ABSTRACT

BEUN. JOSHUA B. Neutrinos, Neutron Capture, and Fission Cycling: Consequences for Supernova Nucleosynthesis. (Under the direction of Professor G. C. McLaughlin).

A long-standing problem in the field of nuclear astrophysics is the question of which astrophysical environment(s) serves as a host to the elemental production process known as the r-process. The r-process is the sequence of nuclear reactions that is responsible for producing the heaviest elements in nature and generates about half of the solar system abundance of nuclei with $A \geq 100$. While the basic recipe for generating r-process elements is understood, the production of heavy nuclei through repetitions of neutron capture and β-decay, determining the astrophysical production site of the r-process has remained elusive. We examine how the r-process environment would be affected by the presence of a sterile neutrino, and we find that the resulting conditions yield an r-process that can reproduce the observed r-process abundance pattern more closely than other models of the r-process. We explore the r-process under conditions where both fission cycling and steady-β flow obtain and find that these mechanisms can jointly operate in the r-process to yield an abundance pattern that reproduces the features of the halo star data. We have examined the role that individual neutron capture cross sections play in the r-process and, contrary to conventional wisdom, find that the evolution of the r-process is sensitive to the neutron capture cross sections of certain, critical nuclei.

Neutrinos, Neutron Capture, and Fission Cycling: Consequences for Supernova Nucleosynthesis

by
Joshua Beun

A dissertation submitted to the Graduate Faculty of
North Carolina State University
in partial fullfillment of the
requirements for the Degree of
Doctor of Philosophy

Physics

Raleigh, North Carolina

2008

APPROVED BY:

Dr. J. Engel	Dr. M. Bourham
Dr. G. C. McLaughlin Chair of Advisory Committee	Dr. J. Blondin

BIOGRAPHY

The author was born in Sherrodsville, OH and moved to Marshall, WI in 1992. Joshua completed his Bachelor's of Science in Engineering-Physics at the University of Wisconsin-Platteville in May 2002, and married Stacy Leigh in June 2002. Joshua has two daughters, Emily Elizabeth who was born on April 15, 2003, and April Alyssa who was born June 30th, 2006.

ACKNOWLEDGMENTS

I would like to thank my adivsor who has been gracious with her time and overflowing with guidance and support. I would like to thank my collaborators Rebecca and Raph, whose expert knowledge has greatly aided my studies. I want to thank my parents, who have always been a source of unwavering support throughout the seas of uncertainty. I would like to extend extreme gratitude to my wife, Stacy, for without her none of this would have been possible. Finally, I would like to thank my daughters, April and Emily, who give me a new reason to smile every day.

TABLE OF CONTENTS

LIST OF FIGURES . . . . . **v**

1 Introduction **1**
1.1 Formation of the Heavy Elements 2
1.2 The Classical r-process 4
1.3 The Neutrino-Driven Wind Environment 8
1.4 Model of r-process Nucleosynthesis 11
1.5 Recent Developments in the r-process 17

2 Active-Sterile Neutrino Oscillations and the r-process **20**
2.1 Background 20
2.2 Nucleosynthesis in the Neutrino Driven Wind 23
2.3 Matter-Enhanced Active-Sterile Neutrino Oscillations 26
2.4 Network Calculations 30
2.5 Fission in r-process Nucleosynthesis 31
2.6 Results and Discussion 32
2.7 Conclusions 41

3 Fission Cycling in a Supernova r-process **43**
3.1 Background 43
3.2 Description of Nucleosynthesis Modeling 47
3.3 Fission Cycling 48
3.4 Steady Beta Flow 55
3.5 Influence of Neutrinos on the Electron Fraction 57
3.6 Conclusions 64

4 The Role of the ^{130}Sn (n,γ) Rate in the r-process **66**
4.1 Background 66
4.2 Model of r-process Nucleosynthesis 69
4.3 ^{130}Sn as a Secondary Waiting Point 69
4.4 Impact of ^{130}Sn (n,γ) on the r-process 72
4.5 Conclusions 77

Bibliography **79**

LIST OF FIGURES

Figure 1.1 Abundance distribution of neutron-capture elements from the s-process and the r-process. The signature of a neutron-capture processes is the accumulation of material at the closed neutron shells of $N = 50$, 82, and 126. At a closed shell, the faster neutron-capture in the r-process results in abundance peaks that are lower in A than the peaks of the s-process. Figure from Sneden and Cowan 2003 [1]. 4

Figure 1.2 Wind Density (g cm^{-3}) as a function of time (s) for the two primary neutrino-driven wind models employed in this work. The faster timescale model, $\tau = 0.1$ s, occurs a steeper density drop in time than the slower timescale model, $\tau = 0.3$ s. 13

Figure 1.3 The abundance pattern of the r-process elements is consistent among the available halo star data between the second and third r-process peak regions and is in good agreement with the solar system r-process abundance pattern. The r-process abundance patterns of the most strongly-enhanced r-process metal-poor stars are shown as the various symbols. The solid line is the scaled solar r-process pattern. All patterns are arbitrarily offset vertically. Figure from Cowan 2007 [2]. 18

Figure 2.1 In the top panel we show the contours of electron fraction, Y_e, at the onset of rapid neutron capture, $T_{keV} \approx 200$. For the astrophysical conditions below, one expects an r-process for $Y_e \lesssim 0.35$ and an r-process which matches the observed ratio of peaks heights for $Y_e \lesssim 0.3$. For comparison with previous work, in the bottom right panel, we show the Y_e, earlier, at the onset of heavy element formation, $T_{keV} \approx 600$. Neutrino captures on free nucleons increase the electron fraction slightly, between $T_{keV} \approx 600$ and $T_{keV} \approx 200$. The neutrino-driven wind parameters are entropy per baryon of $S/k = 100$, expansion time scale of $\tau = 0.3\,s$, neutrino luminosities of $L_\nu = 10^{51}$ ergs s^{-1} and $L_{\bar{\nu}} = 1.3 \times 10^{51}$ ergs s^{-1}, and neutrino temperatures $T_\nu = 3.5$ MeV and $T_{\bar{\nu}} = 4.5$ MeV. 24

Figure 2.2 Electron neutrinos undergoing transformation to sterile neutrinos above the surface of the neutron star by active-sterile MSW neutrino transformation. The active-sterile neutrino mixing parameters are $\delta m^2 = 2\,\mathrm{eV}^2$ and $\sin^2 2\theta_v =$

7×10^{-2}, with the wind parameters of Fig. 2.1. The neutrinos shown have energy $E_\nu \approx 11$ MeV. 29

Figure 2.3 Electron fraction, Y_e is plotted vs. T_{keV} for the wind parameters in Fig. 2.1, with active-sterile neutrino mixing parameters of $\delta m^2 = 10\,\mathrm{eV}^2$ and $\sin^2 2\theta_v = 0.001$. The appropriate neutrino interactions are turned off at $T_{keV} = 850$ for the neutrino-nucleon interactions only and no neutrino interactions cases. The Y_e continues to increase even after heavy element formation, due primarily to neutrino-nucleon interactions. 33

Figure 2.4 An r-process pattern (dark line) producing only the second and third of the three r-process peaks occurs in the neutrino-driven wind when there is active-sterile neutrino mixing. The dramatic impact of active-sterile neutrino oscillations on the r-process is seen immediately when contrasted against the abundances produced without neutrino mixing (light gray line). For the dark line neutrino mixing parameters of $\delta m^2 = 2\,\mathrm{eV}^2$ and $\sin^2 2\theta_v = 7 \times 10^{-2}$ are used together with same astrophysical conditions as in Fig. 2.1. The general features of the r-process pattern above $A \gtrsim 130$ found in solar system data [3] (medium gray line) are reproduced when $Y_e \lesssim 0.3$ at the onset of neutron capture element formation. The solar data is scaled to the simulation such that the sum of the $A = 195$ nuclides is 2.3×10^{-3}. 34

Figure 2.5 The general features of the r-process pattern found in halo stars are reproduced in the neutrino-driven wind when active-sterile neutrino oscillations occur. Only the second, $A \approx 130$ ($Z \approx 55$), third peaks, $A \approx 195$ ($Z \approx 80$), as well as the rare earth bump inbetween, are reproduced. The halo star CS 22892-052 [4] abundances are plotted for comparative purposes (dots) along with the solar system r-process abundances from [3] (dark line). Neutrino mixing parameters of $\delta m^2 = 2\,\mathrm{eV}^2$ and $\sin^2 2\theta_v = 7 \times 10^{-2}$ were used for the neutrino driven wind abundances (light line), although the pattern shown is fairly insensitive to the exact choice of mixing parameter (see Fig. 2.6). The astrophysical conditions are the same as in Fig 2.1. The measured abundances are scaled to the simulation such that the sum of the $Z = 70$ isotopes in each abundance curve have an abundance of 10^{-3}. 35

Figure 2.6 Fission cycling produces a consistent overall r-process pattern in the neutrino-driven wind, as long as $Y_e \lesssim 0.3$ at the onset of neutron capture element formation (bottom panel). In the top panel we show neutron abundance vs. T_{keV} for three sets of neutrino mixing parameters, $\delta m^2 = 10\,\mathrm{eV}^2$ and $\sin^2 2\theta_v = 10^{-2}$, $\delta m^2 = 5\,\mathrm{eV}^2$ and $\sin^2 2\theta_v = 10^{-2}$, and $\delta m^2 = 2\,\mathrm{eV}^2$ and $\sin^2 2\theta_v = 7 \times 10^{-2}$ corresponding to electron fractions of $Y_e = 0.1174$, $Y_e = 0.1752$, and $Y_e = 0.2498$ respectively. The Y_e in the legend occurs at

the start of heavy element formation, $T_{keV} \approx 200$. Lower Y_e's lead to more neutrons but a similar abundance pattern. In the bottom panel we show the abundance patterns from the same mixing parameters as used in the top panel. The abundances curves and astrophysical conditions are the same as figure 2.5. 36

Figure 2.7 Contours indicating the parameter space for which we find an r-process (defined as $Y_e \lesssim 0.35$) in the prospective neutrino mixing parameter range of Mini-BooNE. The light gray region signifies an r-process for an outflow timescale of $\tau = 0.1\,s$, and similarly the dark gray region for $\tau = 0.3\,s$, with a reminder of the astrophysical conditions listed in Fig. 2.1. The black region is the combined NSBL and LSND 90% CL allowed region [5]. The parameter space which produces a successful r-process is much larger than the space probed by experiment. 37

Figure 3.1 The final $R_{\rm peak}$ (Eqn. 3.6) resulting from a symmetric fission distribution for two different outflow timescales, $\tau = 0.1$ s (circles) and $\tau = 0.3$ s (squares), is shown for a variety of electron fractions, Y_e. For very neutron-rich conditions, $Y_e \lesssim 0.1$, a consistent r-process pattern forms between the second, $A \approx 130$, and third, $A \approx 195$, peak region. Fission cycling during the r-process links the second and third peaks, as material that captures out of the third peak reaches the fission regime. The resulting fission daughter products then rejoin the r-process at the second peak. 50

Figure 3.2 The correspondence between Y_e and both the number of fission cycles, Eqn. 3.7, and the neutron-to-seed ratio are shown for the conditions of Fig. 3.1 for our $\tau \approx 0.3$ s standard calculation. Each data point represents the outcome of an individual r-process calculation with different initial neutrino and antineutrino luminosities. The overlap in the number of fission cycles results from the influence of neutrinos on the abundance pattern as different sets of unique neutrino spectrum can result in similar electron fractions. Material begins to fission when $\gtrsim 200$ free neutrons are present for each seed nuclei. . 51

Figure 3.3 Same as Fig. 3.1, but compares the effects of different fission daughter product distributions. The distribution of daughter products determines if material is deposited above or below the closed-shell nuclei in the $A \approx 130$ peak. Fission distributions depositing material above the closed-shell nuclides, asymmetric fission (diamonds), leads to a higher equilibrium $R_{\rm peak}$, as more material is cycled through the $A \approx 130$ peak. Distributions depositing material below the peak, symmetric fission (circles), have a lower equilibrium $R_{\rm peak}$ and cycle less material through the peak region. Fission-induced neutron emission deposits additional material below the closed-shell nuclides, lowering $R_{\rm peak}$, and is shown above for asymmetric fission (squares). 53

Figure 3.4 Under very neutron-rich conditions the effective decay rate of the peaks oscillate until equilibrating at the steady β-flow rate. The abundance weighted atomic number, $Z = \sum_{Z=45}^{60} Z\ Y(Z) / \sum_{Z=45}^{60} Y(Z)$, (dashes) is plotted with the abundance weighted β-decay rate, $\Gamma = \sum_{Z=45}^{60} \Gamma_\beta(Z)\ Y(Z) / \sum_{Z=45}^{60} Y(Z)$, of an isotopic chain (solid) for the second, $A \approx 130$, peak region, versus time, t. The oscillation of the decay rates in the peak regions are due to the changing population of different nuclides during the course of fission cycling. To elucidate abundance changes between isotopic chains, the data above results from our phenomenological model, Eqn. 3.8, under conditions with an $Y_e = 0.05$ at the start of the r-process epoch ($T_9 \approx 2.5$). 55

Figure 3.5 We plot the steady β-flow condition, $\sum_A Y(Z,A)\lambda_\beta(Z,A)$, versus atomic number, Z, for two different Y_e's in the neutrino-driven wind. For the case with an $Y_e = 0.1$ at the start of the r-process epoch, conditions are sufficiently neutron-rich for steady β-flow, marked by a straight line. The case with $Y_e = 0.3$ is not neutron-rich enough for steady β-flow to obtain. 56

Figure 3.6 When conditions neutron-rich enough for steady β-flow occur, a consistent r-process pattern emerges regardless of the initial Y_e. The details of the abundance pattern are dependent on the nuclear physics employed in the mass model, as discussed in the text. The abundance, Y, is plotted versus the atomic number, Z, for these very neutron-rich conditions. The dashed line is generated in the neutrino-driven wind for $L_{\nu_e} = 0.02$ and $L_{\overline{\nu}_e} = 3.0$, the dashed-dotted line for $L_{\nu_e} = 0.01$ and $L_{\overline{\nu}_e} = 4.0$, and the solid line for $L_{\nu_e} = 0.006$ and $L_{\overline{\nu}_e} = 6.0$. The electron neutrino and anti-neutrino luminosities, L_{ν_e} and $L_{\overline{\nu}_e}$, are in units of $\times 10^{51}$ ergs s^{-1}. The effective temperature of the electron neutrinos is $T_{\nu_e} = 3.5$ MeV and for the electron anti-neutrinos is $T_{\overline{\nu}_e} = 4.5$ MeV. Labeled is Y_e at the start of the r-process epoch. The black line represents the solar system abundances from [6], and the gray diamonds are the r-process abundances from the halo star HD 221170 [7]. All abundances are scaled to 10^{-4} at $Z = 52$. 58

Figure 3.7 The electron fraction, Y_e, is shown over a range of electron neutrino and anti-neutrino temperatures, T_ν and $T_{\overline{\nu}}$. The "alpha" effect equally binds protons and neutrons into α-particles which drives the electron fraction to $Y_e \approx 1/2$ and prevents an r-process. Regions of Y_e before α-particle formation ($T_9 \approx 9.4$), top panel, initially appear favorable to the r-process; however, the "alpha" effect has pushed Y_e near 1/2 by the start of the r-process epoch

($T_9 \approx 2.5$), bottom panel. The effective electron neutrino and anti-neutrino temperatures, T_ν and $T_{\overline{\nu}}$, are in units of MeV. The electron neutrino luminosity is $L_\nu = 1 \times 10^{51}$ ergs s^{-1} and the electron anti-neutrino luminosity is $L_{\overline{\nu}} = 1.3 \times 10^{51}$ ergs s^{-1}..... 61

Figure 3.8 The electron fraction, Y_e, is shown over a range of electron neutrino and anti-neutrino luminosities, L_ν and $L_{\overline{\nu}}$. A reduction in the electron neutrino luminosity, L_ν, prevents the "alpha" effect and leads to a successful r-process. The "alpha" effect is avoided as reducing the electron neutrino luminosity, L_ν, lowers the rate of neutrino capture on neutrons forming protons, Eqn. 3.1. The electron fraction, Y_e, is favorable for the r-process before α-particle formation ($T_9 \approx 9.4$), top panel, and reductions in L_ν lead to a low Y_e conditions for the r-process, bottom panel. The electron neutrino and anti-neutrino luminosities, L_ν and $L_{\overline{\nu}}$, are in units of $\times 10^{51}$ ergs s^{-1}. The effective temperature of the electron neutrinos is $T_\nu = 3.5$ MeV and for the electron anti-neutrinos is $T_{\overline{\nu}} = 4.5$ MeV. For low values of both L_ν and $L_{\overline{\nu}}$, electron and positron capture set the Y_e..... 62

Figure 3.9 Under the wind conditions of Fig. 3.8, neutrino luminosities, L_ν and $L_{\overline{\nu}}$ in units of $\times 10^{51}$ ergs s^{-1}, necessary for a successful r-process (all shaded regions), the presence of fission cycling (medium gray and black), and for the presence of steady β-flow (black) are shown. 63

Figure 4.1 We show the ratio (logarithmic) of the largest neutron capture cross section with respect to the smallest neutron capture cross section over the chart of the nuclei between the three sets of theoretical neutron capture cross sections listed in the text. The neutron capture cross sections can vary by many orders of magnitude (ratios of over 10^{10} for the darkest squares) between the theoretical models. 68

Figure 4.2 In the right hand frame, we show an example of the most populated nuclei near ^{130}Sn at the time it becomes populated in an r-process in the neutrino-driven wind, $t \approx 3.5$ s. These r-process nuclei include ^{130}Cd, ^{130}In, and ^{132}Sn. In the left hand frame, the classical waiting point nuclei along $N = 82$ are shown. We employ the following wind parameters for the neutrino-driven wind: an expansion timescale of $\tau = 0.3$ s and an entropy per baryon of $S/k = 100$. 70

Figure 4.3 The flow of material along the β-decay reaction channel of the $A = 130$ path nuclei is shown above. The arrows indicate the direction of β-decay. ^{130}Sn is heavily populated by material that arrives from the β-decay pathway of ^{130}Cd and ^{130}In. The figure is shown for the same conditions as Fig. 4.2. . 71

Figure 4.4 The flow of material near ^{130}Sn is shown above. The arrows that point towards the right indicate the direction of the neutron capture reaction channel, and the arrows that point along the diagonal indicate the direction of β-decay. A large amount of material arrives at ^{130}Sn from the β-decay of the $A = 130$ nuclei. Depending on the neutron capture cross section of ^{130}Sn, some fraction of this material is re-directed along the $Z = 50$ neutron capture reaction channel. The conditions here are the same as Fig. 4.2. 72

Figure 4.5 The percent change in abundance across the r-process is shown for an r-process calculation under an increase in the neutron capture cross section of ^{130}Sn by a factor of 100 with respect to the baseline calculation. For an r-process with the increased neutron capture cross section, the abundance of the $A = 130$ nuclei decreases by $\sim 90\%$ while the abundance of the $A = 131$ nuclei increases by $\sim 190\%$ with respect to the baseline calculation. The size of the effects on the abundance pattern above the $A = 130$ region range from 0 to $\sim 35\%$. 74

Figure 4.6 The absolute difference in the abundance of ^{130}Sn (solid line) is shown above for an r-process simulation with the neutron capture cross section of ^{130}Sn increased by a factor of 100, $Y_{\rm Rate}$, and the baseline r-process calculation with the unaltered set of neutron capture rates, $Y_{\rm Baseline}$. An increase in the neutron capture cross section of ^{130}Sn leads to the capture of additional neutrons by ^{130}Sn, depleting the abundance of ^{130}Sn and enhancing the abundance of ^{131}Sn. The absolute difference in the abundance of ^{131}Sn (dashed line) is also shown. 75

Figure 4.7 We show the relative rate of net neutron capture, $\dot{\eta}$, summed over each of the three peak regions of the r-process (Eq. 4.6). Above, the relative difference in $\sum \dot{\eta}$ is shown between an r-process with the neutron capture cross section of ^{130}Sn increased by a factor of 100, $\sum \dot{\eta}_{\rm Rate}$, and the baseline calculation, $\sum \dot{\eta}_{\rm Original}$. The cross section increase yields an increase in the amount of neutron capture that occurs in the $A \sim 130$ peak and reduces the amount of neutron capture for nuclei in the rare earth and $A \sim 195$ peak regions. 76

Figure 4.8 The abundance pattern of the third r-process peak is shown above for two r-process calculations, an r-process simulation with the neutron capture cross section of ^{130}Sn increased by a factor of 100 (dashed line), and the baseline r-process calculation with the unaltered set of neutron capture cross sections (solid line). Increasing the neutron capture cross section of ^{130}Sn alters the distribution of material in the rare earth and third peak regions by shifting the abundance towards lighter nuclei in A. 77

Chapter 1

Introduction

The foundations of the current understanding of the formation of the elements rest largely on the seminal work by Burbidge, Burbidge, Fowler, and Hoyle (B^2FH) [8]. In their work, B^2FH outlined the astrophysical production sites and nuclear reaction mechanisms responsible for producing the quantities of the elements found in nature. The process thought to produce the heaviest elements in nature, known as the r-process, is responsible for the formation of about half of the solar abundance of elements with mass number $A > 100$ [9]. B^2FH postulated that an explosive, neutron-rich environment would be necessary for the production of these elements. Although there are many astrophysical candidates that could act as a potential host(s) for the r-process, none possess all of the essential ingredients necessary for r-process element production.

In this chapter, a summary of the principles of the r-process is presented, followed by an overview of the neutrino-driven wind environment of the core-collapse supernova, a promising r-process candidate site. Next, the details of our calculation of r-process element abundances in the neutrino-driven wind environment are provided. Lastly, some recent developments in the r-process are discussed along with an overview of the methods employed in this work to explore these issues. We discuss an impediment to the r-process in the neutrino-driven wind that results from the reduction of the free neutron abundance by the α effect. Then, we describe how the consistent pattern of r-process element abundances found throughout the halo

star data may point to the presence of the operation of fission cycling during the r-process. Finally, we discuss how the neutron-capture cross sections of critical nuclei may influence the r-process and present the implications this has on the nuclear data needs of the r-process. Additional details of the r-process may be found in the recent r-process review articles [10, 11, 12].

1.1 Formation of the Heavy Elements

Following the Big Bang, the primordial composition of the elements consisted of mainly Hydrogen, Helium, and Lithium. The production of the elements lighter than Iron ($Z < 26$) were constructed from these original building blocks and proceeded mostly through nuclear reactions involving charged particles, the fusion of α particles for example. These reactions took place in the hot, dense environments of stars. As the stars progressed along their evolutionary path, heavier and heavier elements were formed, a consequence of the higher temperatures and densities found in the subsequent stages of stellar evolution. Once the core of a star burns to Iron, stellar nuclear burning no longer generates the energy a star requires to sustain itself against gravity and, in fact, requires energy. This tipping point in the sequence of energy generation of stellar burning, along with the energetics required to overcome the Coulomb barrier of nuclei with increasingly larger proton number, Z, prevent stellar burning from producing the heaviest elements in nature.

Neutron-capture provides a mechanism for accumulating nucleons onto the nucleus and producing the heaviest elements in nature. Additionally, the neutron carries no charge, allowing it to capture onto nuclei that contain large numbers of protons without experiencing the repulsive force of the Coulomb barrier. Nucleosynthesis cannot proceed through neutron-capture alone as this mechanism does not increase the total proton number inside the nucleus, however. In order to increase both the atomic weight, A, and atomic number, Z, through a neutron-capture process, neutron-capture must be paired with a second reaction, β-decay. A proton is produced by β-decay from the decay of a neutron. This combination of neutron-capture and β-decay allows the nucleus to effectively capture a proton as a result of neutron-

capture, and provides a neutron-capture mechanism for the production of the heavy elements.

B^2FH found evidence for the operation of a neutron-capture process from abundance distributions of the elements that featured material accumulating near the closed neutron shells of $N = 50$, 82, and 126. Nuclei at the closed neutron shells are relativity stable, and the net capture of neutrons here is low. As a result, r-process nuclei will accumulate here. The observation of two sets of nuclei strongly peaked at each of the three closed neutron shells pointed to the presence of elements formed from two distinct neutron-capture processes, see Fig. 1.1. The location of the peaks near the closed neutron shells depends on the relative speed of neutron-capture with respect to β-decay of the production process. For a process where neutron-capture is slow compared to β-decay, these peaks form at a larger A, and this process is known as the s-process. Conversely, the peaks at lower A result from a process where neutron capture is rapid compared to β-decay. This is known as the r-process. Details on both the observations of neutron-capture elements and the separation of individual s-process and r-process patterns are found in [11, 12].

The slow rate of neutron-capture during the s-process, approximately one capture per 100,000 years [8], results in the s-process primarily forming the heavy neutron-capture elements near the path of β stability. The location of the s-process remains near β stability as an s-process nucleus will β-decay before a second neutron can be captured. The structure of the s-process abundance pattern is shown in Fig. 1.1. The s-process cannot produce any nuclei past Lead-208 as the next reaction sequence of a neutron-capture followed by a β-decay leads to the production a nucleus that is α unstable. This α emitter terminates the s-process.

Unlike the s-process, the location of the elements formed by the r-process can extend away from the valley of β stability and can reach near the neutron drip line as a consequence of the rapid accumulation of neutrons that occurs during the r-process. This flight from stability can only be sustained by the presence of a large abundance of free neutrons. Once this supply of neutrons is depleted, the r-process elements return to stability through β-decay. In the r-process, the return to stability from very neutron-rich elements results in the production of the most neutron-rich

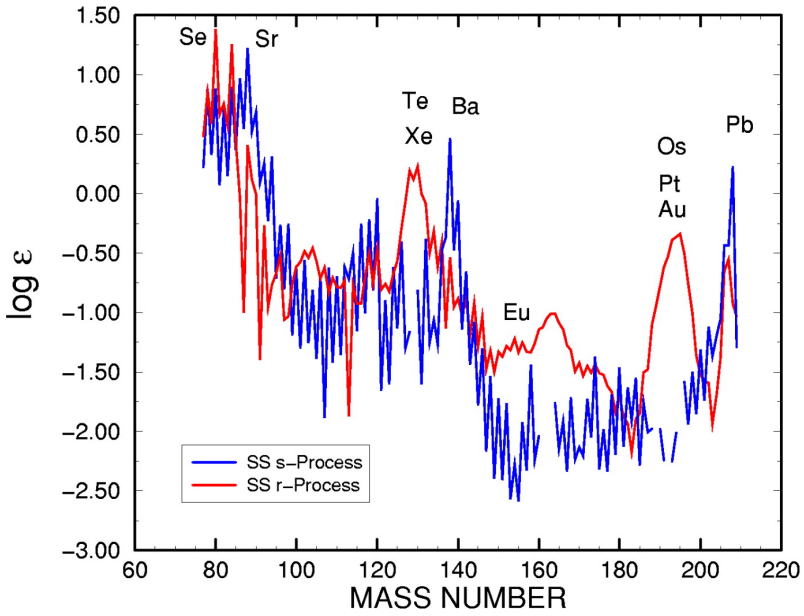


Figure 1.1: Abundance distribution of neutron-capture elements from the s-process and the r-process. The signature of a neutron-capture processes is the accumulation of material at the closed neutron shells of $N = 50$, 82, and 126. At a closed shell, the faster neutron-capture in the r-process results in abundance peaks that are lower in A than the peaks of the s-process. Figure from Sneden and Cowan 2003 [1].

isobar for each stable element in A. Similar to the s-process, large peak features are found in the abundances of r-process elements. The three main r-process peaks occur at $A \sim 80$, 130, and 195 which correspond to the first, second, and third peaks of the r-process respectively. The three r-process peaks are coincident with the closed neutron shells at $N = 50$, 82, and 126. The peak structure of the elements produced by the r-process is shown in Fig. 1.1.

1.2 The Classical r-process

The classical r-process is a model of the r-process under conditions where analytical expressions can adequately describe the evolution of the nuclear abundance. The principle nuclear reactions that participate in the classical r-process are neutron-capture, photo-dissociation, and β-decay. When the r-process occurs in environments with temperatures of $T_9 \gtrsim 1$, where T_9 is in units of 10^9 K, and neutron number den-

sities of $n_n \gtrsim 10^{22}$ cm^{-3}, where n_n is defined as the neutron number density, neutron-capture occurs on a timescale much faster than β-decay, even as the location of the r-process path moves away from the valley of β stability [13]. The r-process path consists of the most abundant isotope in each isotopic chain along Z. The timescale of the r-process can be estimated from the summation of the β-decay lifetimes along the r-process path and is on the order of seconds [14].

A nucleus in the r-process will typically capture multiple neutrons before it undergoes β-decay. The total number of neutrons that a nucleus can capture is limited by the binding energy of the particular nucleus. The binding energy reaches zero at the neutron-drip line, whereupon no additional neutrons can be added. Additionally, photo-dissociation, the reverse process of neutron-capture, works to prevent the capture of neutrons. Under neutron rich conditions in the r-process, the rate of neutron-capture and the rate of photo-dissociation along an isotopic chain can become approximately equal, leading to the condition known as $(n, \gamma) \leftrightarrows (\gamma, n)$ equilibrium. For an r-process under $(n, \gamma) \leftrightarrows (\gamma, n)$ equilibrium, the abundance of nuclei along an isotopic chain is set by $(n, \gamma) \leftrightarrows (\gamma, n)$ equilibrium and the net amount of β-decay between isotopic chains determines the flow of material along the r-process. As the supply of free neutrons is diminished, $(n, \gamma) \leftrightarrows (\gamma, n)$ equilibrium can no longer be maintained. The rate of neutron-capture and photo-dissociation becomes negligible and the r-process nuclei back to stability through β-decay.

The r-process path is useful in describing the location of the r-process nuclei during their travel towards the neutron-drip line and in their return to the valley of β stability. The r-process path consists of the most heavily populated nucleus for each isotopic chain in Z. When the r-process is in $(n, \gamma) \leftrightarrows (\gamma, n)$ equilibrium, the path, known as the equilibrium path, contains the set of waiting point nuclei. The equilibrium path of the r-process is useful as its location can be predicted from the results of detailed balance.

Starting from detailed balance, the relationship between the abundances of adja-

cent nuclei in an isotopic chain can be determined

$$\begin{aligned}\frac{Y(Z,A+1)}{Y(Z,A)} &= \frac{n_n\langle v\sigma_{n,\gamma}(Z,A)\rangle}{\lambda_{\gamma,n}(Z,A+1)} \\ &= n_n\left(\frac{2\pi\hbar^2}{m_u kT}\right)^{3/2}\left(\frac{A+1}{A}\right)^{3/2}\times \\ &\quad \frac{G(Z,A+1)}{2G(Z,A)}\exp\left[\frac{S_n(Z,A+1)}{kT}\right] \end{aligned} \tag{1.1}$$

where $Y(Z,A)$ is the abundance, $n_n\langle v\sigma_{n,\gamma}(Z,A)\rangle$ is the thermally averaged neutron-capture rate, $\lambda_{\gamma,n}(Z,A)$ is the photo-disintegration rate, k is the Boltzmann constant, T is the temperature, $\hbar$ is the Planck constant, $G(Z,A)$ is the nuclear partition function, m_u is the atomic mass unit, and $S_n(Z,A+1)$ is the neutron separation energy. The most abundant isotope in each isotopic chain of Z has a neutron separation energy of

$$\begin{aligned} S_n^0 &\approx kT\ln\left[\frac{2}{n_n}\left(\frac{m_u kT}{2\pi\hbar^2}\right)^{3/2}\right] \\ &= \left(\frac{T}{10^9\text{ K}}\right)\left\{2.79+0.198\left[\log\left(\frac{10^{20}\text{ cm}^{-3}}{n_n}\right)+\frac{3}{2}\log\left(\frac{T}{10^9\text{ K}}\right)\right]\right\} \end{aligned} \tag{1.2}$$

where the second line is in units of MeV. S_n^0 results from Eq. (1.1) by approximating the adjacent abundances as equal as well as approximating the mass number and nuclear partition function as equal. The most abundant isotopes will all have the same neutron separation energy, and this value lies between $2-3$ MeV during the r-process [15].

When the r-process has a sufficient pool of seed nuclei to draw from, an additional equilibrium condition forms known as steady-β flow. When the r-process is under steady-β flow, a consistent r-process abundance pattern emerges between pairs of closed neutron shells, and the abundances between individual isotopic chains correspond to their β-decay rates,

$$\lambda_\beta(Z-1)Y(Z-1) = \lambda_\beta(Z)Y(Z), \tag{1.3}$$

where $Y(Z)=\sum_A Y(Z,A)$ and $\lambda_\beta(Z)=\sum_A \lambda_\beta(Z,A)Y(Z,A)/Y(Z)$ where $\lambda_\beta(Z,A)$ is the β-decay rate of the nucleus (Z,A). Under conditions where a steady supply

of seed nuclei were available for the r-process, Kratz et. al 1993 found that steady flow formed between the closed neutron shells, $50 < N \leq 82$ [16]. Similarly, steady-β flow abundance patterns that form between the second and third r-process peaks are a consequence of the slower β-decay rates of the "waiting point" nuclei at $N = 82$ and 126. Under steady-β flow, the r-process abundance pattern is set by the relevant nuclear properties rather than by the astrophysical conditions.

Under very neutron-rich conditions, the r-process can reach nuclei with $Z \geq 80$ that are subject to fission [11]. Once these nuclei fission, their fission products become the seeds of the r-process itself, producing a cyclic flow of material between the nuclei that are undergoing fission and their fission fragments. We introduce the idea of fission cycling in the r-process with a simple model of the r-process under $(n, \gamma) \rightleftharpoons (\gamma, n)$ equilibrium, and with the fission event occurring in coincidence with the β-decay of the heaviest waiting-point nucleus with proton number, Z_f. The heaviest waiting-point nucleus is taken to fission into two distinct fragments with proton numbers, Z_1 and Z_2 ($Z_2 > Z_1$), respectively. Once a sufficient amount of time has passed, and after nuclei below $Z < Z_1$ have been depleted by neutron-capture and β-decay, the abundances along the r-process may be analytically determined. In between the isotopic chains of the fission fragments, $Z_1 < Z < Z_2$, and for all of the isotopic chains above the heavier fragment, $Z_2 < Z \leq Z_f$, the rate of change in the abundance of an isotopic chain is

$$\dot{Y}(Z) = \lambda_\beta(Z-1)Y(Z-1) - \lambda_\beta(Z)Y(Z) \tag{1.4}$$

In addition, the rate of change for the isotopic chains that contain the fission fragments, Z_1 and Z_2, are

$$\dot{Y}(Z_1) = \lambda_\beta(Z_f)Y(Z_f) - \lambda_\beta(Z_1)Y(Z_1), \tag{1.5}$$

$$\dot{Y}(Z_2) = \lambda_\beta(Z_f)Y(Z_f) + \lambda_\beta(Z_2-1)Y(Z_2-1) - \lambda_\beta(Z_2)Y(Z_2). \tag{1.6}$$

The formation of a steady state set of abundances can be achieved after a few fission cycles as the flow at the bottom of the r-process, at the lower proton numbers, Z_1 and Z_2, by fission, is fed by the fission products of Z_f. The fission cycling process can result in a robust r-process pattern between the second and third r-process peaks at $A \sim 130$ and 195 [17].

Late in the r-process, the number of available free neutrons wanes and the temperature falls as a function of time. The r-process enters the freeze-out phase, and neutron-capture occurs at slower and slower timescales. The start of freeze-out is typically marked by

$$R = \frac{Y_n}{\Sigma_i Y_i} \sim 1, \tag{1.7}$$

where Y_n is the free neutron abundance and $\Sigma_i Y_i$ is the sum of the abundances of the rest of the nuclear species that are participating in the r-process. The ratio of the free neutron abundance and the sum over the remainder of the nuclear species is known as the neutron to seed ratio, R. Over the course of freeze-out, the analytical expressions employed above to describe the r-process become less effective and break down, particularly the above assumptions involving $(n, \gamma) \leftrightarrows (\gamma, n)$ equilibrium due to the lack of sufficiently neutron rich conditions. To accurately track the evolution of the r-process abundances during the freeze-out epoch, it is necessary to perform full network calculations that can account for the individual r-process reactions without assumptions of reactions in equilibrium.

1.3 The Neutrino-Driven Wind Environment

Proposed sites for the r-process include the neutrino-driven wind of a core-collapse supernova [18, 19, 20, 21, 22, 23, 24, 25, 26, 27], a prompt explosion from a low mass supernova [28, 29], neutron star mergers [30, 31, 32, 33, 34, **?**], a collapsar from a massive stellar progenitor [35, 36], and the shocked surface layers of the post-collapse O-Ne-Mg Cores [37, 38]. No single site is currently thought to contain all of the essential ingredients for the r-process, however. A promising candidate for the r-process, neutrino-driven wind environment, is explored throughout this work, and an outline of the neutrino-driven wind environment is presented here to highlight the critical features most important to the production of r-process elements. For a complete review of both the neutrino-driven wind and the core-collapse supernova environment, see [11, 39].

The core-collapse supernova is a candidate host site of the r-process that is fa-

vored as its expected production of r-process elements is consistent with the r-process material production found in the second and third peaks of the solar system r-process abundances. To meet this requirement, a supernova must eject $\sim 10^{-6}$–$10^{-5}\,M_{\odot}$ of r-process material, where $M_{\odot}$ is the mass of the sun [22, 27]. This is consistent with the amount of material expected to be ejected post-core bounce from the gravitational well of the protoneutron star. This material is ejected as a consequence of neutrino interactions participating in what is known as the neutrino-driven wind. In order for a nucleon to be ejected from the protoneutron star, it must gain about ~ 200 MeV of energy. As each nucleon gains on the order of ~ 20 MeV with each successive interaction with a neutrino, about ten neutrino-nucleon reactions are required to lift nucleons out of the gravitational well of the protoneutron star.

The neutrino-driven wind environment forms out of the final stellar evolutionary stages of a massive star. Stars with over ten times the mass of our own sun, $M \gtrsim 10\,M_{\odot}$, progress through the stages of stellar burning and develop an onion-like structure, with each layer containing the ashes of the elements produced from its previous stellar nucleosynthesis epochs. In the massive star's final stellar burning stage, the core has a nuclear composition of Iron and is enclosed by layers of lighter elements that range from Silicon near the core to Hydrogen near the outer layers. As the nuclear burning of Iron does not generate energy, and the Iron core soon compresses under the force of gravity. The Iron core compresses until it reaches densities on the level of the nucleus, upon which a protoneutron star is formed [40].

The gravitational binding energy of the protoneutron star is released into the emission of neutrinos and anti-neutrinos of the various family flavors [41]. A protoneutron star with a radius of $R_{\rm NS} \sim 10$ km and a mass of $M_{\rm NS} \sim 1.4\,M_{\odot}$ has a gravitational binding energy of $\sim (3/5)GM_{\rm NS}^2/R_{\rm NS} \sim 3 \times 10^{53}$ erg. Here G is the gravitational constant. The gravitational binding energy is often approximated as being distributed equally among the various flavors of neutrinos, on the order of $\sim 10^{51}$ erg s^{-1} for each species of neutrino, during the course of diffusion through the protoneutron star. This diffusion occurs on the order of ~ 10 s and is a consequence of a number of reactions involving the various neutrino family members, *e.g.* all species of neutrinos and anti-neutrinos, e, μ, and τ, can neutral-current scatter of off elec-

trons. The effective temperature of the neutrinos results from the depth from within the protoneutron star that the neutrinos and anti-neutrinos decouple from thermal equilibrium. In addition to neutral-current neutrino-electron scattering, the electron neutrinos and anti-neutrinos, ν_e and $\bar{\nu}_e$, also participate in charged-current reactions here. Since neutrons outnumber protons inside the protoneutron star, the reaction $\nu_e + n \rightarrow p + e^-$ occurs more frequently than the reaction $\bar{\nu}_e + p \rightarrow n + e^+$. As a result, the neutrinos leave local thermodynamic equilibrium in the following order: ν_μ, $\bar{\nu}_\mu$, ν_τ, $\bar{\nu}_\tau$, then $\bar{\nu}_e$, and then ν_e. The relative values of the neutrino energy spectrum for the individual family species are then

$$\langle E_{\nu_\mu} \rangle \approx \langle E_{\bar{\nu}_\mu} \rangle \approx \langle E_{\nu_\tau} \rangle \approx \langle E_{\bar{\nu}_\tau} \rangle > \langle E_{\bar{\nu}_e} \rangle > \langle E_{\nu_e} \rangle \tag{1.8}$$

Of important consequence to heavy element production is that the neutrino energy spectrum is greater for $\bar{\nu}_e$, with $\langle E_{\bar{\nu}_e} \rangle \approx 16$ MeV, than for ν_e, with $\langle E_{\nu_e} \rangle \approx 11$ MeV [41]. This difference in neutrino energy spectrum between ν_e and $\bar{\nu}_e$ will set the stage for the neutron rich environment necessary for the r-process.

The temperature above the protoneutron star is sufficiently large for nuclear statistical equilibrium (NSE) to occur, with the entropy directing the nuclear composition of the material towards nucleons rather than that of the heavier nuclei. The material in NSE is heated and directed away from the protoneutron star by the neutrino-nucleon reactions $\bar{\nu}_e + p \rightarrow n + e^+$ and $\nu_e + n \rightarrow p + e^-$. This expansion of material off of the protoneutron star by neutrinos and anti-neutrinos is known as the neutrino-driven wind. After the point above the protoneutron star where the temperature falls to $T \sim 6 \times 10^9$ K, the neutrino-driven wind is essentially in a state of adiabatic expansion as the decreasing neutrino flux, resulting from the increasing distances away from the protoneutron star, no longer has sufficient strength to play the lead role in setting the wind dynamics.

A quantity used for tracking the neutron richness of the neutrino-driven wind environment is the electron fraction, Y_e. The electron fraction plays a role in determining the abundance outcome of the r-process, and near the protoneutron star, it is influenced by both neutrino-nucleon reactions and electron and positron captures. When both the total proper neutron and proton number densities, N_n and N_p respectively,

are known, it is convenient use the following form of the electron fraction,

$$Y_e = \frac{N_p}{N_p + N_n} \tag{1.9}$$

The neutron-to-proton ratio may be taken as N_n/N_p. Equivalently, the electron fraction can be calculated from the abundance information of all of the participating nuclear species,

$$Y_e = \sum_i Z_i Y_i \tag{1.10}$$

Where i is an index over all nuclear species, Z_i is the proton number of an individual nuclear species, and Y_i is the abundance of the nuclear species. We note that both of these expressions of the electron fraction assume overall charge neutrality.

In the neutrino-driven wind, the conditions are generally such that electron and positron capture on nucleons, $e^- + p \rightarrow n + \nu_e$ and $e^+ + n \rightarrow p + \bar{\nu}_e$ respectively, are less important than the neutrino-nucleon interactions, $\bar{\nu}_e$ capture on protons and ν_e capture on neutrons, $\bar{\nu}_e + p \rightarrow n + e^+$ and $\nu_e + n \rightarrow p + e^-$ respectively [42]. The interplay between these two neutrino-nucleon terms serve to set the electron fraction,

$$Y_e \approx \frac{\lambda_{\nu_e}}{\lambda_{\nu_e} + \lambda_{\bar{\nu}_e}} = \frac{1}{1 + (\lambda_{\bar{\nu}_e}/\lambda_{\nu_e})}. \tag{1.11}$$

Above, $\lambda_{\bar{\nu}_e}$ is the rate of the $\bar{\nu}_e + p \rightarrow n + e^+$ interaction, and λ_{ν_e} is the rate of the $\nu_e + n \rightarrow p + e^-$ interaction.

At this point above the protoneutron star, as the neutrino luminosities of both $\bar{\nu}_e$ and ν_e are approximately equal, $L_{\nu_e} \sim L_{\bar{\nu}_e}$, and since $\bar{\nu}_e$ are emitted with larger mean spectral energies than ν_e, $\langle E_{\bar{\nu}_e} \rangle > \langle E_{\nu_e} \rangle$, the rate of antineutrino capture on protons is faster than the rate of neutrino capture on neutrons, $\lambda_{\bar{\nu}_e} > \lambda_{\nu_e}$. From Eq. 1.11, this leads to neutron rich conditions, $Y_e < 0.5$, while material is propagating in the neutrino-driven wind [22]. The presence of neutron rich conditions are critical to the production of r-process elements in this environment.

1.4 Model of r-process Nucleosynthesis

This section outlines the details of the numerical r-process simulation employed in this work to calculate the abundances of r-process elements that are produced in

the neutrino-driven wind environment of the core collapse supernova.

To describe the trajectory of the mass element as it travels from the surface of the protoneutron star, we employ a one-dimensional model of the neutrino-driven wind. The one-dimensional parameterization of the neutrino-driven wind results from a constant mass outflow rate ($\dot{M} = 4\pi r^2 \rho v$) in the neutrino-driven wind with a homologous outflow with a radial velocity v of

$$v \propto r, \tag{1.12}$$

where r is the radial distance measured from the center of the protoneutron star [20]. The radial distance can be expressed as a function of time,

$$r = r_o \exp(t/\tau), \tag{1.13}$$

where r_o is the initial radius. We define the expansion time scale τ as

$$\tau = r/v. \tag{1.14}$$

The enthalpy per baryon is taken to scale as $\propto 1/r$. This leads to the equation for the density that the mass element encounters in the neutrino-driven wind,

$$\rho \propto \rho_o \exp(-3t/\tau). \tag{1.15}$$

The density profile of the wind model employed in these studies and the impact of the choice of the expansion time scale τ on the density profile are shown in Fig. 1.2,

Our nucleosynthesis simulations track the chemical evolution of a mass element as it encounters and evolves in concert with the various conditions of its astrophysical host. While the mass element is considered to occupy space as a point particle, it is important to note that the mass element does not need to be composed of a single nuclear species, and, in fact, will contain the fractional abundance of all the species that participate in the nucleosynthesis process. The relationship between the abundance of a nuclear species $Y(Z, A)$ and the proper number density of a nuclear species $n_{Z,A}$ is

$$n_{Z,A} = \rho N_A Y(Z, A) \tag{1.16}$$

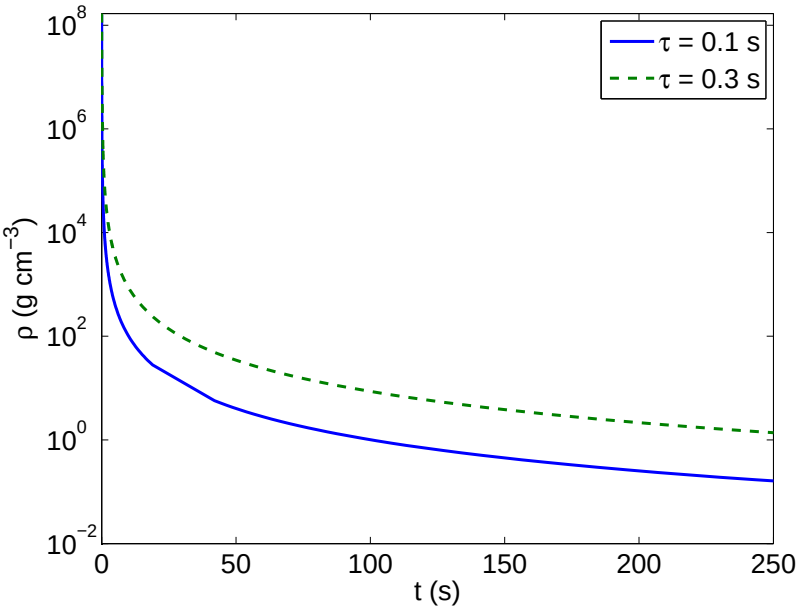


Figure 1.2: Wind Density (g cm^{-3}) as a function of time (s) for the two primary neutrino-driven wind models employed in this work. The faster timescale model, $\tau = 0.1$ s, occurs a steeper density drop in time than the slower timescale model, $\tau = 0.3$ s.

Above, N_A is Avagadro's number and ρ is the density.

In the neutrino-driven wind environment, the mass element encounters three primarily epochs of nucleosynthesis during its flight from the protoneutron star: the nuclear statistical equilibrium (NSE) epoch, the charged particle nucleosynthesis epoch, and the r-process nucleosynthesis epoch. The mass element experiences a different set of astrophysical conditions in each nucleosynthesis epoch as well as evolving towards different chemical compositions. Our simulation handles each epoch separately and evolves the mass element sequentially through three separate FORTRAN codes, each specific to a separate nucleosynthesis epoch. Details of the simulation of the NSE epoch are found in [43], details of the charged particle reaction epoch simulation are found in [44], and details of the simulation of the r-process epoch are found in [45]. The electron fraction is calculated in a self-consistent fashion throughout all of the nucleosynthesis epochs.

Our simulation of NSE employs distance, temperature, and density information

to calculate all relevant thermodynamic quantities including electron and positron number densities. As the mass element is initially ejected from the protoneutron star at temperatures of $T_9 \approx 35$ and entropies of $S/k \sim 100$, the chemical composition of the mass element is well described by NSE [43]. The relevant thermodynamic quantities are placed as inputs in the NSE simulation, and the resulting abundances of neutrons, protons, and light elements with $(A > 40)$ are calculated.

As the mass element leaves the NSE regime, at a temperature of $T_9 \lesssim 10$, we employ a full reaction-rate network to track the nucleosynthetic evolution of the mass element. In this regime, nuclei of intermediate atomic weight, $A \lesssim 120$, are accounted for. The set of reaction rates employed by our simulation for this nucleosynthesis epoch are taken from [46] and include all relevant strong, electromagnetic, and weak interaction rates. The calculation of the evolution of the abundance proceeds as follows. Given a set of nuclear abundances and their individual reaction rates at a time, t, the time derivatives of the abundances, $\dot{\vec{Y}}$, are calculated. The individual nuclear abundances are to be generated using the finite difference prescription over the time step, Δt,

$$\frac{\vec{Y}(t+\Delta t) - \vec{Y}(t)}{\Delta t} = \begin{array}{ll} \dot{\vec{Y}}(t) & (explicit) \\ \dot{\vec{Y}}(t+\Delta t) & (implicit) \end{array} \tag{1.17}$$

As the set of reaction rates that participate in this nucleosynthesis epoch contain reaction rates that are relatively very slow, the rates associated with the weak interaction for example, and those that are relatively very fast, the rates associated with charged particle interactions, a fully implicit technique is employed to evolve the nuclear abundances over the time of the nucleosynthesis epoch. The solution of the implicit form of Eq. 1.17 is accomplished by solving for the zeros of the set of equations

$$\vec{\mathcal{Z}}(t+\Delta t) \equiv \frac{\vec{Y}(t+\Delta t) - \vec{Y}(t)}{\Delta t} - \dot{\vec{Y}}(t+\Delta t) = 0 \tag{1.18}$$

To solve this set of equations, we use the Newton-Raphson method [47], which employs the Taylor series expansion of $\vec{\mathcal{Z}}(t+\Delta t)$, and generates the trial change in the

abundances as

$$\Delta\vec{Y} = \left(\frac{\partial\vec{\mathcal{Z}}(t+\Delta t)}{\partial\vec{Y}(t+\Delta t)}\right)^{-1}\vec{\mathcal{Z}} \tag{1.19}$$

where $\partial\vec{\mathcal{Z}}/\partial\vec{Y}$ is the Jacobian of $\vec{\mathcal{Z}}$. Once the convergence of the abundances $\vec{Y}(t+\Delta t)$ is complete, the simulation proceeds to the next time step. The process repeats until the mass element arrives at the conditions that mark the start of the r-process epoch.

After the mass element leaves the the charged particle reaction epoch, it enters the r-process nucleosynthesis epoch at a temperature of $T_9 \lesssim 2.5$. The relevant nuclear reactions for the r-process are neutron-capture, photo-disintegration, β-decay, charged-current neutrino interactions, β-delayed neutron emission, and for very neutron rich environments, fission processes. We employ the nuclear mass model from [48], β-decay rates from [49], and neutron-capture rates from [46]. Neutrino interactions as well as fission probabilities are discussed in Chapters 2 and 3. Neglecting interactions involving neutrinos and fission processes to highlight the reaction physics, the nuclear reactions involving the change in abundance for a single r-process nucleus can be written as

$$\begin{aligned}
\dot{Y}(Z,A) \;=\;& n_n\langle v\sigma_{n,\gamma}(Z,A-1)\rangle Y(Z,A-1) + \lambda_{\gamma,n}(Z,A+1)Y(Z,A+1) \\
&+\lambda_{\beta 0}(Z-1,A)Y(Z-1,A) \\
&+\lambda_{\beta 1}(Z-1,A+1)Y(Z-1,A+1) \\
&+\lambda_{\beta 2}(Z-1,A+2)Y(Z-1,A+2) \\
&+\lambda_{\beta 3}(Z-1,A+3)Y(Z-1,A+3) \\
&-n_n\langle v\sigma_{n,\gamma}(Z,A)\rangle Y(Z,A) - \lambda_{\gamma,n}(Z,A)Y(Z,A) \\
&-[\lambda_{\beta 0}(Z,A)+\lambda_{\beta 1}(Z,A)+\lambda_{\beta 2}(Z,A)+\lambda_{\beta 3}(Z,A)]Y(Z,A),
\end{aligned} \tag{1.20}$$

where n_n is the neutron number density, $\lambda_{\gamma,n}(Z,A)$ is the photo-disintegration rate, $n_n\langle v\sigma_{n,\gamma}(Z,A)\rangle$ is the thermally averaged neutron-capture rate, and $\lambda_{\beta 0}(Z,A)$, $\lambda_{\beta 1}(Z,A)$, $\lambda_{\beta 2}(Z,A)$, and $\lambda_{\beta 3}(Z,A)$ are the rates for β-decay and the subsequent emission of 0, 1, 2, and 3 neutrons respectively. The set of these equations, with a separate equation for each nuclear species that participates in the r-process, forms the basis of our

r-process network.

As before, the time evolution of these equations lends itself to an implicit differencing solution as interactions that proceed at slower rates, such as β-decay, and those that proceed at faster rates, such as neutron-capture, simultaneously participate in the r-process. For a sufficiently short time step, Δt, the free neutron abundance, temperature, and density can be taken to be constant over the time step. The reactions of the r-process, Eq. 1.20, can then be written in the finite difference form,

$$\begin{aligned}
\Delta Y(Z,A)/\Delta t \;=\; & n_n\langle v\sigma_{n,\gamma}(Z,A-1)\rangle(Y(Z,A-1)+\Delta Y(Z,A-1)) \\
& +\lambda_{\gamma,n}(Z,A+1)(Y(Z,A+1)+\Delta Y(Z,A+1)) \\
& +\lambda_{\beta 0}(Z-1,A)(Y(Z-1,A)+\Delta Y(Z-1,A)) \\
& +\lambda_{\beta 1}(Z-1,A+1)(Y(Z-1,A+1)+\Delta Y(Z-1,A+1)) \\
& +\lambda_{\beta 2}(Z-1,A+2)(Y(Z-1,A+2)+\Delta Y(Z-1,A+2)) \\
& +\lambda_{\beta 3}(Z-1,A+3)(Y(Z-1,A+3)+\Delta Y(Z-1,A+3)) \\
& -n_n\langle v\sigma_{n,\gamma}(Z,A)\rangle(Y(Z,A)+\Delta Y(Z,A)) \\
& -\lambda_{\gamma,n}(Z,A)(Y(Z,A)+\Delta Y(Z,A)) \\
& -[\lambda_{\beta 0}(Z,A)+\lambda_{\beta 1}(Z,A)+\lambda_{\beta 2}(Z,A)+\lambda_{\beta 3}(Z,A)]\times \\
& (Y(Z,A)+\Delta Y(Z,A)) \qquad (1.21)
\end{aligned}$$

The time evolution of the system can now be performed by solving the linear set of equations of the change in abundance for each nuclear species, $\Delta Y(Z,A)$, at each time step. Using a time step, Δt, of appropriate duration, the solution of these equations proceeds by first triangularizing the matrix formed by Eq. 1.21. The individual $\Delta Y(Z,A)$'s are then found by using back substitution [47]. These $\Delta Y(Z,A)$'s are then used to evolve the abundances of the nuclear species $Y(Z,A)$ forward in time. The set of solutions allow the Δt of the next time step to be calculated. This method of evolving the abundances of the nuclear species through finite differencing is repeated until the mass element is evolved to the end of its thermodynamic trajectory. The final abundance composition of the mass element can then be compared to other abundance patterns of the r-process.

1.5 Recent Developments in the r-process

The above sections have outlined the features of the neutrino-driven wind that have led to its status as a favored astrophysical host for the r-process. However, a critical impediment to the production of r-process elements occurs here in the neutrino-driven wind in the form of a reduction to the free neutron abundance.

Although neutrino interactions are initially beneficial in the development of the neutron-rich conditions needed for the r-process, a critical detriment occurs as a consequence of the neutrino-nucleon interaction $\nu_e + n \rightarrow p + e^-$. As free protons are quick to pair with an addition proton and two additional neutrons to form α particles, these reactions serve to drive the electron fraction towards 1/2,

$$Y_e \approx \frac{\lambda_{\nu_e}}{\lambda_{\bar{\nu}_e} + \lambda_{\nu_e}} + \frac{\lambda_{\bar{\nu}_e} - \lambda_{\nu_e}}{\lambda_{\bar{\nu}_e} + \lambda_{\nu_e}} \left(\frac{X_\alpha}{2} \right). \tag{1.22}$$

This is known as the α effect and was first discussed in Fuller and Meyer 1995 [50].

We discuss a possible resolution to the α effect through modifications to the standard picture of neutrino physics in the neutrino-driven wind environment in Chapters 2 and 3. In Chapter 2 this is accomplished through a physical mechanism, the transformation of ν_e neutrinos to a sterile flavor, ν_s, and in Chapter 3, we examine a reduction to the ν_e luminosity that is not tied to a specific physical mechanism. Both chapters center on the reduction of α particle formation by inhibiting the electron neutrino interaction, $\nu_e + n \rightarrow p + e^-$ and the resulting production of protons. This preserves the free neutron abundance that is necessary for r-process element formation by reducing the contribution to the electron fraction by the α particle abundance in Eq. 1.22.

The presence of a consistent pattern of r-process elements above $Z \geq 56$ has been found throughout the available halo star observational data [51]. The consistent pattern covers the region just after the second r-process peak through the third r-process peak region, as shown in Fig. 1.3. This data suggests that a mechanism is operating within the r-process to produce a robust abundance pattern. We explore the consequences of the presence of fission cycling during the r-process in Chapter 3 and find that under very neutron rich conditions that a robust r-process abundance

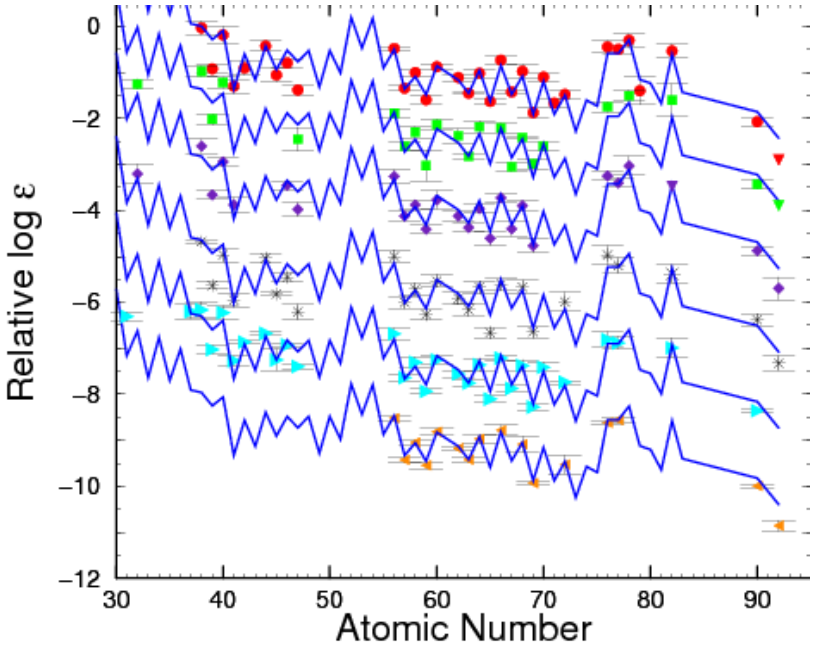


Figure 1.3: The abundance pattern of the r-process elements is consistent among the available halo star data between the second and third r-process peak regions and is in good agreement with the solar system r-process abundance pattern. The r-process abundance patterns of the most strongly-enhanced r-process metal-poor stars are shown as the various symbols. The solid line is the scaled solar r-process pattern. All patterns are arbitrarily offset vertically. Figure from Cowan 2007 [2].

pattern is found to emerge from the joint operation of both fission cycling and steady-β flow. The operation of these mechanisms allow for the r-process abundance pattern to be generated as a consequence of the underlying nuclear data of the r-process rather than the astrophysical conditions of the neutrino-driven wind. This allows a robust pattern of the r-process elements to form between the second and third r-process peak regions that is consistent over small variations in the astrophysical conditions.

The location of the r-process can extend near the neutron drip line during its formation, and $\gtrsim 3,000$ nuclei can play a role in the r-process [52]. Although some inroads have been made in obtaining the relevant experimental nuclear data for some of the relevant nuclei, experimental nuclear data is not available for many of the nuclei that participate in the r-process. In classical r-process studies, this deficiency is less critical as the use of the $(n,\gamma) \leftrightarrows (\gamma,n)$ equilibrium approximation during the

r-process shifts the nuclear data burden away from the neutron capture and photodissociation rates to the more tractable β-decay rates. This was previously taken to be acceptable as individual neutron capture rates were not thought to influence the abundance pattern of the r-process. However, in Chapter 4, we identify a nucleus, ^{130}Sn, whose neutron capture rate can impact the abundance pattern of the r-process. ^{130}Sn acts as a secondary waiting point and impacts the amount of material that travels through the $A = 130$ peak region, influencing the abundance pattern of the r-process.

Chapter 2

Active-Sterile Neutrino Oscillations and the r-process

We investigate nucleosynthesis in the supernovae post-core bounce neutrino-driven wind environment in the presence of active-sterile neutrino transformation. We consider active-sterile neutrino oscillations for a range of mixing parameters: vacuum mass-squared differences of $0.1\,\mathrm{eV}^2 \leq \delta m^2 \leq 100\,\mathrm{eV}^2$, and vacuum mixing angles of $\sin^2 2\theta_v \geq 10^{-4}$. We find a consistent r-process pattern for a large range of mixing parameters that is in rough agreement with the halo star CS 22892-052 abundances and the pattern shape is determined by fission cycling. We find that the allowed region for the formation of the r-process peaks overlaps the LSND and NSBL (3+1) allowed region.

2.1 Background

Neutrinos dominate both the dynamics and the nucleosynthesis in the region near the protoneutron star during a core collapse supernova. The prodigious neutrino flux generated here is thought to deposit enough energy to liberate material from the gravitational well of the protoneutron star. Neutrino capture produces a neutron-rich environment outside the protoneutron star at late times post-core bounce. Understanding the role of neutrinos in this environment directly leads to our understanding

of heavy element nucleosynthesis in the core collapse supernova environment.

One of the synthesis processes that may take place in this environment is the r-process, or rapid neutron capture process, which generates about half of the elements with atomic weight $A \geq 100$ [8]. At the heart of the r-process is the rapid capture of neutrons, which occurs much faster than the competing beta decay, forming very neutron rich nuclides. As the supply of free neutrons is exhausted, these nuclides decay back to beta stability, forming a characteristic r-process abundance pattern that can be observed today.

While this basic r-process mechanism is understood, finding the astrophysical location of the r-process proves more elusive. Several observational factors point towards the neutron-rich material produced near the protoneutron star of a core-collapse supernovae as a likely candidate, *e.g* [1, 53] . Sneden and Cowan 2003 [1] concluded the r-process abundance patterns in extremely metal poor giant stars match the second and third peaks of the solar system r-process pattern, indicating these elements were formed early in the evolution of the universe given these considerations [54]. The neutrino-driven wind of the core collaspe supernova is a promising candidate for the r-process, for a review see Wanajo et al. 2001 [26].

The evolution for a mass element which will eventually undergo an r-process in the neutrino-driven wind of the protoneutron star proceeds through several stages [21] Material first emerges from the surface of the protoneutron star as free nucleons, carried off by the neutrino-driven wind. The strong influence of neutrinos in this regime produces neutron rich material resulting from the equilibrium effects of the ν_e and $\overline{\nu}_e$ fluxes, as the $\overline{\nu}_e$'s are thought to have a longer mean free path at the surface of the protoneutron star and hence are more energetic. The larger ν_e opacity than $\overline{\nu}_e$ implies the $\overline{\nu}_e$'s decouple deeper in the core, and therefore have a deeper neutrinoshpere than the ν_e's. [42] As the mass element moves farther from the star, it reaches lower temperatures ($T < 750$ keV), the nucleons coalesce into α particles and a large abundance of free neutrons. The α particles then combine into seed nuclei for the r-process with $50 \lesssim A \lesssim 100$. Neutron capture begins at even lower temperatures ($T < 300$ keV) allowing the formation of r-process elements.

It has long been suggested that fission could influence the r-process [17], primarily

for cosmochronometers *e.g* [55] In sufficiently neutron-rich conditions, heavy elements which are unstable to fission can be produced, terminating the r-process path. Additionally, fission influences the r-process through the subsequent cycling of these fission unstable heavy elements by neutron capture on the fission products. Beta-delayed, neutron induced, and spontaneous fission are all thought to play important roles in determining the outcome of the final r-process abundances [56].

Early r-process models in the neutrino-driven wind environment, such as Woosley, et al, 1994 [20], accurately reproduced the r-process abundances without significant fission cycling; However, later models produced lower entropy per baryon, producing nearly but not quite all the requisite conditions. Further, proper consideration of the near inertness of alpha particles to neutrino interactions resulted in decreased neutronization, presenting a significant impediment to r-process production in this environment [57, 50, 58, 21, 59, 60].

There are three possible solutions for circumventing these problems. One solution is modifying the hydrodynamics by using a very fast dynamical timescale [58, 23] even in a proton-rich environment [61], or increasing temperature with high entropy [20]; however, it is not known how neutrino heating could generate such conditions. Another possibility is choosing a different location for the r-process to occur, such as a neutron-star merger [62, 63]. However this solution is not currently favored by analysis of the observational data [54]. Other astrophysical sites such as gamma ray burst accretion disks are currently being considered [30, 32].

The solution examined here is the introduction of active-sterile neutrino oscillations through the $\nu_e \leftrightarrows \nu_s$ and $\overline{\nu}_e \leftrightarrows \overline{\nu}_s$ channels. Two different types of terrestrial experiments place constraints on $\nu_e \leftrightarrows \nu_s$ and $\overline{\nu}_e \leftrightarrows \overline{\nu}_s$ transitions, reactor experiments and short baseline accelerator experiments. Relevant data of the former comes from CHOOZ [64] with it's null result on $\overline{\nu}_e$ disappearance, and the latter KARMEN, [65], with a null result on $\overline{\nu}_\mu \rightarrow \overline{\nu}_e$ appearance, leading to no indication of oscillations. LSND [66] is the only short baseline experiment which reported a positive signal for $\nu_e \rightarrow \nu_\mu$ and this data is used as motivation for a sterile neutrino.

Big Bang Nucleosynthesis(BBN) and the cosmic microwave background (CMB) can provide constraints on the existence of sterile neutrinos. The number of new

neutrino flavors, which would include a sterile neutrino, is restricted by the actions of the relativistic energy density limits during the BBN epoch while simultaneously accounting for the WMAP data, e.g. [67, 68]. This restriction may be lifted through flexibility in the electron neutrino asymmetry, ξ_e, which allows room for the addition of neutrinos beyond the standard model [69]. CMB also places bounds on the neutrino mass; however, these bounds are dependent on the thermal spectrum of the sterile neutrino [70]. At present, while they provide restrictions, the BBN and CMB analysis do not discount light sterile neutrinos.

We organize the paper as follows: In Section 2.2, we describe the neutrino driven wind model and general nucleosynthesis in the neutrino-driven wind. Section 2.3 describes matter-enhanced active-sterile neutrino oscillations and their effects on nucleosynthesis. Section 2.4 describes the network calculation of element abundances. In Section 2.5 we discuss the influence of fission in the r-process and how fission cycling links the second and third peaks of the r-process. Our results appear in Section 2.6 showing our calculation of nucleosynthesis with active-sterile neutrino oscillations and we compare with both the solar system and halo star abundances. We conclude in section 2.7.

2.2 Nucleosynthesis in the Neutrino Driven Wind

The neutrino-driven wind epoch begins several seconds after post-core bounce in the type II supernovae environment. The newborn protoneutron star undergoes Kelvin-Helmholtz cooling, radiating neutrinos that can lift material off the star's surface. This material is likely ejected by neutrino heating through charged-current reactions. It takes about ten neutrino interactions per nucleon to eject material from the surface of the star, and the neutrinos set the electron fraction, Y_e [42].

In our calculations we use a one-dimensional model to follow a mass element's peregrination from a nucleon at the surface of the protoneutron star to an ejected r-process element. Although multidimensional phenomena such as convection may operate in this environment, this simple model elucidates the effect of neutrino flavor transformation on nucleosynthesis.

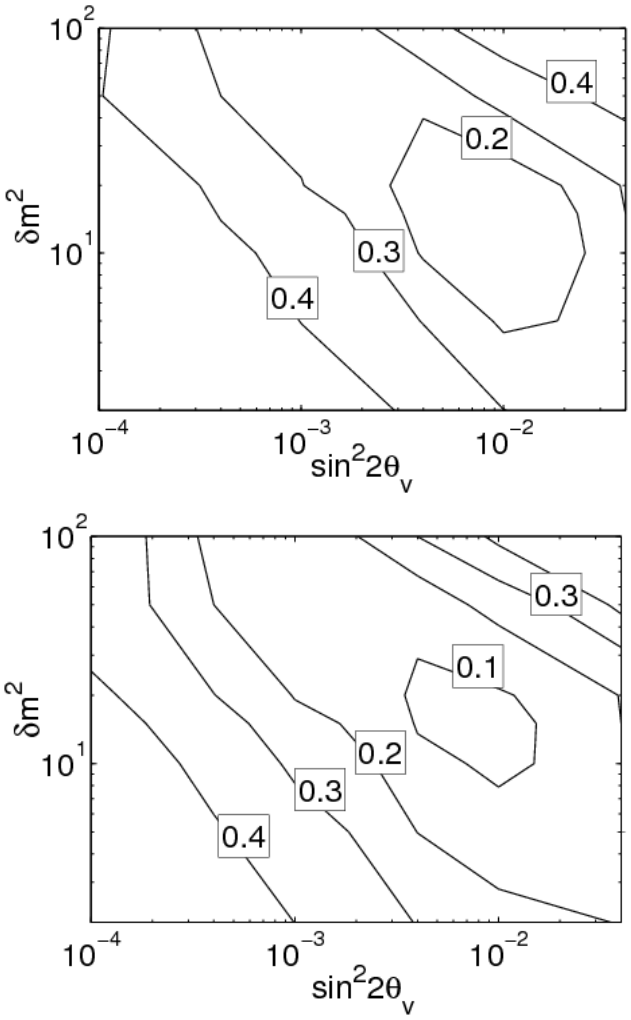


Figure 2.1: In the top panel we show the contours of electron fraction, Y_e, at the onset of rapid neutron capture, $T_{keV} \approx 200$. For the astrophysical conditions below, one expects an r-process for $Y_e \lesssim 0.35$ and an r-process which matches the observed ratio of peaks heights for $Y_e \lesssim 0.3$. For comparison with previous work, in the bottom right panel, we show the Y_e, earlier, at the onset of heavy element formation, $T_{keV} \approx 600$. Neutrino captures on free nucleons increase the electron fraction slightly, between $T_{keV} \approx 600$ and $T_{keV} \approx 200$. The neutrino-driven wind parameters are entropy per baryon of $S/k = 100$, expansion time scale of $\tau = 0.3\,s$, neutrino luminosities of $L_\nu = 10^{51}\,\mathrm{ergs\ s^{-1}}$ and $L_{\bar{\nu}} = 1.3 \times 10^{51}\,\mathrm{ergs\ s^{-1}}$, and neutrino temperatures $T_\nu = 3.5\,\mathrm{MeV}$ and $T_{\bar{\nu}} = 4.5\,\mathrm{MeV}$.

A parameterization of the neutrino-driven wind in the type II supernovae environment following from [20] results in a constant mass outflow rate ($\dot{M} = 4\pi r^2 \rho v$) with a homologous outflow with a radial velocity v of

$$v \propto r, \tag{2.1}$$

where r is the radial distance from the center of the protoneutron star. From this we find

$$r = r_o \exp(t/\tau), \tag{2.2}$$

where r_o is the initial radius and the expansion time scale, τ is defined as

$$\tau = r/v. \tag{2.3}$$

Including $\propto 1/r$ scaling for the enthalpy per baryon, the density ρ scales as

$$\rho \propto \rho_o \exp(-3t/\tau). \tag{2.4}$$

In our calculations we primarily use $\tau = 0.3\,\mathrm{s}$ and $S/k = 100$ unless otherwise stated. Our mass element leaves the surface of the protoneutron star in Nuclear Statistical Equilibrium (NSE) due to the very high temperature. At entropies of $S/k = 100$ baryonic content exists only as protons and neutrons [22]. Electron neutrino and anti-neutrino capture on free nucleons set the electron fraction and at the surface produce neutron-rich conditions. As material flows away from the protoneutron star it cools and once material reaches temperatures below $T \lesssim 750$ keV the formation of α particles begins.

During this epoch since neutrino interactions have created a neutron-rich environment, all the protons and many neutrons bind into α particles. Electron neutrinos capture on the remaining neutrons producing protons, which in turn consume more neutrons to form additional α particles. This drives the electron fraction towards $Y_e = 0.5$ decreasing the number of free neutrons and creating an environment unfavorable to the r-process, known as the α-effect [60, 50].

As the mass element continues moving away from the protoneutron star, the lower energies allow α particles and neutrons to combine into seed nuclei for the r-process. Farther away from the protoneutron star, as the material falls out of NSE, it undergoes a series of quasi-equilibrium phases [60, 44]. The large Coulomb barriers eventually become insurmountable and charged current reactions drop out of equilibrium, while a large abundance of free neutrons remains. The mass element continues to move outward leaving neutron capture (n,γ) and photo-dissociation (γ,n) as the only reactions left in equilibrium.

This $(n, \gamma) \rightleftharpoons (\gamma, n)$ equilibrium phase marks the onset of the r-process, as the balance between neutron capture and photo-dissociation determines the equilibrium path of the r-process. The r-process may produce nuclei unstable towards fission at this time, whose fission products may effect the r-process abundances. Once there are not enough free neutrons left to maintain $(n, \gamma) \rightleftharpoons (\gamma, n)$ equilibrium, neutron capture and photo-dissociation reactions freeze-out allowing the r-process nuclei to β-decay back to stability, forming the progenitors to the observed r-process elements.

2.3 Matter-Enhanced Active-Sterile Neutrino Oscillations

McLaughlin et al. 1999 [43] demonstrated that active-sterile neutrino transformation could circumvent the problematic issues associated with the r-process in the neutrino driven wind from the protoneutron star. Active-active neutrino transformation as well as active-sterile transformation through different channels has also been explored in Caldwell et al. 2000 [71] and Nunokawa et al. 1997 [72].

Here we consider matter enhanced transformation of neutrinos through the $\nu_e \leftrightarrows \nu_s$ and $\overline{\nu}_e \leftrightarrows \overline{\nu}_s$ channels as described by [43]. We define a sterile neutrino as one with interactions significantly weaker than the normal weak interaction. These interactions must be weak enough as to not contribute significantly to the decay rate of the Z° boson [73]. Our results are independent of the model which produces a light sterile neutrino, as any SU(2) standard model singlet could be a light sterile neutrino.

For the following equations we use Ψ_e for the electron neutrino wavefunctions and Ψ_s for the sterile neutrino wavefunctions. We consider evolution of flavor eigenstates in matter without the potential created by background neutrinos in the form [74]

$$i\hbar\frac{\partial}{\partial r}\begin{bmatrix}\Psi_e(r)\\ \\ \Psi_s(r)\end{bmatrix} = \begin{bmatrix}\phi_e(r) & \sqrt{\Lambda}\\ \\ \sqrt{\Lambda} & -\phi_e(r)\end{bmatrix}\begin{bmatrix}\Psi_e(r)\\ \\ \Psi_s(r)\end{bmatrix} \tag{2.5}$$

where

$$\phi_e(r) = \tfrac{1}{4E}(\pm 2\sqrt{2}G_F[N_e^-(r) - N_e^+(r) - \tfrac{N_n(r)}{2}]E - \delta m^2\cos 2\theta_v) \tag{2.6}$$

and

$$\sqrt{\Lambda} = \frac{\delta m^2}{4E}\sin 2\theta_v. \tag{2.7}$$

In equation (2.6), the positive sign designates electron neutrinos and the negative sign electron anti-neutrinos. Here, G_F is the Fermi constant and $N_e^-(r)$,$N_e^+(r)$, and $N_n(r)$ represent the number density for the electrons, positrons, and neutrons in the medium. The neutrino mixing angle is θ_v, and the vacuum mass-squared splitting term is defined as $\delta\mathrm{m}^2 \equiv m_2^2 - m_1^2$, where m_1 and m_2 are the masses of the mass eigenstates.

The potential is defined to be proportional to the net weak charge,

$$V(r) \equiv 2\sqrt{2}G_F[N_e^-(r) - N_e^+(r) - N_n(r)/2], \tag{2.8}$$

meaning neutrinos of energy

$$E_{res}(r) \equiv \pm\frac{\delta m^2\cos 2\theta_v}{V(r)} \tag{2.9}$$

undergo a Mikheyev-Smirnov-Wolfenstein (MSW) resonance at a positive (ν_e) or negative ($\overline{\nu}_e$) potential. Noting the electron fraction is

$$Y_e(r) = \frac{N_e^-(r) - N_e^+(r)}{N_p(r) - N_n(r)}, \tag{2.10}$$

we can immediately see how Y_e influences the sign of the potential,

$$V(r) = \frac{3G_F\rho(r)}{2\sqrt{2}m_N}\left(Y_e - \frac{1}{3}\right). \tag{2.11}$$

Electron neutrinos transform for a positive potential and electron anti-neutrinos for a negative potential. Above, $\rho(r)$ is the matter density a distance r away from the protoneutron star, m_N is nucleon mass, and $N_p(r)$ is the proton number density. Since the local material is electrically neutral we take $N_p = N_e^- - N_e^+$.

Using the above substitutions, we can rewrite equation (2.6) as

$$\phi_e(r) = \pm\frac{3G_F\rho(r)}{2\sqrt{2}m_N}\left(Y_e - \frac{1}{3}\right) - \frac{\delta m^2}{4E}\cos 2\theta_v. \tag{2.12}$$

Active-sterile MSW neutrino resonances occur when $\phi_e = 0$, providing a direct relationship to Y_e from the neutrino mixing parameters, δm^2 and $\sin^2 2\theta_\nu$ and the electron neutrino and anti-neutrino energies.

We calculate equation (2.5) numerically for neutrino survival probabilities passing through matter above the protoneutron star. We assume no flavor transformations occur until the neutrinos leave the surface of the protoneutron star, hence all neutrinos reside in the active flavor eigenstates, ν_e and $\overline{\nu}_e$, with no sterile mixing, ν_s and $\overline{\nu}_s$, at this time. We begin the neutrino transformation evolution with a Fermi-Dirac neutrino and anti-neutrino spectrum. As the neutrinos depart from the protoneutron star, the evolving survival probabilities from equation (2.5) cause the neutrinos to depart rapidly from this initial spectrum. We use electron neutrino and anti-neutrino luminosities of $L_\nu = 10^{51}$ ergs s^{-1} and $L_{\bar{\nu}} = 1.3 \times 10^{51}$ ergs s^{-1} respectively, electron neutrino and anti-neutrino temperatures of $T_\nu = 3.5$ MeV and $T_{\bar{\nu}} = 4.5$ MeV respectively, and an effective chemical potential of zero. We chose these values to be representative of the general qualitative behavior of the expected neutrino flavor transformation in this environment. For these luminosities, electron neutrinos and electron anti-neutrinos strongly determine the initial electron fraction, although additional influence on the electron fraction comes from electron and positron capture through the backward rates of the following reactions:

$$\nu_e + n \leftrightarrows p + e^-, \tag{2.13}$$

and

$$\bar{\nu_e} + p \leftrightarrows n + e^+. \tag{2.14}$$

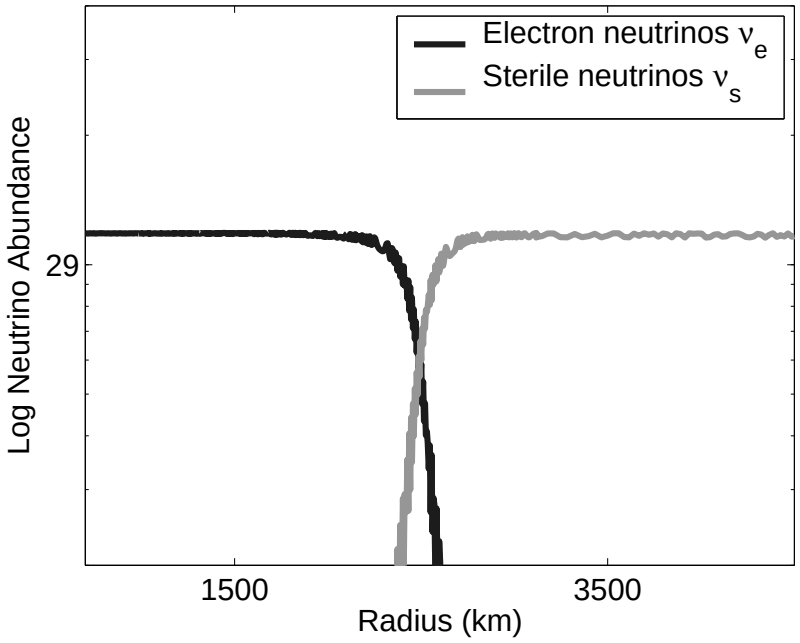


Figure 2.2: Electron neutrinos undergoing transformation to sterile neutrinos above the surface of the neutron star by active-sterile MSW neutrino transformation. The active-sterile neutrino mixing parameters are $\delta m^2 = 2\,\mathrm{eV}^2$ and $\sin^2 2\theta_v = 7 \times 10^{-2}$, with the wind parameters of Fig. 2.1. The neutrinos shown have energy $E_\nu \approx 11$ MeV.

We now point out the main features of active-sterile neutrino mixing in this environment: the detailed behavior of $\nu_e \leftrightarrows \nu_s$ mixing is discussed in [75, 43]. As neutrinos leave the surface of the protoneutron star, low energy electron neutrinos are the first to undergo transformation to sterile neutrinos, ν_s, due to the large potential, equation (2.11). Such a transformation is shown in Fig. 2.2. This reduces the efficacy on the forward rate of equation (2.13) lowering both the potential and the electron fraction, allowing progressively higher energy electron neutrinos to transform. Once the electron fraction drops below 1/3, the highest energy electron anti-neutrinos transform to sterile neutrinos due to the now negative potential. The potential continues to drop towards its minimum, after which it will ascend back towards its zero value. On its way back, upon the potential reaching this zero value, all of the electron anti-neutrinos above a threshold energy convert from $\overline{\nu}_s$'s back to $\overline{\nu}_e$'s. As the mass element reaches the alpha particle formation epoch, very few of the original electron neutrinos and

most of the original electron anti-neutrinos are present. This severely impedes the forward rate of equation (2.12) due to the lack of ν_e's, and also prevents the dramatic electron fraction rise associated with the α effect, allowing a neutron-rich neutron-to-proton ratio needed for r-process element formation. The suppression of the α effect is dependent on the neutrino mixing parameters, δm^2 and $\sin^2 2\theta_\nu$, and we describe later which parameters allow for r-process elements to be produced [43].

2.4 Network Calculations

We calculate the nuclide abundances for a mass element leaving the surface of a protoneutron star by linking three network calculations: a nuclear statistical equilibrium (NSE) code [43], a full reaction rate network code [44], and an r-process reaction network code [45]. Throughout the calculation we self-consistently solve the neutrino evolution through the integration of equation (2.5). In all regimes we are guided by the structure of the protoneutron star from [41], and from the wind as described in [45] as described in Sec. 2.2.

As the mass element first leaves the protoneutron star with $T_{MeV} \approx 3$, the NSE code takes distance and density and calculates all relevant thermodynamic quantities including positron and electron number densities. We use NSE to calculate the neutron, proton, and heavy element ($A > 40$) abundances. We also compute the weak reaction rates, generating an updated electron fraction, Y_e. This allows us to self-consistently solve the matter enhanced (MSW) equation and hence the neutrino survival probabilities.

Once the mass element leaves the NSE regime, at $T_{keV} \lesssim 900$, we use the full reaction-rate network to calculate the evolution of the mass element. In this regime intermediate nuclide production is accounted for, $A \lesssim 120$, utilizing strong, electromagnetic, and weak interactions rates from [46]. As before, we continue to use the updated electron fraction to self consistently calculate the MSW neutrino evolution.

As the mass element reaches the neutron capture regime where charged particle reactions have frozen out, we use an r-process reaction rate code, for $T_{keV} \lesssim 200$. The relevant nuclear reactions included are neutron capture, photo-disintegration, beta

decay, charged-current neutrino interactions, and beta-delayed neutron emission. We use the nuclear mass model from [76], β-decay rates from [49] and neutron capture rates from [46]. While this mass model is known to produce a gap after the second peak, we choose it since it is the largest self-consistent data set available. We include the effects of nuclei undergoing fission as it is relevant in this regime.

2.5 Fission in r-process Nucleosynthesis

It is important to understand which nuclides become unstable to fission and if and where fission terminates the r-process. Some previous works such as Cowan et al. 1999 [77] and Meyer 2002 [61] have included termination of the r-process through fission. Meyer 2002 [61] used a network termination boundary of Z = 91 from proton drip line to neutron drip line with only one isotope ^{275}Pa undergoing fission. Cowan et al. 1999 [77] employed a probability of unity for spontaneous fission for nuclei with atomic weight greater than 256. Other calculations such as Goriely et al. 2004 [34] and Panov and Thielemann 2004 [56], employed a set of fission rates over a range of heavy nuclei.

Perhaps even more important than which nuclei undergo fission is the role the nuclide distribution of the daughter products play. There are two fission modes generally considered, described by their daughter product distributions, symmetric and asymmetric. Symmetric fission results in the progenitor nucleus being split nearly in half by fission, resulting in daughter products of the same nuclide for even numbers of protons and neutrons in the progenitor and adjacent nuclides for odd permutations of protons and neutrons. For asymmetric fission, the progenitor nucleus splits unevenly, resulting in one daughter product being proportionally heavier than the other.

Cowan et al. 1999 [77] and Rauscher et al. 1994 [78] employ symmetrical fission, to determine the daughter products, while Panov and Thielmann 2004 [56] utilize a weighting function to determine the various daughter products. Ternary fission has been suggested as well [56]. At present, a consensus on the choice of fission daughter products has not been formed.

In this work we go one step beyond a single nucleus termination point. While

we terminate the network path at $A \geq 270$ by taking the probability of spontaneous fission to be unity above this point, we also include beta-delayed fission as well for nuclei ranging from $81 \leq Z \leq 100$ and $140 \leq N \leq 164$. Beta-delayed fission has the greatest importance during late stages of the r-process [56]. Our approach is sufficient to illustrate the qualitative impact of $\nu_e \leftrightarrows \nu_s$ transform on the r-process. For a detailed comparison on a nucleus by nucleus basis with data, it would be preferable to include neutron-induced fission as well. In the future, such rates may become available.

As stated above, the choice of fission daughter products can have a significant impact on the distribution of final r-process element abundances. We examined two models, symmetric fission where the two daughter products are taken to be as close to atomic weight and number as possible, and asymmetric fission using daughter products suggested by Ref. [17], which takes the daughter products to be about 40% and 60% of the mass of the progenitor nucleus.

2.6 Results and Discussion

It is convenient to cast our results in the form of both the electron fraction, $Y_e = p/(n+p)$, and abundance patterns to allow for direct comparison with previous theoretical and experimental results. We begin with a calculation of electron fraction, Y_e, since this is a key indicator of r-process element production in the neutrino-driven wind environment and it facilitates comparison with previous work over the neutrino mixing parameter region, δm^2 and $\sin^2 2\theta_\nu$. We then discuss the implications of our results and compare our calculated abundance patterns with both solar data [3, 4] and halo star data [79]. We also compare neutrino mixing parameters favorable to the r-process against the parameter region that will be probed by Mini-BooNE [5]. We pay particular attention to the effect of fission cycling since this process is a determining factor in the behavior of the system.

A key indicator of whether the r-process will occur is the electron fraction, Y_e, at the onset of neutron capture element formation. As described earlier, the α effect together with low entropy is a prominent cause of the reduction of free neutrons, stifling

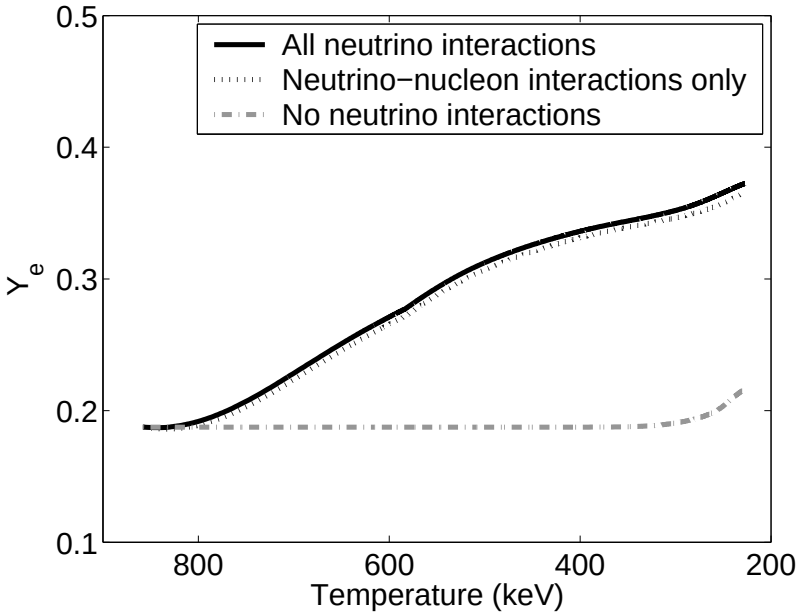


Figure 2.3: Electron fraction, Y_e is plotted vs. T_{keV} for the wind parameters in Fig. 2.1, with active-sterile neutrino mixing parameters of $\delta m^2 = 10\,\mathrm{eV}^2$ and $\sin^2 2\theta_v = 0.001$. The appropriate neutrino interactions are turned off at $T_{keV} = 850$ for the neutrino-nucleon interactions only and no neutrino interactions cases. The Y_e continues to increase even after heavy element formation, due primarily to neutrino-nucleon interactions.

the r-process. Active-sterile neutrino oscillations allow the α effect to be circumvented during the epoch of α particle formation as electron neutrinos are converted to their sterile counterparts, preventing electron neutrino capture on neutrons, and producing a neutron-rich environment.

Our reaction rate network self-consistently accounts for the evolution of Y_e throughout the duration of nucleosynthesis of the mass element. We begin by comparing Y_e with a previous calculation, Fig. 7 of Ref. [43], at the onset of heavy element formation (Fig. 2.1b) and find that good agreement is reached. Then we further track the Y_e up to the point of neutron capture element formation, $T_{keV} \approx 200$, and we find that for $Y_e \lesssim 0.35$ at this time, the environment is sufficiently neutron-rich for a r-process to occur (Fig. 2.1a).

We note there is a slight increase of Y_e between the two times, as shown between the two panels of Fig. 2.1. Since charged-current reactions affect the Y_e as the mass

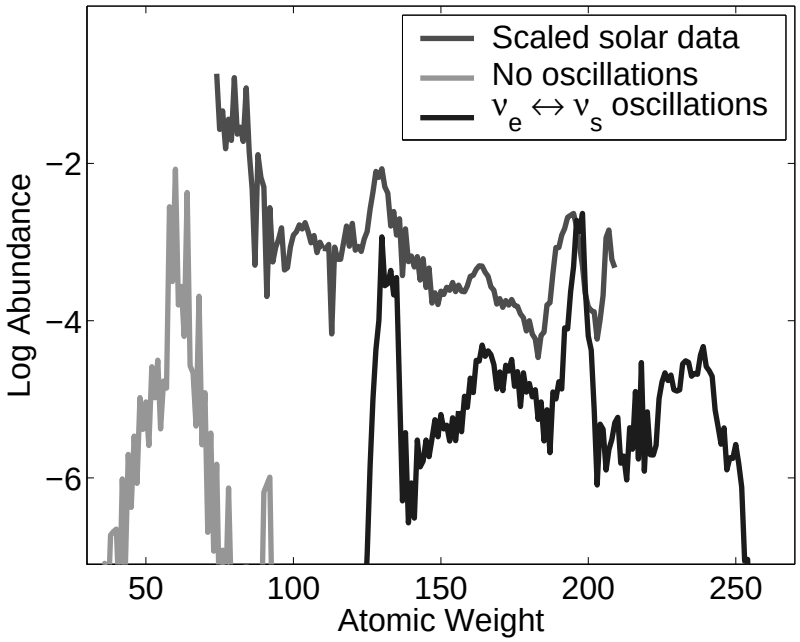


Figure 2.4: An r-process pattern (dark line) producing only the second and third of the three r-process peaks occurs in the neutrino-driven wind when there is active-sterile neutrino mixing. The dramatic impact of active-sterile neutrino oscillations on the r-process is seen immediately when contrasted against the abundances produced without neutrino mixing (light gray line). For the dark line neutrino mixing parameters of $\delta m^2 = 2\,\mathrm{eV}^2$ and $\sin^2 2\theta_v = 7 \times 10^{-2}$ are used together with same astrophysical conditions as in Fig. 2.1. The general features of the r-process pattern above $A \gtrsim 130$ found in solar system data [3] (medium gray line) are reproduced when $Y_e \lesssim 0.3$ at the onset of neutron capture element formation. The solar data is scaled to the simulation such that the sum of the $A = 195$ nuclides is 2.3×10^{-3}.

element moves farther away from the protoneutron star, the increase in Y_e must be the result of one or more charged-current reactions, electron neutrino capture on neutrons (the forward rate of equation (2.13)) increases Y_e, making the environment less neutron-rich. Although electron neutrinos that undergo transformation to sterile neutrinos do not affect the Y_e, not all electron neutrinos undergo transformation. The effect of these residual electron neutrinos is shown in Fig. 2.3, where we plot the electron fraction between heavy nucleus production and neutron capture element formation, for the neutrino mixing parameters of $\delta \mathrm{m}^2 = 10\,\mathrm{eV}^2$ and $\sin^2 2\theta_v = 0.001$ Electron neutrino capture on neutrons is therefore responsible for the increase in Y_e

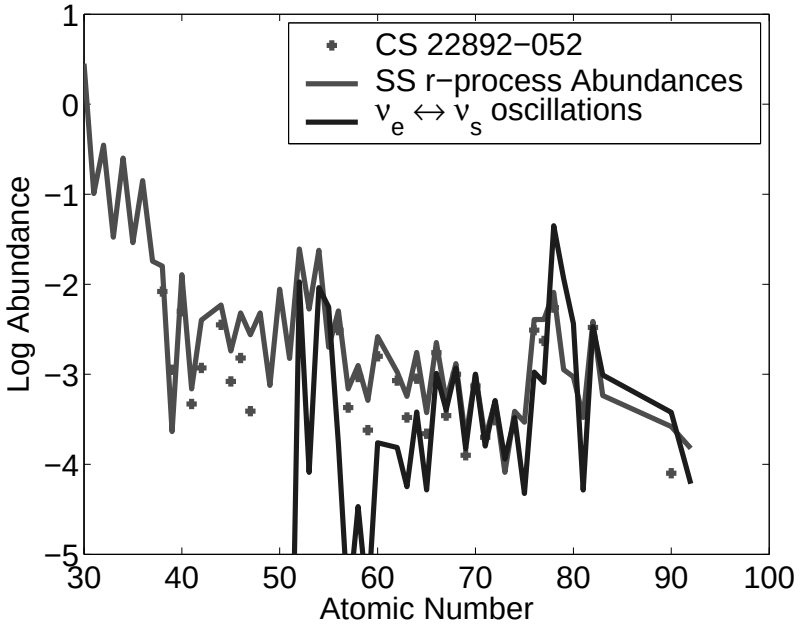


Figure 2.5: The general features of the r-process pattern found in halo stars are reproduced in the neutrino-driven wind when active-sterile neutrino oscillations occur. Only the second, $A \approx 130$ ($Z \approx 55$), third peaks, $A \approx 195$ ($Z \approx 80$), as well as the rare earth bump inbetween, are reproduced. The halo star CS 22892-052 [4] abundances are plotted for comparative purposes (dots) along with the solar system r-process abundances from [3] (dark line). Neutrino mixing parameters of $\delta m^2 = 2\,\mathrm{eV}^2$ and $\sin^2 2\theta_v = 7 \times 10^{-2}$ were used for the neutrino driven wind abundances (light line), although the pattern shown is fairly insensitive to the exact choice of mixing parameter (see Fig. 2.6). The astrophysical conditions are the same as in Fig 2.1. The measured abundances are scaled to the simulation such that the sum of the $Z = 70$ isotopes in each abundance curve have an abundance of 10^{-3}.

seen in Fig. 2.1.

In Fig. 2.4, we examine the consequences active-sterile neutrino oscillations have on abundance patterns in the neutrino-driven wind environment and find conditions suitable for the r-process in this environment for $Y_e \lesssim 0.35$. We note that none of our calculations reproduce the first r-process peak at $A \sim 80$. The resulting abundance pattern features the second and third r-process peaks and we note that the deficit after the second r-process peak, $A \sim 130$ is a consequence of the mass model we are using, Fig. 2.4 (dark line). The solar abundance of A = 195 is scaled to 2.3×10^{-3} for comparison.

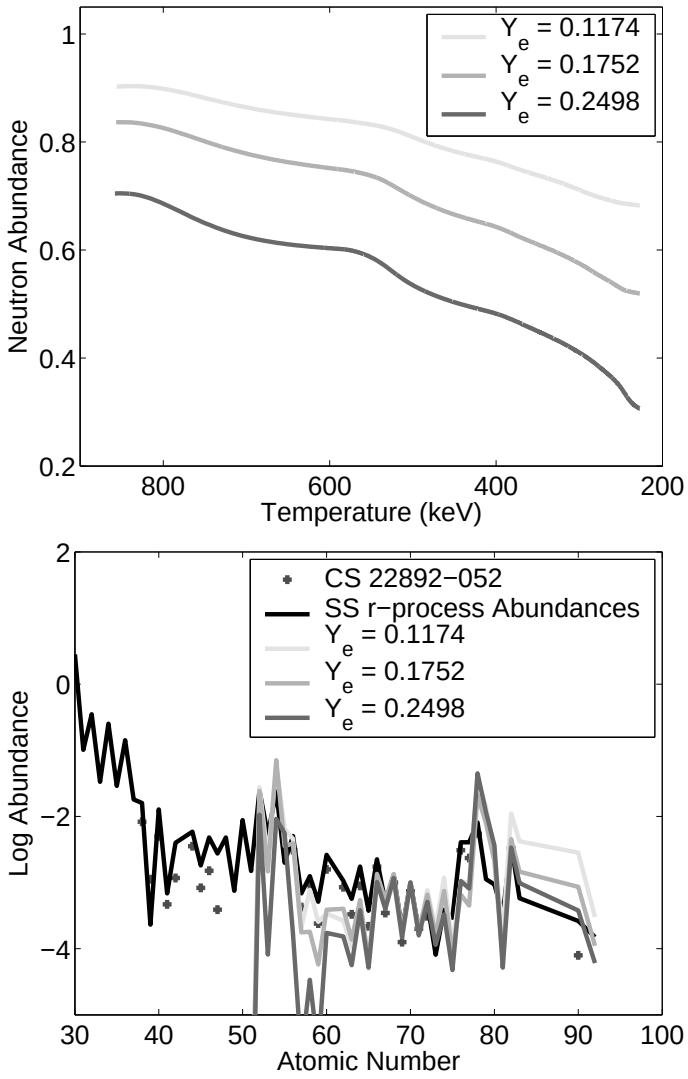


Figure 2.6: Fission cycling produces a consistent overall r-process pattern in the neutrino-driven wind, as long as $Y_e \lesssim 0.3$ at the onset of neutron capture element formation (bottom panel). In the top panel we show neutron abundance vs. T_{keV} for three sets of neutrino mixing parameters, $\delta m^2 = 10\,\mathrm{eV}^2$ and $\sin^2 2\theta_v = 10^{-2}$, $\delta m^2 = 5\,\mathrm{eV}^2$ and $\sin^2 2\theta_v = 10^{-2}$, and $\delta m^2 = 2\,\mathrm{eV}^2$ and $\sin^2 2\theta_v = 7 \times 10^{-2}$ corresponding to electron fractions of $Y_e = 0.1174$, $Y_e = 0.1752$, and $Y_e = 0.2498$ respectively. The Y_e in the legend occurs at the start of heavy element formation, $T_{keV} \approx 200$. Lower Y_e's lead to more neutrons but a similar abundance pattern. In the bottom panel we show the abundance patterns from the same mixing parameters as used in the top panel. The abundances curves and astrophysical conditions are the same as figure 2.5.

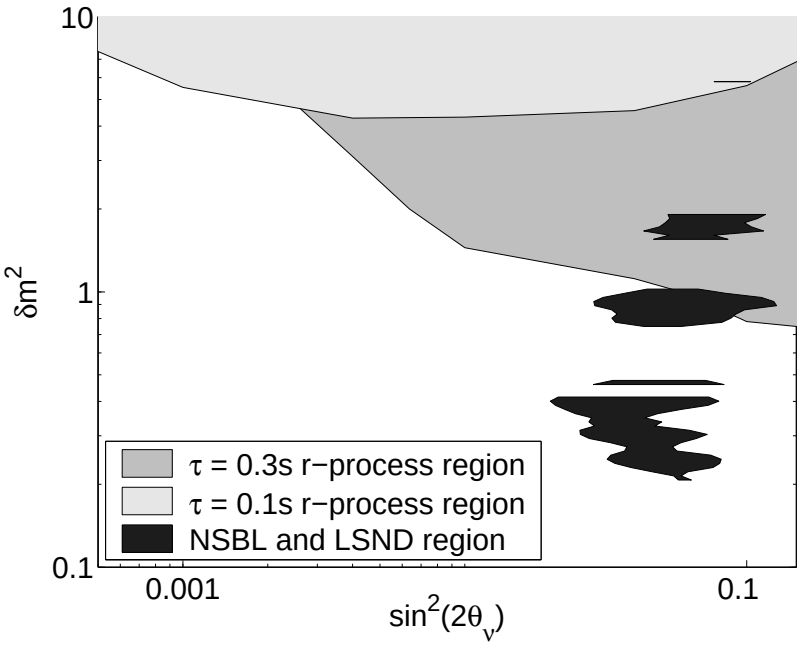


Figure 2.7: Contours indicating the parameter space for which we find an r-process (defined as $Y_e \lesssim 0.35$) in the prospective neutrino mixing parameter range of MiniBooNE. The light gray region signifies an r-process for an outflow timescale of $\tau = 0.1\,s$, and similarly the dark gray region for $\tau = 0.3\,s$, with a reminder of the astrophysical conditions listed in Fig. 2.1. The black region is the combined NSBL and LSND 90% CL allowed region [5]. The parameter space which produces a successful r-process is much larger than the space probed by experiment.

We classify our abundance patterns by Y_e at the onset of neutron capture element formation [80]. For $0.35 \gtrsim Y_e \gtrsim 0.30$, there are too few free neutrons to produce the third r-process peak, $A \sim 195$, with the same proportions as the second r-process peak, $A \sim 130$, as is indicated by observational data. Electron fractions of $Y_e \lesssim 0.3$ lead to conditions sufficiently neutron-rich to have the second and third r-process peaks in similar proportions to the observational data. Y_e lower than $Y_e \leq 0.25$ produces r-process elements around $A \gtrsim 250$ that are strongly susceptible to fission, which can in turn repopulate regions at and around the $A \sim 130$ peak. We will return to this fission cycling in the following section. Fig. 2.5 shows our abundance pattern plotted as a function of proton number, further demonstrating the second and third r-process peak production. The three abundances are scaled such that $Z = 70$ has

an abundance of 10^{-3}.

Early calculations reproduced the general features of the solar system r-process pattern by constructing a final r-process abundance pattern through a mass weighted average of individual abundances patterns resulting multiple mass trajectories [20, 19, 21]. We have investigated different wind conditions, including changes in neutrino luminosity and outflow timescale. The effect of varying the outflow timescale is shifting the range of neutrino mixing parameters, δm^2 and $\sin^2 2\theta$, for which a successful r-process occurs. The effect of reducing the neutrino luminosity is contracting the range of the neutrino mixing parameters yielding a successful r-process. While we find the absence of an $A \sim 80$ peak for a wide range of conditions, it would be necessary to calculate a time integrated history over a particular series of wind conditions to determine in a given neutrino driven wind model produces a significant first r-process peak.

Additionally, a multidimensional wind model could influence the abundance pattern in several ways. It could adjust the period which the mass element lingers in the α-particle formation epoch, longer periods leading to more exposure to ν_e's and hence less neutron-rich conditions. The alteration of thermodynamic quantities, such as temperature and density, between NSE and nuclear freeze-out epochs would change the nuclear composition at any stage. For example, the abundance pattern of the r-process is dependent on these freeze-out conditions.

The choice of neutrino mixing parameters affects the free neutron abundance and hence the electron fraction at the time of neutron capture element formation. We find that fission cycling is a mechanism for generating a stable r-process pattern once a threshold Y_e is reached, $Y_e \leq 0.25$ in our environment. All neutrino mixing parameters which are below this Y_e produce the same general r-process pattern, shown in Fig. 2.6.

Fission cycling behaves as a mechanism linking the second and third peaks of the r-process. As very heavy nuclides are produced, $A \gtrsim 250$, they may become unstable towards fission and provide an effective termination point to the r-process path. The resulting daughter nuclides from this fission repopulate abundances of the second r-process peak.

The consistency of the r-process pattern is dependent on the equilibrium path of the r-process. Early studies analyzing the mass numbers of both the peaks and the closed neutron shells, yielded a r-process path well away from the neutron-drip line. In general the equilibrium path of the r-process is determined by the balance between neutron capture and photo-dissociation for particular temperature and density conditions. In our calculations the environment becomes sufficiently neutron-rich to generate a r-process path along the neutron-drip line, resulting in a consistent r-process abundance pattern of the second and third peaks.

In the remainder of this section we discuss some details about the effects of fission. It is difficult to make any definitive comments on the specific effects that spontaneous fission and beta-delayed fission have on particular final r-process nuclide abundances due to uncertainties in fission models; however, some general comments are warranted. The impact of fission is greatest in the regimes around the $A \sim 130$ peak and past the $A \sim 195$ peak, the regimes where fission deposition and depletion occurs.

The details of the pattern around the $A \sim 130$ peak is caused by the deposition of fission daughter products, which in turn are strongly affected by the choice of fission daughter product distribution, in the region of $120 \lesssim A \lesssim 140$. Two modes of daughter product distributions that we examined are symmetric and asymmetric as described in Ref. [17]. Symmetric fission modes generally produce an abundance pattern similar to that produced by an r-process calculation without fission, since material is mostly deposited near the closed neutron shell region of the $A \sim 130$ peak; however, asymmetric modes can make significant material deposits into the $A \sim 100$ region and erase the deficit past the $A \sim 130$ peak. It has been suggested that fission could form elements $A \leq 120$ in metal poor stars previously, *e.g.* Ref. [56].

Abundance structure of the depletion region past the $A \sim 195$ peak is strongly affected by several factors. These factors are the amount of material that reaches this region, how strongly fission depletion occurs, and for what elements it occurs. Most previous work on fission in the r-process involves calculations which effectively terminate the r-process using a 100% fission probablity in the regime of $260 \lesssim A \lesssim 280$. Given that the nuclear physics of such neutron-rich nuclei is not well understood, it is

difficult to draw conclusions about any detailed features in this region. Nevertheless, fission cycling produces a distinct and stable abundance pattern with overall features that are in agreement with data.

Halo stars, by virtue of their ancient nature, give us a glimpse of the abundances from the earliest r-process progenitors. The similarity between the r-process pattern in halo stars and that seen in the solar r-process suggests a single extremely consistent r-process mechanism is operating for the heavier r-process elements. We present our abundance pattern for comparison with the halo star CS 22892-052 [79, 3] and the solar system r-process [4] in Fig. 2.5 and Fig. 2.6. There is rough agreement between our data, Fig. 2.5 (black line), and CS 22982-052, Fig. 2.5 (dots), between $50 \lesssim Z \lesssim 80$ the region of the second and third r-process peaks. The gap after the $Z \sim 50$ peak is the same as the gap after $A \sim 135$ in the previous plot, shown in Fig. 2.5 and is feature of the mass model we are using. Our final abundances are allowed to decay over a timescale of 14 Gyr, using decay modes and lifetimes from Ref. [81]. This is consistent with the overall chronometric estimate of r-process elements from CS 22982-052 [79]. Recent estimates of the age of the universe is $13.73^{+0.13}_{-0.17}$ Gyr from WMAP [82] and the galactic globular cluster age is $12.6^{+3.4}_{-2.2}$ Gyr [83]. The decay timescale primarily affects the abundances of Th^{232} and U^{238} since their half-lives are the shortest of the long lived quasi-stable elements. Using a decay timescale of 12 Gyr produces the same overall abundance patterns found in Fig. 2.5 and Fig. 2.6 with the largest differences being a 4% abundance increase in Th^{232}, and a 13% abundance increase in U^{238}. The rest of the quasi-stable elements, such as Rb^{37}, La^{138}, Sm^{147}, Lu^{176}, Re^{187}, and Pt^{190}, have less than a 2% abundance change.

The Mini-BooNE experiment is designed to study neutrino mixing in the range of the positive LSND result. One possible implication of this result is the existence of a sterile neutrino. In such a scenario the range of mixing parameters yielding a successful r-process in our calculations overlaps with the parameter range of Mini-BooNE. In Fig. 2.7, we compare our r-process allowed region for two outflow timescales, $\tau = 0.1\,\mathrm{s}$ and $\tau = 0.3\,\mathrm{s}$, with the combined null-short baseline (NSBL) and liquid scintillator neutron detector (LSND) (3+1) 99% confidence level (CL) data, with lower CL regions naturally residing inside the 99% region. A compilation of the NSBL and LSND

data is described in detail in Ref. [5]. It should be noted that several factors impact the location of the r-process region and hence any compatibility with the NSBL and LSND data. The choice of expansion timescale, τ, alters the electron fraction and shifts the points where active-sterile MSW flavor transformation occurs.

Finally, we caution that the inclusion of the neutrino background terms in the weak potential can significantly change the r-process abundances [75]. However, at late times the luminosity decreases, decreasing the effect of background terms [75]. In our calculations which do not include the background, we find that a reduced electron neutrino luminosity of $L_\nu = 5 \times 10^{50}\,\mathrm{ergs\ s^{-1}}$ and a reduced electron anti-neutrino luminosity of $L_{\bar{\nu}} = 6.5 \times 10^{50}\,\mathrm{ergs\ s^{-1}}$ can still yield a robust r-process solution. Future studies of neutrino transformation fully inclusive of background terms done together a hydrodynamical wind calculation will determine the extent to which r-process nucleosynthesis products will be produced and also escape the star.

2.7 Conclusions

We have examined nucleosynthesis in the neutrino-driven wind in the post-core bounce supernovae environment. We find that inclusion of active-sterile neutrino transformation yields an r-process pattern where only the second and third of the r-process peaks are produced for a broad range of neutrino mixing parameters. Analysis of data from halo stars has suggested that there are at least two separate types of events which make r-process nuclei [1]. Further-more the analysis suggests one of these mechanisms operates early in the evolution of the universe and makes primarily the second and third r-process peaks.

Fission cycling is responsible for the establishment of a stable r-process pattern. As long as many neutrons exist during the phase of neutron capture, nuclei are created with sufficiently high mass number that they are unstable to fission. Below a threshold ($Y_e \lesssim 0.3$) in our model the resulting abundance pattern is not sensitive to the magnitude of the free neutron abundance and therefore the number of times the fission cycle occurs.

We find our allowed r-process region has overlap with the parameter space to be

probed by the Mini-BooNE experiment. The extent of this overlap is dependent on uncertainties in the astrophysical environment and in the neutrino transformation calculations; however, the existence of a sterile neutrino in the parameters space that will be probed by Mini-BooNE will directly influence element production in core-collapse supernova.

Chapter 3

Fission Cycling in a Supernova r-process

Recent halo star abundance observations exhibit an important feature of consequence to the r-process: the presence of a main r-process between the second and third peaks which is consistent among halo stars. We explore fission cycling and steady-β flow as the driving mechanisms behind this feature. The presence of fission cycling during the r-process can account for nucleosynthesis yields between the second and third peaks, whereas the presence of steady-β flow can account for consistent r-process patterns, robust under small variations in astrophysical conditions. We employ the neutrino-driven wind of the core-collapse supernova to examine fission cycling and steady-β flow in the r-process. As the traditional neutrino-driven wind model does not produce the required very neutron-rich conditions for these mechanisms, we examine changes to the neutrino physics necessary for fission cycling to occur in the neutrino-driven wind environment, and we explore under what conditions steady-β flow is obtained.

3.1 Background

The production of neutron capture elements early in the universe is recorded in the abundances of Galactic halo stars. The two mechanisms responsible for generating

most neutron capture elements are the r-process and the s-process, with the r-process generating about half of the nuclides with $A \gtrsim 100$ [8, 9, 12]. The observed r-process abundance distribution in metal-poor halo stars diverges above and below $Z \approx 58$ into two distinct patterns [84, 51, 85, 4, 86, 87, 88, 89, 79, 90, 91, 92]. These patterns are defined by their consistency with the solar and halo star r-process abundances. The low r-process pattern ($Z \lesssim 58$) may result from the contributions of a light element production process (LEPP), see *e.g.* Montes et al. 2007 [93] for additional discussion. The high abundance ($58 \lesssim Z \lesssim 76$) pattern, known as the main r-process, is very consistent among both the available halo star data and the solar system r-process abundances [94, 95]. We suggest the existence of a main r-process implies that a robust mechanism is producing elements from the second ($A \approx 130$) through the third ($A \approx 195$) r-process peak region [96, 97].

While there has been success in observing the abundance fingerprints of the r-process, determining the astrophysical production site(s) remains an open question [62, 19, 20, 98, 99, 34]. A promising candidate site for the r-process is the neutrino-driven wind of the post-bounce core-collapse supernova, as the amount of r-process material ejected can account for the Galactic abundances [20, 26]. Also, the frequency of the core-collapse supernova event is sufficiently rapid to produce r-process material early in the universe, in accordance with the r-process abundances observed in very metal-poor stars [54]. However, traditional models of the neutrino-driven wind do not quite yield an r-process due to the low free neutron abundance at the r-process epoch [58, 27].

The r-process requires a neutron-to-seed ratio of $R \gtrsim 100$ for production of the heaviest, $A \approx 195$, peak [12]. Uncertainties in the wind model may be responsible for this shortcoming as R is related to both the entropy, S, and the dynamical timescale, τ, and both are sensitive to the the proto-neutron star physics, see *e.g.* [11]; an increase of S and a decrease of τ both lead to a higher initial neutron-to-seed ratio, R [58]. These changes would likely require a compact and/or massive proto-neutron star [22, 27, 23, 24, 26]. Additional studies have looked to a prompt supernova explosion mechanism for producing the neutron-rich conditions necessary for the r-process [28, 29], although the physical realization of a prompt explosion scenario

remains uncertain [100, 101].

An avenue that has been suggested for generating a suitable neutron-to-seed ratio is a shocked wind solution. A supersonic wind expansion, reducing seed formation during the α-particle formation epoch, is followed by a deceleration at late times [102, 27] which allows the remaining free neutrons to be fully reincorporated into the r-process. Recent r-process models in this supersonic outflow scenario can reproduce the solar system abundances, but require an artificially high neutron-to-proton ratio [103]. Alternate wind solutions generated solely by magnetic fields or acoustic waves, *e.g.* [104, 105], also do not appear to produce a high enough neutron-to-seed ratio for an r-process. Given these difficulties, alternative sites remain viable candidates, including neutron star mergers [99] and gamma ray bursts [30, 31].

In the neutrino-driven wind environment, charged-current neutrino reactions on both nucleons and nuclei determine the neutron-to-seed ratio for the r-process. The relevant neutrino interactions on nucleons are

$$\nu_e + \mathrm{n} \rightleftharpoons \mathrm{p} + e^-, \tag{3.1}$$

$$\bar{\nu}_e + \mathrm{p} \rightleftharpoons \mathrm{n} + e^+. \tag{3.2}$$

For example, when electron anti-neutrino capture creating neutrons, Eqn. 3.1, is favored over electron neutrino capture creating protons, Eqn. 3.2, a higher neutron-to-proton ratio results. These reactions are sensitive to the hardness of the electron neutrino and anti-neutrino spectra, which we parameterize by the effective electron neutrino and anti-neutrino temperature, T_{ν_e} and $T_{\bar{\nu}_e}$, the electron neutrino and anti-neutrino luminosity, L_{ν_e} and $L_{\bar{\nu}_e}$, and the distance from the center of the proto-neutron star. An analytic form of these neutrino-nucleon capture rates is found in [59]. Neutrino-nucleon reactions are responsible for the "alpha" effect, a critical detriment to the r-process in the presence of a high electron neutrino flux during the α-particle formation epoch [50, 59, 60]. There have been several physical modifications proposed to reduce the efficacy of the "alpha" effect; for instance, a fast outflow wind [58] or active-sterile neutrino oscillations [43, 75, 106] lead to a successful r-process. Both mechanisms reduce the capture of free neutrons by electron neutrinos during the α-particle formation epoch, allowing for a successful r-process.

When classifying the neutron richness of the r-process, we employ the electron fraction:

$$Y_e = \frac{N_p}{N_p + N_n}, \tag{3.3}$$

where N_n and N_p are the total neutron and proton number densities including both free nucleons and those in nuclei. The neutron-to-proton ratio may be taken as N_n/N_p. Environments with a low electron fraction have the high free neutron densities necessary to drive the rapid capture of neutrons onto seed nuclei, generating increasingly heavier nuclides by atomic weight, A. During the r-process, these nuclei capture neutrons, become increasingly beta unstable, and undergo β-decay to proceed to a larger atomic number, Z. After β-decay, the nuclide can again capture neutrons and the cycle repeats. As the supply of free neutrons dwindles, the nuclides decay back to β-stability. The union of rapid neutron capture and β-decay results in an abundance pattern distinguished by large peak features at $A \approx 80,\ 130$ and, 195, the first, second, and third peaks respectively. These peaks correspond to the closed shell nuclei with slow β-decay rates, creating "waiting points", causing material to accumulate at these points.

Abundances of the second and third r-process peaks, and the intermediate nuclei between them, are defined by the nuclear properties of the r-process under conditions where both steady β-flow and fission cycling persist [17]. Fission cycling occurs for sufficiently neutron-rich conditions where the r-process extends to nuclides that can decay through fission channels. Fission impacts the r-process by terminating the path near the trans-uranium region. This termination results in material returning to the $A \approx 130$ peak [107]. If neutron-rich conditions persist, these fission products effectively become new seed nuclei for the r-process, facilitating steady β-flow.

Once a sufficient supply of both neutrons and seed nuclei are available, steady-β flow correlates the r-process abundances to their inverse β-decay rates, see *e.g.* [10] for further discussion. The individual abundances in N along an isotopic chain are determined by (n,γ) $\rightleftarrows$ (γ,n) equilibrium. These correlated abundances span two or more of the closed-shell regions, and when occurring between the second, $A \approx 130$, and third, $A \approx 195$, r-process peaks, are a set of isotopic chains between $58 \lesssim Z \lesssim 76$.

The Z of the last chain is determined by fission. The first and last chains are linked as material leaving the last chain becomes the seed nuclides for the first chain through fission cycling. The rate change of the total abundance of an isotopic chain, $Y(Z)$, is the difference between material entering and exiting the chain by β-decay,

$$\begin{aligned} \dot{Y}(Z) &= \sum_{A} Y(Z-1,A)\lambda_{\beta}(Z-1,A) \\ &\quad - \sum_{A} Y(Z)\lambda_{\beta}(Z,A). \end{aligned} \tag{3.4}$$

Above, the individual abundances of an isotopic chain are $Y(Z,A)$, and the individual β-decay rates are $\lambda_{\beta}(Z,A)$. If both (n,γ) $\rightleftarrows$ (γ,n) equilibrium and re-population of the seed nuclei persist, the flow of material between isotopic chains reaches a steady-state configuration and the abundances and β-decay rates of each isotopic chain are inversely related as:

$$\sum_{A} Y(Z,A)\lambda_{\beta}(Z,A) = \text{const.} \tag{3.5}$$

This is known as the steady β-flow condition.

Here we examine fission cycling and steady-β flow mechanisms and discuss their impact on the r-process in the neutrino-driven wind. We also explore changes to the neutrino physics, independent of a physical generator, that lead to environments where fission cycling and steady-β flow mechanisms are present in the neutrino-driven wind. In section 3.2, we describe the details of our calculation in the neutrino-driven wind. In section 3.3 we describe how fission cycling influences the r-process. Section 3.4 describes how steady-β flow leads to a robust r-process pattern. In section 3.5 we detail how the neutrino spectrum influences the r-process environment. In section 3.6, we summarize the results.

3.2 Description of Nucleosynthesis Modeling

The neutrino-driven wind forms several seconds post-core bounce in the core-collapse supernova environment, and a one-dimensional wind model is often employed to describe the abundance composition of the isotropic outflow [20, 108].

Two-dimensional wind models have been employed previously; however, these calculations do not self-consistently account for neutrino interactions, necessitating the use of an artificial Y_e [109]. Here we follow the same wind parameterization as [106]. Unless otherwise noted, our calculations use an entropy per baryon of $s/k = 100$, an outflow timescale of $\tau = 0.3$ s, an initial density of $\rho_o \approx 1.7 \times 10^8$ g/cm^3, and an initial radius of $r_7 \approx 0.1$, in units of 10^7 cm.

We track the abundance composition of a mass element, following ejection from the proton-neutron star, using three coupled reaction networks. The element is initially in Nuclear Statistical Equilibrium (NSE), and we follow it using a NSE network [43] until α-particles begin to form, $T_9 \approx 10$, where T_9 is in units of 10^9 K. Next, we track the mass element throughout α-particle formation with an intermediate network calculation [44] that includes strong and electromagnetic rates tabulated by [46]. We have added electron-capture, positron-capture, neutrino-capture, and anti-neutrino-capture rates from [110] to both networks. As material reaches the r-process epoch, $T_9 \approx 2.5$, we use an r-process network [45, 111] that handles the relevant reactions of β-decay, β-delayed neutron emission, neutron capture, and photo-disintegration, and we include charged-current neutrino interactions. We use β-decay rates and neutron separations from [48], neutron capture rates from [46], and neutrino-capture rates from [110]. A complete description of the network calculation can be found in [106].

3.3 Fission Cycling

Fission decay joins β-decay, neutron capture, and photo-dissociation as a primary reaction channel for r-process nuclides near the trans-uranium region, as previously mentioned. Nuclei that undergo fission provide a termination point for the r-process by preventing the production of heavier nuclides past this region. After the nuclide undergoes fission, it fragments into smaller nuclides that rejoin the r-process in the $A \approx 130$ region. This leads to fission cycling, with the fission daughter products acting as seed nuclei for the r-process.

A knowledge of both the location of fission and the resultant distribution of fission fragments are necessary for detailed calculations of the r-process in very neutron-rich

environments. Treatments of fission in the r-process [55, 78, 77, 112] have been limited to largely phenomenological methods since there are few measurements of the fission properties for neutron-rich heavy nuclides. This current study is concerned with the general effects of fission on the r-process. We employ β-delayed fission probabilities from [113] which are relevant to our mass model and astrophysical conditions. We indirectly include the effects of neutron-induced fission, as no complete and consistent set of neutron-induced rates is available, by employing a spontaneous fission region for $A \gtrsim 270$, where all of the nuclides instantaneously fission, following previous treatments described in [114]. We implement fission by depopulating the parent fission nuclide into its appropriate daughter nuclides at the end of each timestep in our network code. The effects of neutrino-induced fission are small and are not included [115, 116]. We employ phenomenological fission distributions, following previous studies described in [114], to elucidate the primary effects fission cycling has on the r-process pattern. We also include fission-induced neutron emission when noted, implementing a piecewise linear fit of the values from [117]. We treat the emitted neutrons as becoming immediately thermalized with the surrounding medium.

As the fission material is re-incorporated in the $A \approx 130$ peak, this material experiences "waiting points" and accumulates here as β-decay is necessary for material to move from one isotopic (Z) chain to the next ($Z+1$) chain. The material is initially compacted together in atomic mass space, A, and then disperses through β-decay. Note that some material remains in each peak region during the fission cycling process as β-decay does not fully deplete each peak.

To examine the accumulation of material during this β-decay dispersion process, we compare abundances in the second and third r-process peaks,

$$R_{\rm peak} = \frac{\sum_{A=190}^{200} Y(A)}{\sum_{A=125}^{135} Y(A)}. \tag{3.6}$$

Figure 3.1 demonstrates $R_{\rm peak}$ for a range of Y_e. The Y_e is from the start of of the r-process epoch. Each point represents an individual nucleosynthesis outcome

resulting from a unique choice of electron neutrino and anti-neutrino luminosities in the neutrino-driven wind. The left-most portion ($Y_e \gtrsim 0.3$) of Fig. 3.1, where $R_{\rm peak}$ is zero, denotes where final r-process abundances extend from the second peak and up to the rare earth region. The first bump, at $Y_e \approx 0.3$, denotes patterns where the heaviest r-process nuclides occupy the third peak and have partially left the second peak. Once past this bump, the heaviest r-process nuclides are beyond the third peak and have reached the fission region, and re-incorporate into the second peak.

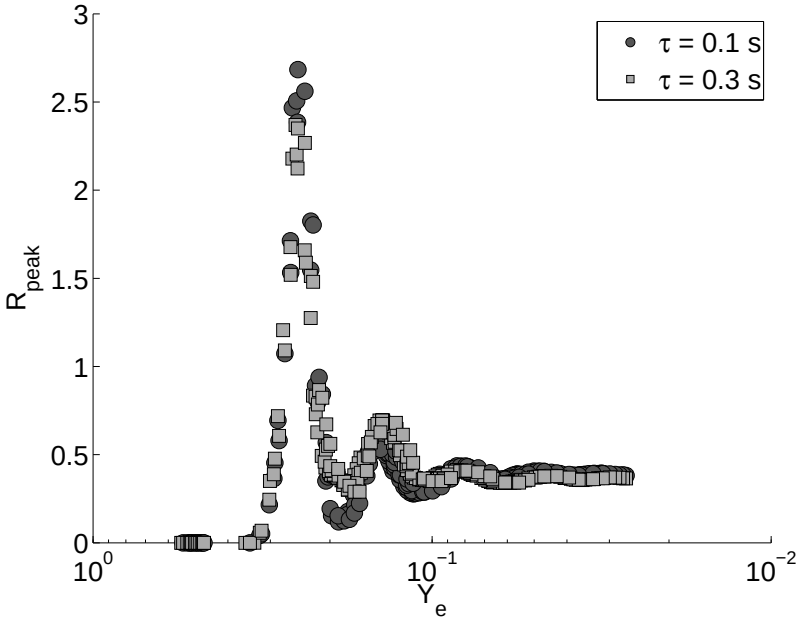


Figure 3.1: The final $R_{\rm peak}$ (Eqn. 3.6) resulting from a symmetric fission distribution for two different outflow timescales, $\tau = 0.1$ s (circles) and $\tau = 0.3$ s (squares), is shown for a variety of electron fractions, Y_e. For very neutron-rich conditions, $Y_e \lesssim 0.1$, a consistent r-process pattern forms between the second, $A \approx 130$, and third, $A \approx 195$, peak region. Fission cycling during the r-process links the second and third peaks, as material that captures out of the third peak reaches the fission regime. The resulting fission daughter products then rejoin the r-process at the second peak.

The behavior of fission under very neutron-rich conditions can be quantified by the number of fission cycles. When a nuclide fissions, there is an increase of heavy nuclei in abundance as multiple daughter nuclides are produced. The doubling of the

total abundance is a fission cycle,

$$\Lambda = \log_2(Y_{end}) - \log_2(Y_{start}), \tag{3.7}$$

where Λ is the number of fission cycles and Y_{start} and Y_{end} are the total abundance before and after fission cycling respectively. The relationship between the electron fraction, Y_e, and both the number of fission cycles and neutron-to-seed ratio at the start of the r-process epoch is shown in Fig. 3.2 for our baseline calculation as described in Sec. II. The number of free neutrons per seed nuclei is influenced by the location of the fission termination point of the r-process. For our standard calculation, we find fission cycling initially occurs for a neutron-to-seed ratio $\gtrsim 200$, consistent with previous studies, *e*.g. Meyer et al. 1997 [80].

In Fig. 3.1, cycles occur at the minima past each bump and extend to the next minima. For example, the first fission cycle ranges from the minima at $Y_e \approx 0.17$ to the minima at $Y_e \approx 0.09$. Significant fission cycling occurs for increasingly neutron-rich conditions, and, under very neutron-rich conditions, the movement of material entering and leaving a peak reaches equilibrium, a consequence of steady β-flow.

The equilibrium $R_{\rm peak}$, due to fission cycling, appears as the straight region of the curve in Fig. 3.1 for $Y_e \lesssim 0.1$, and does not change significantly for variations in the wind conditions. This is depicted in Fig. 3.1 as the equilibrium peak ratio is not strongly affected by choice of the outflow timescale. Here, this stability is demonstrated for the wind outflow timescales of $\tau = 0.1$ s and $\tau = 0.3$ s.

The equilibrium value of $R_{\rm peak}$ is sensitive to properties of the fission model. In particular, it is sensitive to the specific location within the second peak to which fission returns material, as the presence of waiting points here dictate the flow and accumulation of material. Material deposited at or below closed-shell nuclei flow to a waiting point, and remain in this peak region longer than material deposited above the closed-shell nuclei. The accumulation of material in the $A \approx 130$ peak leads to smaller values of $R_{\rm peak}$. Material arriving above the closed-shell bypasses the waiting point and continues flowing to heavier regions, leading to larger values of $R_{\rm peak}$.

In Fig. 3.3 we show specific examples of the consequences to $R_{\rm peak}$ resulting from different fission daughter product distributions. We consider cases of fission daughter

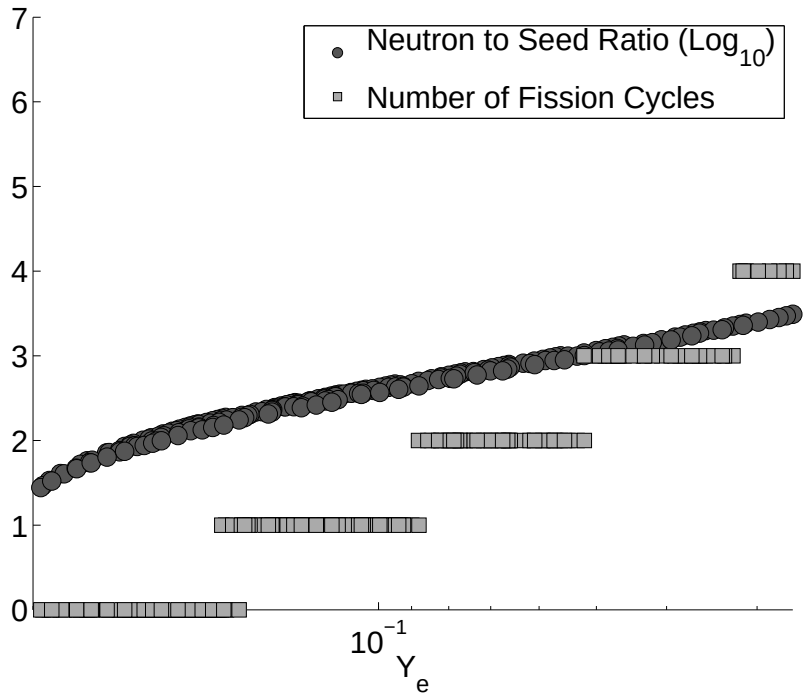


Figure 3.2: The correspondence between Y_e and both the number of fission cycles, Eqn. 3.7, and the neutron-to-seed ratio are shown for the conditions of Fig. 3.1 for our $\tau \approx 0.3$ s standard calculation. Each data point represents the outcome of an individual r-process calculation with different initial neutrino and antineutrino luminosities. The overlap in the number of fission cycles results from the influence of neutrinos on the abundance pattern as different sets of unique neutrino spectrum can result in similar electron fractions. Material begins to fission when $\gtrsim 200$ free neutrons are present for each seed nuclei.

product distributions with both symmetric and asymmetric modes. Symmetric distributions have daughter nuclides that are close in both charge, Z, and mass, A. These distributions deposit more material at or below the closed-shell nuclides and have a smaller equilibrium $R_{\rm peak}$, shown as circles in Fig. 3.3. Asymmetric distributions have daughter product distributions whose charge and mass are separated proportionally by a scaling factor, resulting in one daughter being larger in both A and Z than the other. This leads to more material being deposited above the closed-shell nuclides and a higher equilibrium $R_{\rm peak}$, shown as diamonds in Fig. 3.3. When neutrons are emitted during the course of fission, fewer daughter products lie above the close-shell nuclei, lowering the equilibrium $R_{\rm peak}$ from the asymmetric case, shown as squares

in Fig. 3.3. Detailed knowledge of both the fission location and daughter product distributions is required to fully model the r-process abundances in very neutron-rich environments.

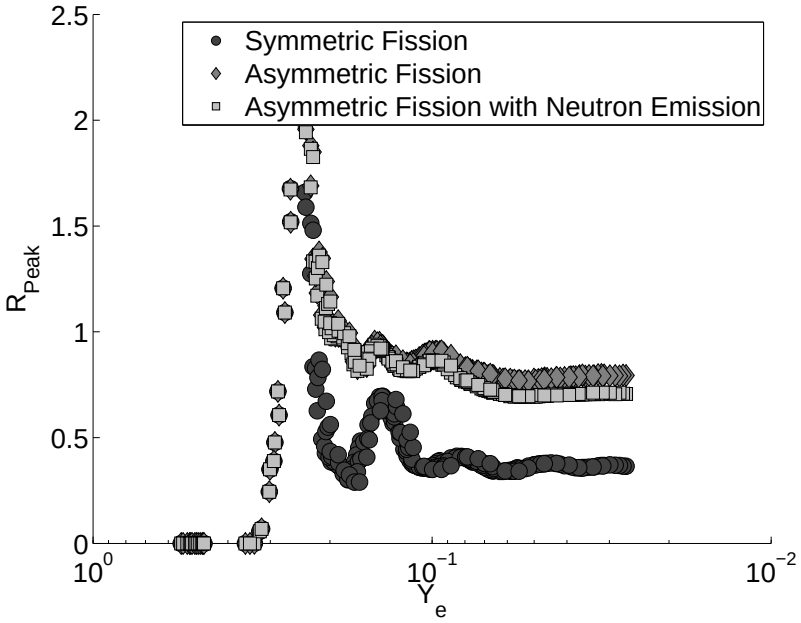


Figure 3.3: Same as Fig. 3.1, but compares the effects of different fission daughter product distributions. The distribution of daughter products determines if material is deposited above or below the closed-shell nuclei in the $A \approx 130$ peak. Fission distributions depositing material above the closed-shell nuclides, asymmetric fission (diamonds), leads to a higher equilibrium $R_{\rm peak}$, as more material is cycled through the $A \approx 130$ peak. Distributions depositing material below the peak, symmetric fission (circles), have a lower equilibrium $R_{\rm peak}$ and cycle less material through the peak region. Fission-induced neutron emission deposits additional material below the closed-shell nuclides, lowering $R_{\rm peak}$, and is shown above for asymmetric fission (squares).

The change in abundance of the various r-process peaks during fission cycling, as depicted in Fig. 3.1 and 3.3, can be phenomenologically described by the effective rate of material entering and exiting the major peak regions. The effect of fission cycling on the peak abundances is modeled by approximating the flow of fission material as rapid compared to the flow leaving the $A \approx 130$, the rare earth, and the $A \approx 195$

peak regions. The rate of abundance change in each peak becomes:

$$\dot{Y}_{130} = -\Gamma_{130}(t)Y_{130} + f\Gamma_{195}(t)Y_{195} \tag{3.8}$$

$$\dot{Y}_{\rm Earth} = -\Gamma_{\rm Earth}(t)Y_{\rm Earth} + \Gamma_{130}(t)Y_{130} + (2-f)\Gamma_{195}(t)Y_{195} \tag{3.9}$$

$$\dot{Y}_{195} = -\Gamma_{195}(t)Y_{195} + \Gamma_{\rm Earth}(t)Y_{\rm Earth} \tag{3.10}$$

where Y is the abundance of each peak and Γ is the rate of decay leaving a region, with the subscripts corresponding to the $A \approx 130$, rare earth, and $A \approx 195$ peaks. Here f is the distribution of fission daughter products between the $A \approx 130$ and rare earth regions. For purposes of illustrating the toy model, we take all fission products as arriving to the $A \approx 130$ region, $f = 2$. The equilibrium (steady β-flow) behavior of fission cycling is depicted in the far right-hand region of Fig. 3.1. For discussion of solutions for long-time fission cycling see [17]. The transient region prior to steady β-flow equilibrium is dependent on the flow (decay rate) of material leaving each peak region, Γ_{130}, $\Gamma_{\rm Earth}$, and Γ_{195}. The effective flow out of a region is determined by the β-decay rate of each isotopic chain, as material is in $(n,\gamma) \leftrightharpoons (\gamma,n)$ equilibrium during this fission cycling phase. Additionally, this outflow is determined by the population of nuclides within a peak, since the individual β-decay rate changes from nuclide to nuclide. As a consequence, various nuclides are populated while material is flowing through each peak, leading to changes in the effective flow out of each peak. For example, the effective flow rate in the $A \approx 130$ peak slows as the closed shell nuclides, with slow β-decay rates, are populated. We employ our phenomenological model to highlight the change in the effective flow rate in Fig. 3.4, for the $A \approx 130$ peak region with a $Y_e = 0.05$ at the start of the r-process. Here, the fluctuation in the decay rates of a peak corresponds to the changing of individual nuclide abundances. The movement of material within a peak is demonstrated by the corresponding change of the weighted atomic number, Z. As the conditions in Fig. 3.4 are very neutron-rich, sufficient for steady β-flow, the right-most portion depicts a straight line for both the effective flow rate and Z, since steady β-flow leads to isotopic chain abundances determined by the β-decay rate of each chain.

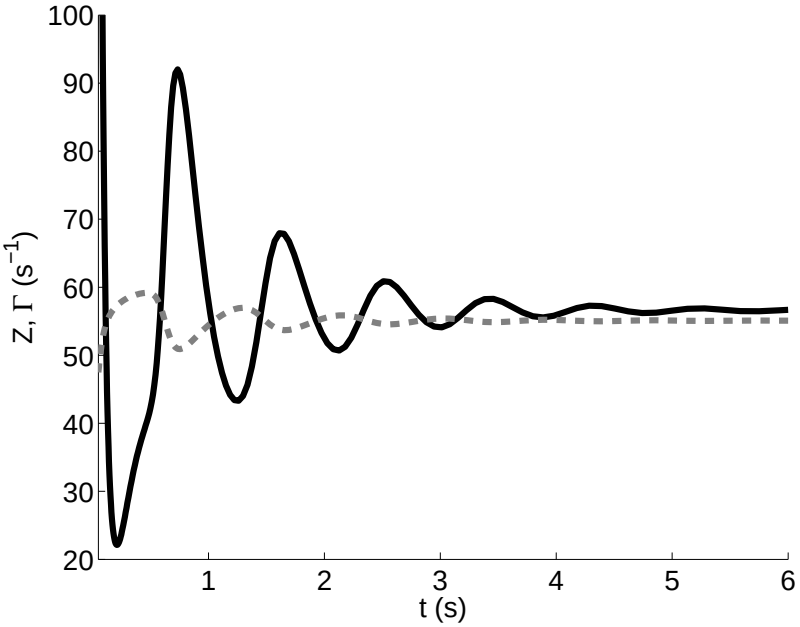


Figure 3.4: Under very neutron-rich conditions the effective decay rate of the peaks oscillate until equilibrating at the steady β-flow rate. The abundance weighted atomic number, $Z = \sum_{Z=45}^{60} Z\ Y(Z) / \sum_{Z=45}^{60} Y(Z)$, (dashes) is plotted with the abundance weighted β-decay rate, $\Gamma = \sum_{Z=45}^{60} \Gamma_\beta(Z)\ Y(Z) / \sum_{Z=45}^{60} Y(Z)$, of an isotopic chain (solid) for the second, $A \approx 130$, peak region, versus time, t. The oscillation of the decay rates in the peak regions are due to the changing population of different nuclides during the course of fission cycling. To elucidate abundance changes between isotopic chains, the data above results from our phenomenological model, Eqn. 3.8, under conditions with an $Y_e = 0.05$ at the start of the r-process epoch ($T_9 \approx 2.5$).

3.4 Steady Beta Flow

As discussed in Sec. 3.1, the abundances of the r-process become fully determined under conditions where both fission cycling and steady β-flow occur. We now examine consequences to the final r-process abundances resulting from steady β-flow. In Fig. 3.5, the steady-β flow condition, Eqn. 3.5, is tested and fulfilled for very neutron-rich conditions in the neutrino-driven wind, appearing as a straight line between the second and third peaks of the r-process, the main r-process region. For less neutron-

rich conditions, steady-β flow does not obtain as there are not enough free neutrons to sustain re-population of the seed nuclei by fission cycling.

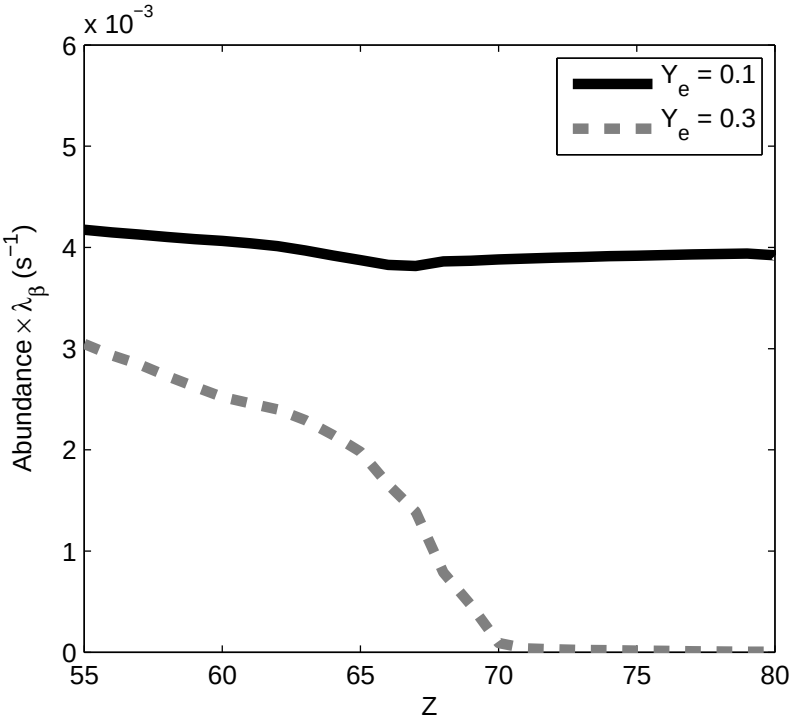


Figure 3.5: We plot the steady β-flow condition, $\sum_A Y(Z,A)\lambda_\beta(Z,A)$, versus atomic number, Z, for two different Y_e's in the neutrino-driven wind. For the case with an $Y_e = 0.1$ at the start of the r-process epoch, conditions are sufficiently neutron-rich for steady β-flow, marked by a straight line. The case with $Y_e = 0.3$ is not neutron-rich enough for steady β-flow to obtain.

A set of typical abundances resulting from steady-β flow, occurring for very neutron-rich conditions in the neutrino-driven wind, are depicted in Fig. 3.6. The individual Y_e's are produced by a unique choice of initial neutrino and anti-neutrino luminosities, in the same manner as Fig. 3.1. Our abundance patterns reproduce the general peak structure of the main r-process between the second and third peaks and is robust over a wide range of conditions in the neutrino-driven wind, directly resulting from the pairing of both fission cycling and steady β-flow. Improvement to a nuclide by nuclide abundance comparison between calculation and both solar and halo star abundance data requires further understanding of the nuclear properties

of nuclei far from stability and processes that influence the abundance pattern after freeze-out [118, 119, 120].

Abundance yields resulting from the joint operation of both fission cycling and steady beta flow produce a consistent pattern of r-process abundances that extends to elements in the actinide region. The main r-process does not appear to extend past $Z > 82$, however. It is possible that the abundance of elements in the actinide region relative to those between the second and third r-process region can be influenced by mechanisms external to the formation of the r-process by both fission cycling and steady beta flow, allowing the final abundances of these elements to emerge independently from the consistent pattern of r-process elements between the second and third peak region. These mechanisms may include post-freeze-out neutrino-induced fission [120] and contributions from an r-process that only yields elements near the actinide region [121]. Additional discussion on the abundance of the r-process elements in the actinide region may be found in Goriely and Arnould 2001 [121].

It has previously been shown, *e*.g. Otsuki et al. 2003 [122], that consistent patterns of r-process elements form in the rare earth region, between $60 \lesssim Z \lesssim 70$, due to the absence of waiting point nuclei in this region. Under particular wind conditions, $\tau = 0.005$ s for example, the resulting r-process abundance pattern can reproduce the full, observed region of consistent r-process elements, $56 \lesssim Z < 76$ [95], as found in the halo star data. In contrast, our calculations demonstrate that when steady β-flow is jointly accompanied by fission cycling, the region of universality is not dependent on the wind conditions and extends between the fission daughter products and the fission termination point of the r-process.

3.5 Influence of Neutrinos on the Electron Fraction

After neutrinos extricate material from the surface of the proto-neutron star, the newly released material is composed entirely of free nucleons. Although we dynamically calculate the Y_e in our models, it is pedagogically useful to examine the electron

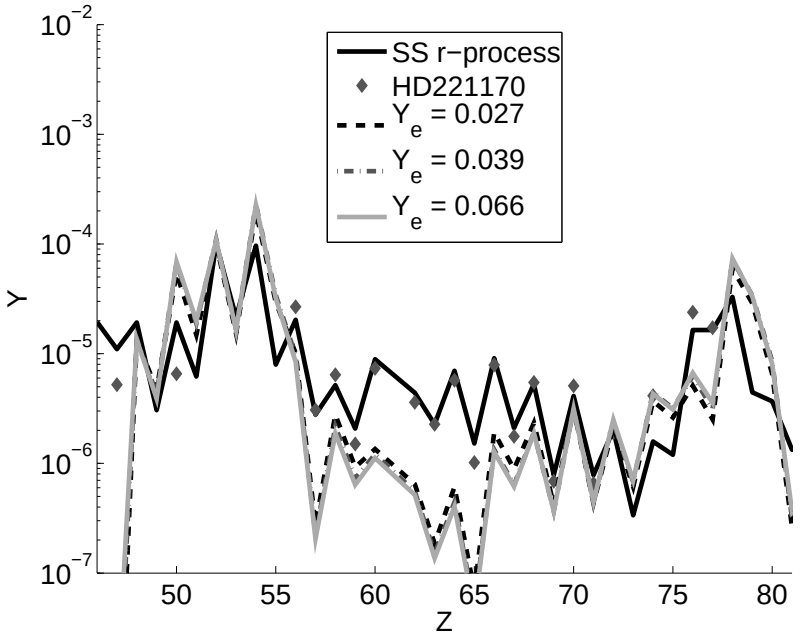


Figure 3.6: When conditions neutron-rich enough for steady β-flow occur, a consistent r-process pattern emerges regardless of the initial Y_e. The details of the abundance pattern are dependent on the nuclear physics employed in the mass model, as discussed in the text. The abundance, Y, is plotted versus the atomic number, Z, for these very neutron-rich conditions. The dashed line is generated in the neutrino-driven wind for $L_{\nu_e} = 0.02$ and $L_{\overline{\nu}_e} = 3.0$, the dashed-dotted line for $L_{\nu_e} = 0.01$ and $L_{\overline{\nu}_e} = 4.0$, and the solid line for $L_{\nu_e} = 0.006$ and $L_{\overline{\nu}_e} = 6.0$. The electron neutrino and anti-neutrino luminosities, L_{ν_e} and $L_{\overline{\nu}_e}$, are in units of $\times 10^{51}$ ergs s^{-1}. The effective temperature of the electron neutrinos is $T_{\nu_e} = 3.5$ MeV and for the electron anti-neutrinos is $T_{\overline{\nu}_e} = 4.5$ MeV. Labeled is Y_e at the start of the r-process epoch. The black line represents the solar system abundances from [6], and the gray diamonds are the r-process abundances from the halo star HD 221170 [7]. All abundances are scaled to 10^{-4} at $Z = 52$.

fraction through the approximation of weak equilibrium. Since neutrino and anti-neutrino rates dominate electron and positron capture, the initial weak equilibrium $Y_e^{(0)}$ is

$$Y_e^{(0)} \approx \frac{1}{1 + \lambda_{\bar{\nu}_e}/\lambda_{\nu_e}}. \tag{3.11}$$

The rates of electron neutrino capture on neutrons and electron anti-neutrino capture on protons are λ_{ν_e} and $\lambda_{\overline{\nu}_e}$ respectively. An increase in the electron anti-neutrino capture rate, achievable by either boosting the electron anti-neutrino flux

or hardening the electron anti-neutrino spectra, will tend to decrease Ye, while an increase in the neutrino capture rate will tend to increase Ye.

Farther away from the proto-neutron star, as material in the expansion continues to cool, α-particles form and contribute to the weak equilibrium Y_e approximation,

$$Y_e \approx Y_e^{(0)} + \left(\frac{1}{2} - Y_e^{(0)}\right) X_\alpha. \tag{3.12}$$

Here, X_α represents the mass fraction of α-particles.

The formation of α-particles is enhanced in the presence of a strong electron neutrino flux, as electron neutrinos capturing on free neutrons create new effective proton seeds for α-particle formation. These effective seeds quickly capture additional neutrons which continues to drive the Y_e to 1/2. The depletion of neutrons from both neutrino capture and α-particle formation is known as the alpha effect, and this alpha effect must be removed for neutron-rich conditions to obtain for the r-process.

We look to neutrino luminosities and spectral properties for the removal of the alpha effect. Since weak equilibrium does not fully obtain in the neutrino-driven wind, we use the following procedure to calculate Y_e instead of the weak equilibrium approximation described above. Starting from a prospective set of neutrino effective temperatures and luminosities, we adjust the initial Fermi-Dirac neutrino spectrum. Then we self-consistently account for both the evolution of the updated neutrino spectrum in the neutrino-driven wind and the relevant changes to the abundance. From this, we dynamically account for the Y_e throughout the nucleosynthesis epochs. For a full description see [106].

We first examine Y_e's resulting from a range of neutrino effective temperatures. Before the formation of α-particles, $T_9 \approx 9.4$, the Y_e's from our model are consistent with weak equilibrium. The Y_e increases with larger electron neutrino effective temperatures as these higher temperatures result in more protons being converted to neutrons. This results from electron neutrino capture on neutrons, Eqn. 3.1. Conversely, larger anti-neutrino energies produce a lower Y_e, a consequence of electron anti-neutrino capture, Eqn. 3.2. The ranges of neutrino effective temperatures depicted in the top panel of Fig. 3.7 result in Y_e between $0.1 \lesssim Y_e \lesssim 0.6$, and the low Y_e portion of the region seems initially promising for a successful r-process. In

Fig. 3.7, the luminosity of the electron neutrinos is 1×10^{51} ergs s^{-1} and the electron anti-neutrino luminosity is 1.3×10^{51} ergs s^{-1}.

After α-particle formation and charged particle reactions have occurred, conditions generated by changes to the neutrino effective temperatures do not lead to a successful r-process. The Y_e at the r-process epoch is shown in the bottom panel of Fig. 3.7, and is noticeably compressed by the alpha effect, ranging between $0.4 \lesssim Y_e \lesssim 0.5$. The Y_e is increased compared to the previous epoch as the alpha effect has converted free neutrons into additional effective proton seed nuclei. These values of Y_e are not neutron-rich enough to lead to a successful r-process.

The second case we examine is for changes in the neutrino and anti-neutrino luminosities. Although initially similar, they lead to a decidedly different outcome, as environments where sufficient reductions in the electron neutrino luminosity occur can lead to a successful r-process. When both the neutrino and anti-neutrino luminosities are significantly reduced compared to traditional models, electron capture and positron capture become important and influence the electron fraction,

$$Y_e \approx 1/[1 + (\lambda_{\bar{\nu}_e} + \lambda_{e^-})/(\lambda_{\nu_e} + \lambda_{e^+})], \tag{3.13}$$

where λ_{e^-} and λ_{e^+} are the electron and positron rates respectively [59]. When electron-positron pairs are important, as they are here, these rates tend to increase the Y_e and begin influencing the Y_e when the neutrino luminosities are $L_{\nu_e} \lesssim 10^{50}$ ergs s^{-1} and $L_{\overline{\nu}_e} \lesssim 5 \times 10^{50}$ ergs s^{-1}. For wind solutions where neutrinos are less prevalent, a weak equilibrium Y_e dictated by electron and positron capture would not be sufficiently neutron-rich for the r-process.

For reductions in the electron neutrino luminosity relative to the traditional wind model, but not in the electron anti-neutrino luminosity, a very large variety of Y_e's result, $0.1 \lesssim Y_e \lesssim 0.8$, as shown in the top panel of Fig. 3.8. Similar to the case with effective neutrino temperatures, lowering the electron neutrino luminosities, L_{ν_e}, decreases the Y_e and leads to neutron-rich conditions. These early Y_e's from the changed rates in Eqn. 3.1 and Eqn. 3.2 are again consistent with the weak equilibrium values. For all of Fig. 3.8, we take the effective electron neutrino temperature to be $T_{\nu_e} = 3.5$ MeV and the electron anti-neutrino temperature as $T_{\overline{\nu}_e} = 4.5$ MeV.

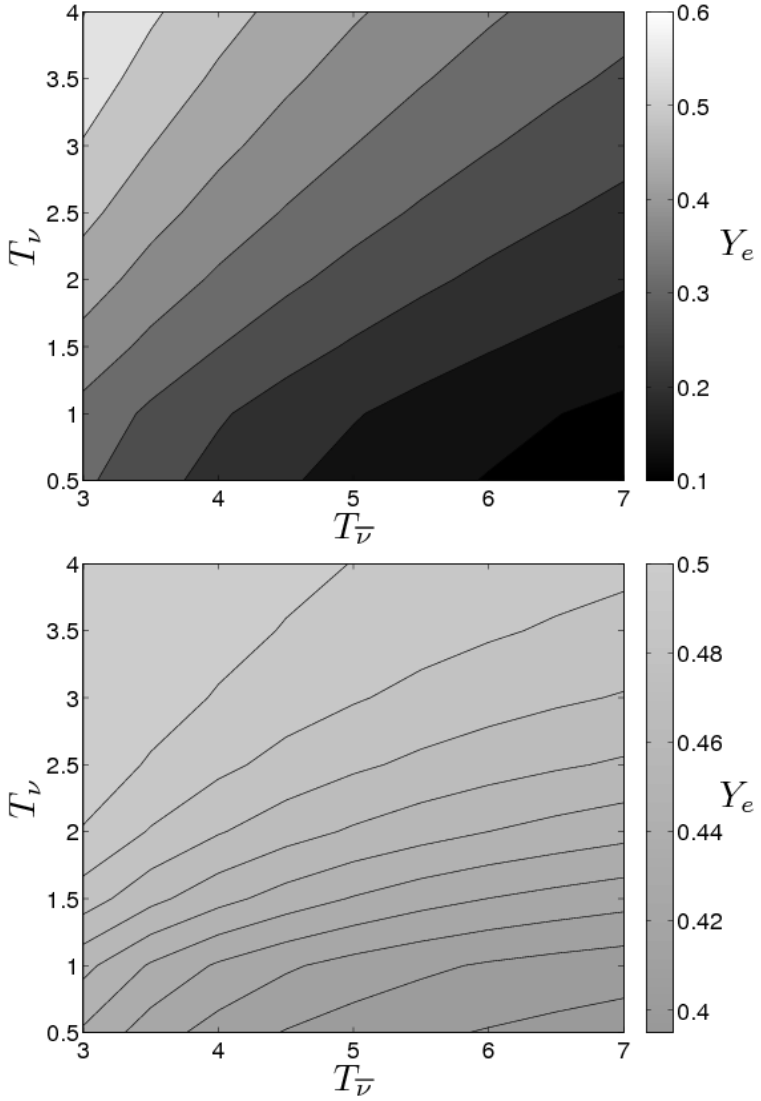


Figure 3.7: The electron fraction, Y_e, is shown over a range of electron neutrino and anti-neutrino temperatures, T_ν and $T_{\overline{\nu}}$. The "alpha" effect equally binds protons and neutrons into α-particles which drives the electron fraction to $Y_e \approx 1/2$ and prevents an r-process. Regions of Y_e before α-particle formation ($T_9 \approx 9.4$), top panel, initially appear favorable to the r-process; however, the "alpha" effect has pushed Y_e near $1/2$ by the start of the r-process epoch ($T_9 \approx 2.5$), bottom panel. The effective electron neutrino and anti-neutrino temperatures, T_ν and $T_{\overline{\nu}}$, are in units of MeV. The electron neutrino luminosity is $L_\nu = 1 \times 10^{51}$ ergs s^{-1} and the electron anti-neutrino luminosity is $L_{\overline{\nu}} = 1.3 \times 10^{51}$ ergs s^{-1}.

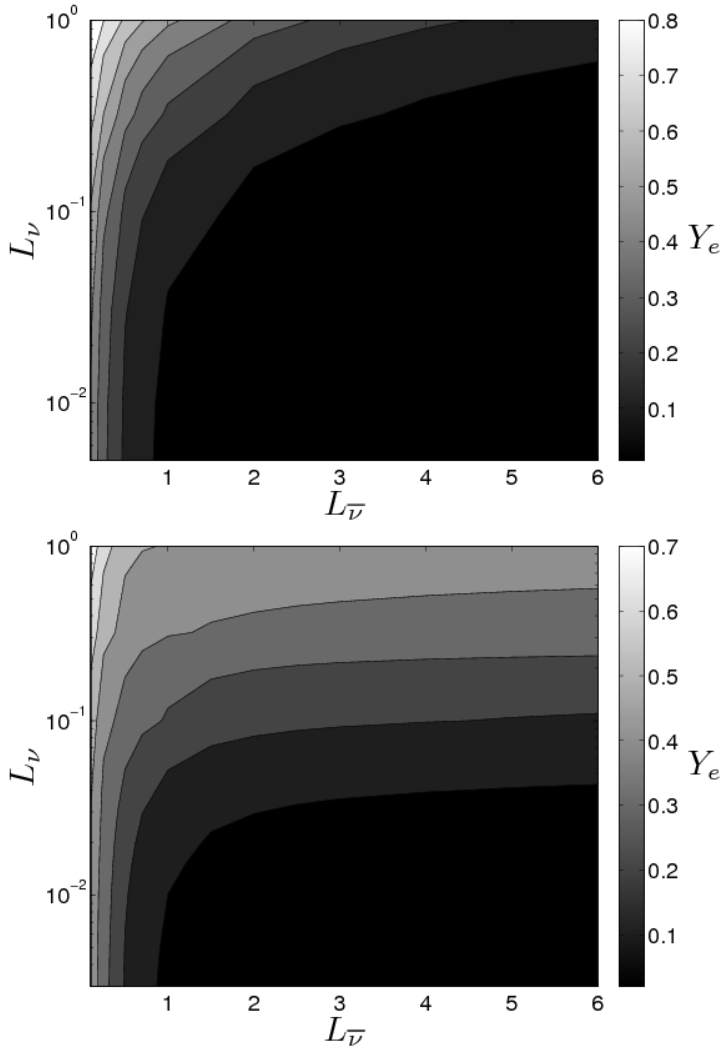


Figure 3.8: The electron fraction, Y_e, is shown over a range of electron neutrino and anti-neutrino luminosities, L_ν and $L_{\overline{\nu}}$. A reduction in the electron neutrino luminosity, L_ν, prevents the "alpha" effect and leads to a successful r-process. The "alpha" effect is avoided as reducing the electron neutrino luminosity, L_ν, lowers the rate of neutrino capture on neutrons forming protons, Eqn. 3.1. The electron fraction, Y_e, is favorable for the r-process before α-particle formation ($T_9 \approx 9.4$), top panel, and reductions in L_ν lead to a low Y_e conditions for the r-process, bottom panel. The electron neutrino and anti-neutrino luminosities, L_ν and $L_{\overline{\nu}}$, are in units of $\times 10^{51}$ ergs s^{-1}. The effective temperature of the electron neutrinos is $T_\nu = 3.5$ MeV and for the electron anti-neutrinos is $T_{\overline{\nu}} = 4.5$ MeV. For low values of both L_ν and $L_{\overline{\nu}}$, electron and positron capture set the Y_e.

Near the r-process epoch, $T_9 \approx 2.5$, changes to the neutrino luminosities continue to produce a large spread of Y_e's, as depicted in the bottom panel of Fig. 3.8. A successful r-process can occur for reductions to the electron neutrino luminosity of $L_{\nu_e} \lesssim 2.3 \times 10^{50}$ ergs s^{-1}. For these decreased electron neutrino luminosities, the depletion of free neutrons by the alpha effect is diminished as fewer new protons are made available through Eqn. 3.1. The neutrino luminosities that lead to a successful r-process are shown by all three shaded regions in Fig. 3.9.

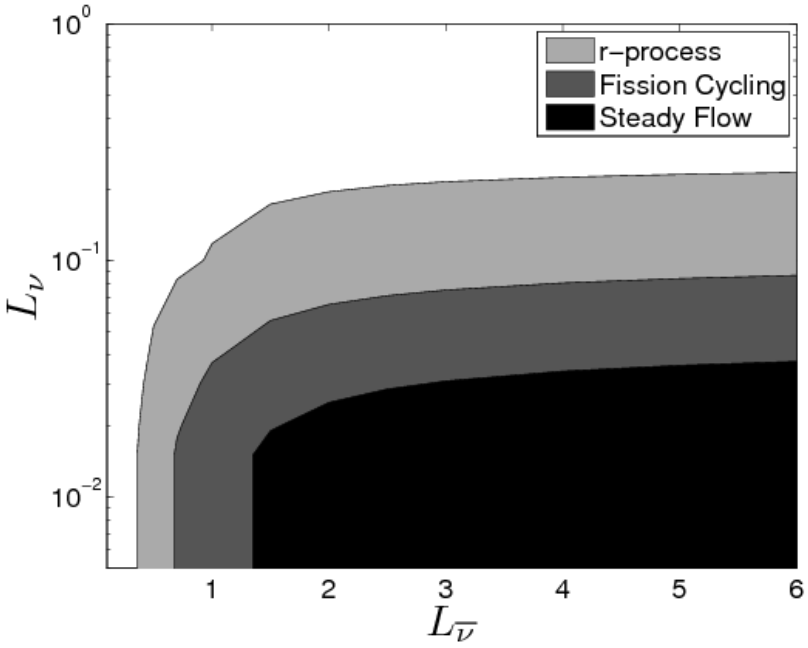


Figure 3.9: Under the wind conditions of Fig. 3.8, neutrino luminosities, L_ν and $L_{\overline{\nu}}$ in units of $\times 10^{51}$ ergs s^{-1}, necessary for a successful r-process (all shaded regions), the presence of fission cycling (medium gray and black), and for the presence of steady β-flow (black) are shown.

We note that neutron-rich conditions beyond the minimum required to produce an r-process occur in our study of the neutrino luminosities. In fact, order of magnitude reductions of L_{ν_e} lead to conditions where fission cycling can occur in the r-process. For a $\tau = 0.3$ s wind timescale, $Y_e \lesssim 0.17$ are sufficient to lead to fission cycling, depicted in the medium gray and black regions of Fig. 3.9. Conditions even more neutron-rich, $Y_e \lesssim 0.1$, lead to a steady flow solution within fission cycling, as described in Sec. 3.4, reproducing the general features of the halo star data and

providing an intriguing solution for the realization of a main r-process. This scenario is shown in Fig. 3.9 as the black region. The necessary large reductions to the L_{ν_e} could be a consequence of either active-sterile neutrino oscillations [106] or other new physics.

3.6 Conclusions

In the neutrino-driven wind, fission cycling during r-process nucleosynthesis occurs for low electron fractions, and when combined with steady β-flow, reproduces the basic features of the main r-process. During fission cycling, material effectively captures out of the third peak and returns to the second peak by fission processes, linking the second and third peaks, and creating a main r-process. For $0.1 \lesssim Y_e \lesssim 0.3$, these abundance patterns retain some dependence on the initial Y_e.

At even lower electron fractions, $Y_e \lesssim 0.1$, steady-β flow occurs during the r-process and the abundance patterns produced are consistent over small changes to the astrophysical conditions. Steady-β flow is a consequence of the presence of both fission cycling and $(n,\gamma) \leftrightharpoons (\gamma,n)$ equilibrium. Fission cycling creates seed nuclei at the second peak, and $(n,\gamma) \leftrightharpoons (\gamma,n)$ equilibrium determines the r-process path. After $(n,\gamma) \leftrightharpoons (\gamma,n)$ equilibrium fixes the path, β-decay between the isotopic chains equilibrate as the first and last chains are connected by fission. This produces an abundance pattern which is not sensitive to the exact initial Y_e. The steady-β flow abundances strongly depend on the details of fission.

As the final r-process abundance pattern is very sensitive to the details of fission, see Fig. 3.3, it is paramount to improve our understanding of which heavy nuclides participate in fission during the r-process and to develop a more precise determination of the daughter products that result. The presence of fission in the r-process may provide a termination point for the r-process, furthering the understanding of which heavy nuclides play a role in the r-process. Under neutron-rich conditions, the distribution of fission daughter products influences the shape of the r-process. If the r-process occurs in very neutron-rich environments, the fission daughter product distribution also determines the starting isotopic chain of steady-β flow, impacting

the region where steady-β flow abundances form and may be important to the understanding of the formation of a main r-process.

Low Y_e's at the r-process epoch are not found in the traditional neutrino-driven wind. Before the onset of alpha particle formation, a large range of electron neutrino and anti-neutrino effective temperatures and luminosities would yield low Y_e environments. The electron fraction is driven to $Y_e \approx 1/2$ as alpha particle formation binds protons and neutrons in equal numbers. Changes to the effective temperatures in the ranges of 0.5 MeV $< T_\nu <$ 4 MeV for electron neutrinos and 3 MeV $< T_{\overline{\nu}} <$ 7 MeV for electron anti-neutrinos result in environments with an "alpha" effect and do not yield a main r-process. Given the physics discussed in this paper, realization of the main r-process in a conventional neutrino-driven wind is a challenge. However, it can occur with a reduction in the electron neutrino capture rate while the electron anti-neutrino capture rate remains unchanged. Future studies on the details of neutrinos, particularly in the post-core bounce supernova environment, as well as physics beyond the standard model, would benefit the understanding of an r-process in the neutrino-driven wind.

Chapter 4

The Role of the ^{130}Sn (n,γ) Rate in the r-process

We examine how the neutron capture cross section of ^{130}Sn is pivotal in shaping the global r-process abundance pattern generated in the neutrino-driven wind of the core-collapse supernova environment. The effects to the r-process of increasing the neutron capture cross section of ^{130}Sn include not only a relative decrease in the abundance of ^{130}Sn and an increase in the abundance of ^{131}Sn, but also a shift in the distribution of material in the rare earth and third peak regions towards nuclei lighter in A . Reducing the uncertainties in this critical cross section, perhaps through experimental exploration at a rare isotope facility, will further enable a detailed comparison between r-process models and both the solar system and halo star data, improving the understanding of the nature of the r-process environment.

4.1 Background

The goal of a number of recent r-process studies is to examine the various candidate r-process locations, prospecting for suitable conditions for the r-process. The merit of a location is evaluated by how well the calculated r-process abundances reproduce the abundance features found in the available solar and halo star data. Difficulties in comparison arise as models of the r-process lack the relevant nuclear

data for many of the large number of participating nuclei ($\gtrsim 3000$), as few r-process nuclei have been examined experimentally, see *e.*g. Pearson et al. 2006 [52].

In the r-process, both neutron capture and photo-disintegration are initially much faster than the competing β-decay, hence $(n,\gamma) \rightleftharpoons (\gamma,n)$ equilibrium obtains, and the relative abundances of adjacent nuclei are described by detailed balance [10],

$$\begin{aligned} \frac{Y(Z,A+1)}{Y(Z,A)} &= \frac{n_n \langle v\sigma_{n,\gamma}(Z,A)\rangle}{\lambda_{\gamma,n}(Z,A+1)} \\ &= n_n \left(\frac{2\pi\hbar^2}{m_u kT}\right)^{3/2} \left(\frac{A+1}{A}\right)^{3/2} \times \\ &\quad \frac{G(Z,A+1)}{2G(Z,A)} \exp\left[\frac{S_n(Z,A+1)}{kT}\right] \end{aligned} \tag{4.1}$$

Here $\hbar$ is the Planck constant, k is the Boltzmann constant, m_u is the atomic mass unit, n_n is the neutron number density, $\langle v\sigma_{n,\gamma}(Z,A)\rangle$ is the product of the capture cross section and the neutron velocity averaged over a thermal distribution of temperature T, $\lambda_{\gamma,n}(Z,A)$ is the rate of photo-disintegration, $G(Z,A)$ is the nuclear partition function, and $S_n(Z,A)$ is the neutron separation energy. For a given isotopic chain in which the S_n's decrease monotonically versus increasing atomic weight, A, the neutron separation energy of the most abundant nuclide in the chain is,

$$S_n \approx kT \ln\left[\frac{2}{n_n}\left(\frac{m_u kT}{2\pi\hbar^2}\right)^{3/2}\right] \tag{4.2}$$

Once S_n is known, the individual abundances of the nuclei along an isotopic chain can be determined. If the r-process is taken to operate entirely under the approximation of $(n,\gamma) \rightleftharpoons (\gamma,n)$ equilibrium, then, besides the S_n's, only the rates of β-decay between isotopic chains are necessary to determine the final r-process abundance pattern.

$(n,\gamma) \rightleftharpoons (\gamma,n)$ equilibrium no longer obtains at late times in the r-process when the neutron-to-seed ratio of the r-process falls below one, $R \lesssim 1$. Individual neutron capture and photo-disintegration reactions are now important in determining the final r-process abundance pattern. Calculations of the r-process employ primarily phenomenological models of neutron capture cross sections that use theoretical nuclear mass models as inputs. The neutron capture cross section of a single nucleus can vary by several orders of magnitude between individual theoretical models. The

variation in the neutron capture cross sections across the chart of the nuclei is demonstrated in Fig. 4.1 for three sets of theoretical neutron capture cross sections based on the SMOKER model [10], the FRDM model [76], and the ETFSI model [123].

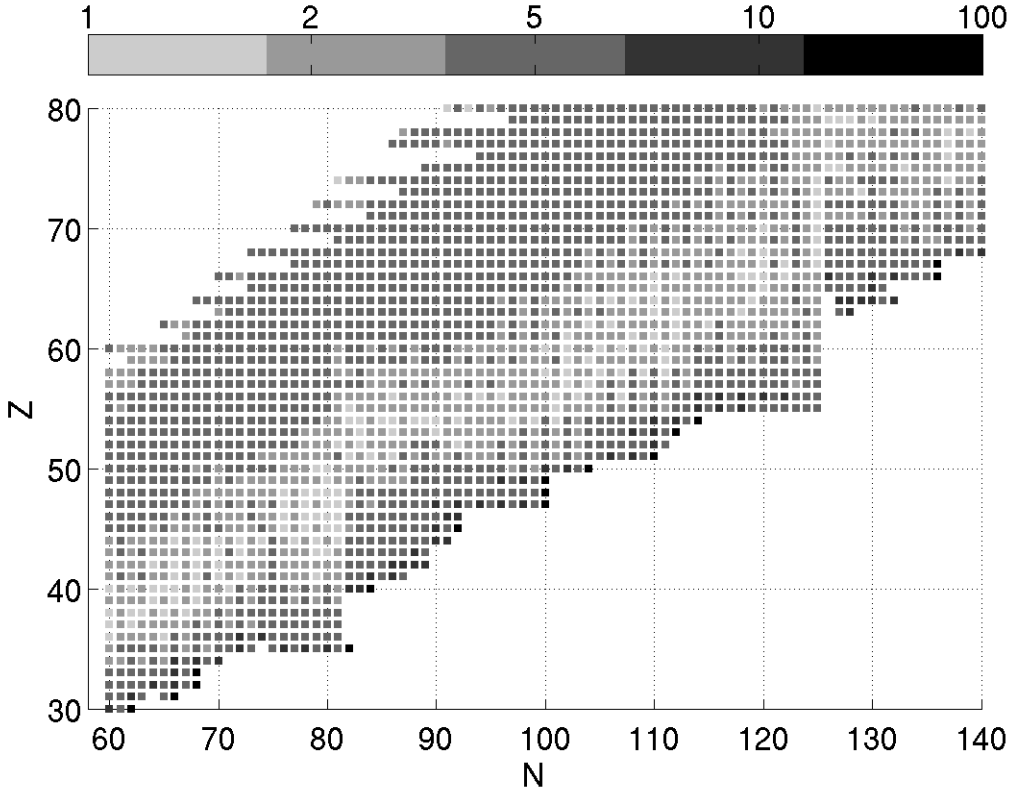


Figure 4.1: We show the ratio (logarithmic) of the largest neutron capture cross section with respect to the smallest neutron capture cross section over the chart of the nuclei between the three sets of theoretical neutron capture cross sections listed in the text. The neutron capture cross sections can vary by many orders of magnitude (ratios of over 10^{10} for the darkest squares) between the theoretical models.

It was noted previously, *e.g.* Surman and Engel 2001 [124], that individual neutron capture cross sections in the region of $A \sim 195$ can influence the r-process in this same region at late times. We explore how an increase to the neutron capture cross section of ^{130}Sn by a factor of 100 yields global changes to the abundance pattern of the r-process compared to an r-process calculation under the original, unaltered neutron capture cross sections. The Holifield Radioactive Ion Beam Facility

(HRIBF) at Oak Ridge National Laboratory (ORNL) is capable of acquiring the relevant nuclear data necessary to generate precision neutron capture cross sections for neutron-rich nuclei near the $N = 82$ closed shell and experiments are in progress to collect this data for ^{130}Sn for the first time [125].

4.2 Model of r-process Nucleosynthesis

To examine the effects of individual neutron capture cross sections at late times in the r-process, we track the chemical evolution of a mass element in the neutrino-driven wind environment, post-ejection, from the protoneutron star's surface. We choose conditions in the neutrino driven wind that to lead to the production of r-process elements through the third r-process peak. We employ a 1D thermodynamic model of the neutrino driven wind with wind parameters of $\tau = 0.3$ s, $S/k = 100$, and an electron fraction at the start of the charged particle epoch of $Y_e = 0.26$ at $T_9 = 10$. In this initial study, as the changes to the r-process pattern occur late in the nucleosynthesis epoch, we do not include neutrino interactions. This study employs an updated set of theoretical β-decay lifetimes found in Möller et al. 2003 [126], and additional details of the nuclear data and of our computational model of the r-process have been discussed previously in Chapters 1 and 2.

4.3 ^{130}Sn as a Secondary Waiting Point

The r-process path is well described by the $(n, \gamma) \leftrightarrows (\gamma, n)$ equilibrium approximation while neutron rich conditions persist in the r-process, and the location of the path is set, in part, by the local thermodynamic conditions, including ρ and T_9. Material advancing along the r-process path accumulates at nuclei with long β-decay lifetimes that are known as waiting points. In addition to these classical waiting points, we suggest that a set of minor, or secondary waiting points may also occur in the r-process. Secondary waiting point nuclei can play a critical role in shaping the outcome of the r-process. We classify a nucleus as a secondary waiting point when the following two conditions are met: a large amount of r-process material flows to

the nucleus before the supply of free neutrons is exhausted, and the rate of β-decay of the nucleus is slow compared to the timescale of the r-process.

A secondary waiting point of consequence to the r-process, ^{130}Sn, emerges prior to freeze-out, while the free neutron abundance is rapidly falling but neutron capture continues to be a relevant reaction in the r-process. ^{130}Sn functions as a secondary waiting point in the r-process due to the location of the r-process path at late times. The r-process path near ^{130}Sn includes three highly populated nuclei, ^{130}Cd, ^{130}In, and ^{132}Sn, at the time ^{130}Sn becomes populated, $t \approx 3.5$ s. ^{130}Cd and ^{130}In have β-decay lifetimes much shorter than ^{132}Sn and depopulate at a faster rate. These three nuclei are shown in Fig. 4.2.

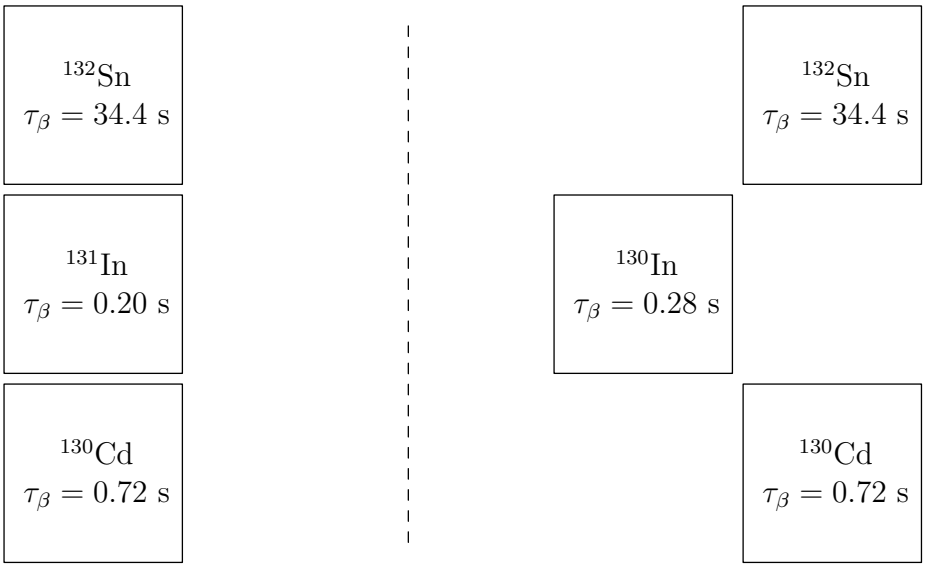


Figure 4.2: In the right hand frame, we show an example of the most populated nuclei near ^{130}Sn at the time it becomes populated in an r-process in the neutrino-driven wind, $t \approx 3.5$ s. These r-process nuclei include ^{130}Cd, ^{130}In, and ^{132}Sn. In the left hand frame, the classical waiting point nuclei along $N = 82$ are shown. We employ the following wind parameters for the neutrino-driven wind: an expansion timescale of $\tau = 0.3$ s and an entropy per baryon of $S/k = 100$.

A large amount of material flows along the $A = 130$ β-decay reaction channel from ^{130}Cd and ^{130}In as both nuclei have a large abundance and short β-decay lifetimes. The β-decay of ^{130}In feeds into ^{130}Sn at this critical time in the r-process, and ^{130}Sn

becomes heavily populated as a result. The β-decay pathways that feed into ^{130}Sn are shown in Fig. 4.3.

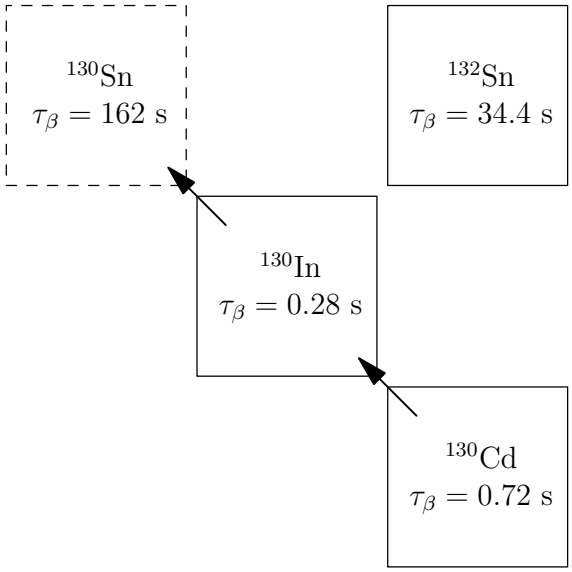


Figure 4.3: The flow of material along the β-decay reaction channel of the $A = 130$ path nuclei is shown above. The arrows indicate the direction of β-decay. ^{130}Sn is heavily populated by material that arrives from the β-decay pathway of ^{130}Cd and ^{130}In. The figure is shown for the same conditions as Fig. 4.2.

The fraction of material that the now highly populated ^{130}Sn directs along the $Z = 50$ nuclei by neutron capture is sensitive to the neutron capture cross section of ^{130}Sn. The long β-decay lifetime of ^{130}Sn, $\tau_\beta = 162$ s, leads to relatively small amounts of material flowing from ^{130}Sn by β-decay. The r-process is sensitive to the neutron capture cross section of ^{130}Sn since this nucleus has such a large abundance at this critical time in the r-process, and the large outflow of ^{130}Sn is predominantly directed along its neutron capture channel. We demonstrate the flow of material into ^{130}Sn by β-decay along with its primary outflow channel of neutron capture in Fig. 4.4.

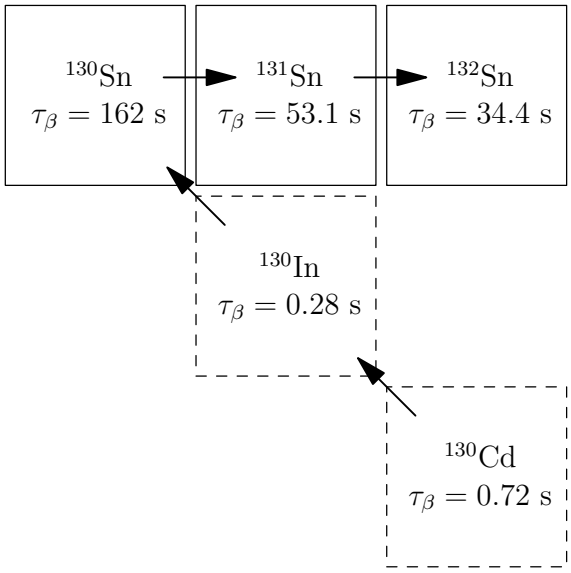


Figure 4.4: The flow of material near ^{130}Sn is shown above. The arrows that point towards the right indicate the direction of the neutron capture reaction channel, and the arrows that point along the diagonal indicate the direction of β-decay. A large amount of material arrives at ^{130}Sn from the β-decay of the $A = 130$ nuclei. Depending on the neutron capture cross section of ^{130}Sn, some fraction of this material is re-directed along the $Z = 50$ neutron capture reaction channel. The conditions here are the same as Fig. 4.2.

4.4 Impact of ^{130}Sn (n, γ) on the r-process

We examine how the uncertainties in the neutron capture cross section of a single nucleus, ^{130}Sn, impact the evolution of the r-process in the neutrino-driven wind. Our procedure is as follows: we calculate an r-process in the neutrino-driven wind as described in Sec. 4.2. This calculation is our baseline calculation. To explore the uncertainties in the neutron capture cross section of ^{130}Sn, we then introduce a scaling factor, χ, into our calculation, which modifies the ^{130}Sn neutron capture cross section,

$$\langle v\sigma_{n,\gamma}(^{130}\mathrm{Sn})\rangle' = \chi\langle v\sigma_{n,\gamma}(^{130}\mathrm{Sn})\rangle \tag{4.3}$$

Above, $\langle v\sigma_{n,\gamma}(^{130}\mathrm{Sn})\rangle$ is the original, thermally averaged, neutron capture cross section of ^{130}Sn, $\langle v\sigma_{n,\gamma}(^{130}\mathrm{Sn})\rangle'$ is the modified neutron capture cross section of ^{130}Sn, and χ is a scalar multiplication factor. Changes to the neutron capture cross section

of ^{130}Sn induce a reciprocal change in the photo-dissociation rate, λ_γ, of ^{131}Sn,

$$\lambda'_\gamma(^{131}\text{Sn}) = \chi\lambda_\gamma(^{131}\text{Sn}) \tag{4.4}$$

Above, $\lambda_\gamma(^{131}\text{Sn})$ is the original photo-dissociation rate of ^{131}Sn and $\lambda'_\gamma(^{131}\text{Sn})$ is the modified photo-dissociation rate of ^{131}Sn. In this study we examine a specific case where the neutron capture cross section of ^{130}Sn is multiplied by a factor of 100, and the photo-dissociation rate of ^{131}Sn is also increased by a factor of 100 ($\chi = 100$).

We find that increasing the neutron capture cross section of ^{130}Sn by a factor of 100 not only influences the abundance of r-process nuclei near ^{130}Sn but also introduces global changes to the abundance of nuclei throughout the r-process pattern. Changes to the abundance near ^{130}Sn include a decrease in the abundance of the $A = 130$ nuclei by $\sim 90\%$ and an increase in the abundance of the $A = 131$ nuclei by $\sim 190\%$. Global effects to the abundance pattern include changes to the abundance of individual nuclear species by as much as $\sim 35\%$. The impact an increase in the neutron capture cross section of ^{130}Sn has on the r-process abundance pattern is shown in Fig. 4.5.

The rate of change in abundance due solely to neutron capture for an individual nucleus, $\dot{Y}(Z, A)$, and the next heavier isotope in Z, $\dot{Y}(Z, A+1)$, is a product of the neutron capture cross section, $\langle v\sigma_{n,\gamma}(Z, A)\rangle$, the abundance of the nucleus, $Y(Z, A)$, and the neutron number density, n_n,

$$\dot{Y}(Z, A+1) = -\dot{Y}(Z, A) = n_n\langle v\sigma_{n,\gamma}(Z, A)\rangle Y(Z, A) \tag{4.5}$$

An increase in the neutron capture cross section will result in a faster depletion of the nucleus (Z, A) by neutron capture. Additionally, a corresponding increase occurs in the production of the next heavier isotope in Z, $(Z, A+1)$. The impact to the abundance of the r-process near ^{130}Sn due to an increase of the ^{130}Sn neutron capture cross section is to hasten both the depletion of ^{130}Sn and the production of ^{131}Sn. This is demonstrated in Fig. 4.6.

Another important consequence that results from the increased production of ^{131}Sn by neutron capture on ^{130}Sn is that the neutrons consumed in the production of ^{131}Sn by neutron capture on ^{130}Sn are no longer available for capture by other

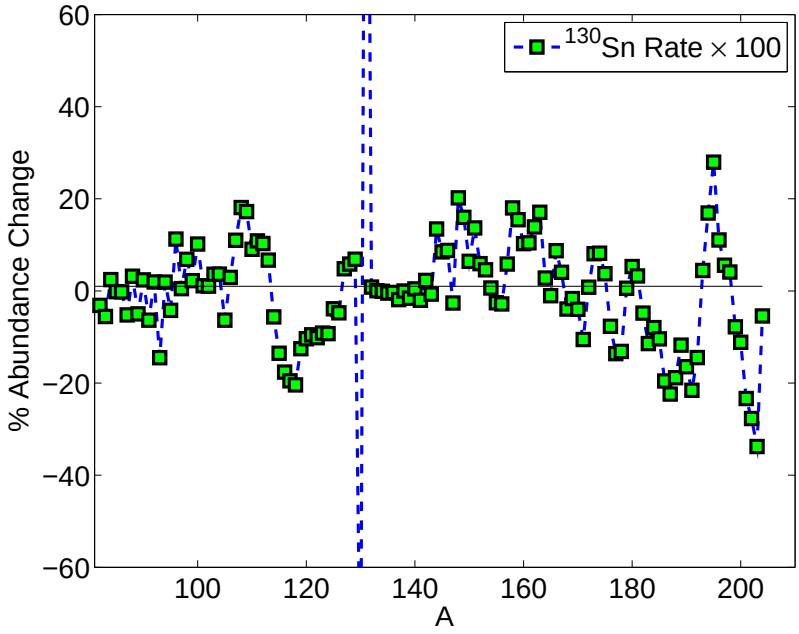


Figure 4.5: The percent change in abundance across the r-process is shown for an r-process calculation under an increase in the neutron capture cross section of ^{130}Sn by a factor of 100 with respect to the baseline calculation. For an r-process with the increased neutron capture cross section, the abundance of the $A = 130$ nuclei decreases by $\sim 90\%$ while the abundance of the $A = 131$ nuclei increases by $\sim 190\%$ with respect to the baseline calculation. The size of the effects on the abundance pattern above the $A = 130$ region range from 0 to $\sim 35\%$.

r-process nuclei. This influence can be quantified by the net rate of neutron capture,

$$\dot{\eta}(Z, A) = n_n \langle v\sigma_{n,\gamma}(Z, A)\rangle Y(Z, A) - \lambda_\gamma(Z, A + 1)Y(Z, A + 1) \tag{4.6}$$

The net rate of neutron capture is the instantaneous rate of neutrons that are captured or released in (n, γ) reactions between the nuclei (Z, A) and $(Z, A + 1)$. The increase in the net rate of neutron capture that occurs in the second peak region is balanced by an equivalent decrease in the net rate of neutron capture in the rare earth and third peak regions. To demonstrate this, we sum the net rate of neutron capture over each of the r-process peak regions, $\sum \dot{\eta}$. Our comparison of $\sum \dot{\eta}$ for each peak region is shown in Fig. 4.7. Our choice of individual r-process peak regions is as follows: the $A = 130$ peak is taken to include nuclei with $A < 145$, the rare earth peak includes nuclei between $145 \leq A < 175$, and the $A = 195$ peak includes nuclei with $A \geq 175$.

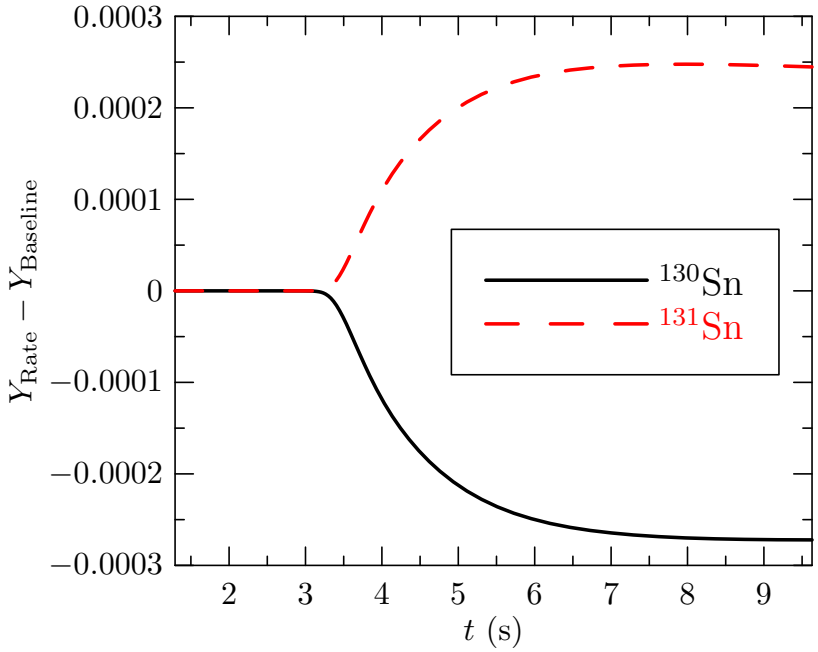


Figure 4.6: The absolute difference in the abundance of ^{130}Sn (solid line) is shown above for an r-process simulation with the neutron capture cross section of ^{130}Sn increased by a factor of 100, Y_{Rate}, and the baseline r-process calculation with the unaltered set of neutron capture rates, Y_{Baseline}. An increase in the neutron capture cross section of ^{130}Sn leads to the capture of additional neutrons by ^{130}Sn, depleting the abundance of ^{130}Sn and enhancing the abundance of ^{131}Sn. The absolute difference in the abundance of ^{131}Sn (dashed line) is also shown.

The specific choice of the range of nuclei used to delineate the peak regions does not influence the result.

An important consequence of the reduced availability of neutrons due to an increase in the neutron capture rate of ^{130}Sn is that the distribution of material within the rare earth and third peak regions is shifted towards lighter nuclei in A compared to the abundance pattern of the baseline r-process calculation. From Eq. 4.5, a decrease in the neutron number density, n_n, locally results in less material from a nucleus (Z, A) advancing to the next nucleus along the isotopic chain, $(Z, A+1)$, by neutron capture. Therefore the effect of the increased neutron capture cross section of ^{130}Sn is not only to increase the neutron capture reaction channel between ^{130}Sn and ^{131}Sn, but also to decrease the overall rate of neutron capture on the rest of

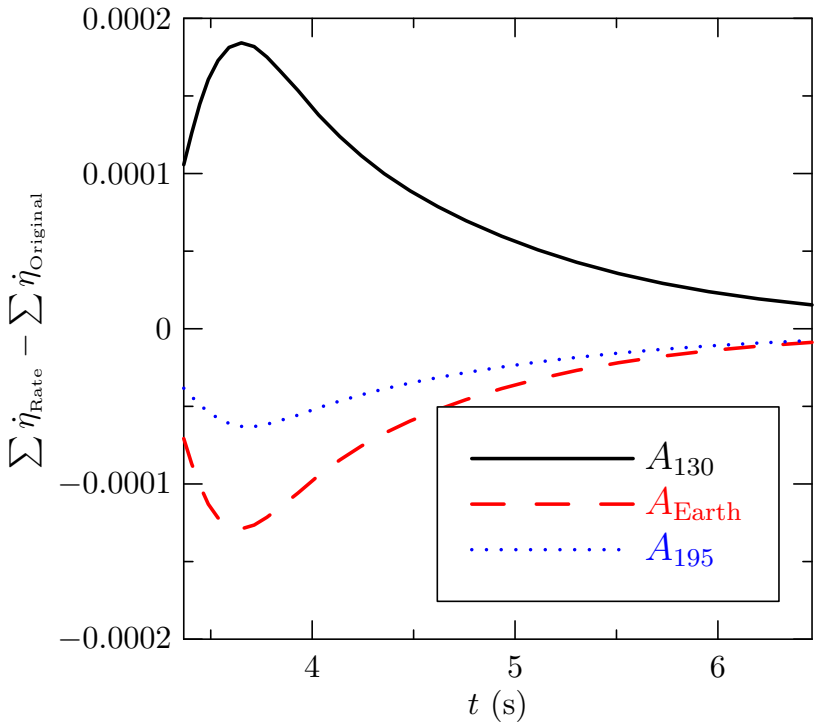


Figure 4.7: We show the relative rate of net neutron capture, $\dot{\eta}$, summed over each of the three peak regions of the r-process (Eq. 4.6). Above, the relative difference in $\sum \dot{\eta}$ is shown between an r-process with the neutron capture cross section of ^{130}Sn increased by a factor of 100, $\sum \dot{\eta}_{\rm Rate}$, and the baseline calculation, $\sum \dot{\eta}_{\rm Original}$. The cross section increase yields an increase in the amount of neutron capture that occurs in the $A \sim 130$ peak and reduces the amount of neutron capture for nuclei in the rare earth and $A \sim 195$ peak regions.

the r-process nuclei. This lowering in the overall rate of neutron capture influences the distribution of material within the rare earth and third peak regions by shifting material within these regions towards lighter nuclei in A. For our r-process calculation under the increased neutron capture cross section, less material reaches the right hand side of the third r-process peak, in nuclei with $A \geq 199$, compared with the abundance pattern of the baseline calculation. This leads to an increase in the abundance of the nuclei on the left hand side of the third r-process peak in the nuclei between $195 \leq A \leq 198$. We find a similar effect occurs in the rare earth region of the r-process, less material populates the heavier, right hand side of the rare earth region, leading to an increase in the abundance of lighter nuclei within the rare earth

region. The impact of the shifting of material in the r-process under an increased neutron capture cross section of ^{130}Sn is shown for the third r-process peak region in Fig. 4.8.

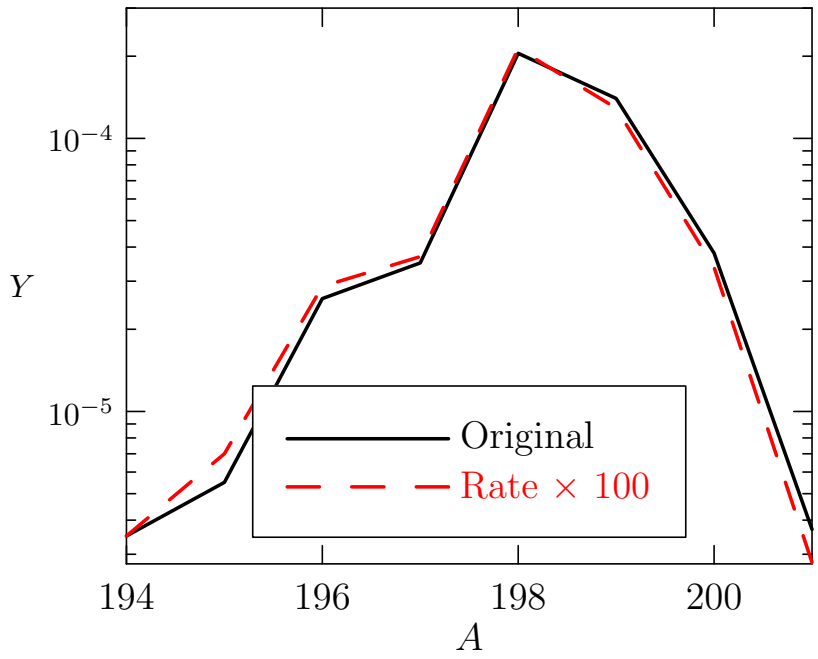


Figure 4.8: The abundance pattern of the third r-process peak is shown above for two r-process calculations, an r-process simulation with the neutron capture cross section of ^{130}Sn increased by a factor of 100 (dashed line), and the baseline r-process calculation with the unaltered set of neutron capture cross sections (solid line). Increasing the neutron capture cross section of ^{130}Sn alters the distribution of material in the rare earth and third peak regions by shifting the abundance towards lighter nuclei in A.

4.5 Conclusions

We have shown, for the case of ^{130}Sn, that an individual neutron capture cross section can be important in shaping the outcome of the r-process. For an increase in the neutron capture cross section of ^{130}Sn by a factor of 100, we find changes to the abundance of nuclei throughout the r-process: changes to the abundance of nuclei near ^{130}Sn are as much as $\sim$ 190%, and changes to the abundance of nuclei

near the third peak region are as much as $\sim 35\%$. We find that a consequence of increasing the neutron capture cross section of ^{130}Sn is to influence where neutrons are captured during the r-process, and this leads to a shifting of material towards lighter nuclei in A in the rare earth and third peak. As our understanding of how the r-process emerges in nature is dependent on models that can accurately reproduce the observed abundance patterns of the r-process, it is important to both identify which nuclei contain these critical neutron capture cross sections that can impact the r-process as well as to conduct the necessary nuclear experiments so that precision neutron capture cross sections for these nuclei may be obtained. Future studies are needed to explore these critical cross sections over a range of astrophysical conditions.

Bibliography

[1] C. Sneden and J. J. Cowan. Genesis of the Heaviest Elements in the Milky Way Galaxy. *Science*, 299:70–75, January 2003.

[2] J. Cowan. private communication, 2007.

[3] F. Käppeler, H. Beer, and K. Wisshak. s-process nucleosynthesis-nuclear physics and the classical model. *Reports of Progress in Physics*, 52:945–1013, August 1989.

[4] D. L. Burris, C. A. Pilachowski, T. E. Armandroff, C. Sneden, J. J. Cowan, and H. Roe. Neutron-Capture Elements in the Early Galaxy: Insights from a Large Sample of Metal-poor Giants. *ApJ*, 544:302–319, November 2000.

[5] M. Sorel, J. M. Conrad, and M. H. Shaevitz. Combined analysis of short-baseline neutrino experiments in the (3+1) and (3+2) sterile neutrino oscillation hypotheses. *Phys. Rev. D*, 70(7):073004, Oct 2004.

[6] Jennifer Simmerer et al. The rise of the s-process in the galaxy. *Astrophys. J.*, 617:1091–1114, 2004.

[7] I. I. Ivans, J. Simmerer, C. Sneden, J. E. Lawler, J. J. Cowan, R. Gallino, and S. Bisterzo. Near-Ultraviolet Observations of HD 221170: New Insights into the Nature of r-Process-rich Stars. *ApJ*, 645:613–633, July 2006.

[8] E. M. Burbidge, G. R. Burbidge, W. A. Fowler, and F. Hoyle. Synthesis of the Elements in Stars. *Reviews of Modern Physics*, 29:547–650, 1957.

[9] A. G. W. Cameron. *Chalk River Rep.*, CRL-41, 1957.

[10] J. J. Cowan, F.-K. Thielemann, and J. W. Truran. The R-process and nucleochronology. *Phys. Rep.*, 208:267–394, November 1991.

[11] Y.-Z. Qian. The origin of the heavy elements: Recent progress in the understanding of the r-process [review article]. *Progress in Particle and Nuclear Physics*, 50:153–199, 2003.

[12] B. S. Meyer. The r-, s-, and p-Processes in Nucleosynthesis. *ARA&A*, 32:153–190, 1994.

[13] S. Goriely and M. Arnould. Waiting point approximation and canonical multi-event r-process revisited. *A&A*, 312:327–337, August 1996.

[14] K.-L. Kratz, F.-K. Thielemann, W. Willebrandt, P. Moller, V. Harms, A. Wohr, and J. W. Truran. Constraints on r-process conditions from beta-decay properties far off stability and r-abundances. *Journal of Physics G Nuclear Physics*, 14:331–+, December 1988.

[15] S. Goriely and M. Arnould. The r-process in the light of a microscopic model for nuclear masses. *A&A*, 262:73–82, August 1992.

[16] K.-L. Kratz, J.-P. Bitouzet, F.-K. Thielemann, P. Moeller, and B. Pfeiffer. Isotopic r-process abundances and nuclear structure far from stability - Implications for the r-process mechanism. *ApJ*, 403:216–238, January 1993.

[17] P. A. Seeger, W. A. Fowler, and D. D. Clayton. Nucleosynthesis of Heavy Elements by Neutron Capture. *ApJS*, 11:121–+, February 1965.

[18] S. E. Woosley and R. D. Hoffman. The alpha-process and the r-process. *ApJ*, 395:202–239, August 1992.

[19] B. S. Meyer, G. J. Mathews, W. M. Howard, S. E. Woosley, and R. D. Hoffman. R-process nucleosynthesis in the high-entropy supernova bubble. *ApJ*, 399:656–664, November 1992.

[20] S. E. Woosley, J. R. Wilson, G. J. Mathews, R. D. Hoffman, and B. S. Meyer. The r-process and neutrino-heated supernova ejecta. *ApJ*, 433:229–246, September 1994.

[21] K. Takahashi, J. Witti, and H.-T. Janka. Nucleosynthesis in neutrino-driven winds from protoneutron stars II. The r-process. *A&A*, 286:857–869, June 1994.

[22] Y.-Z. Qian and S. E. Woosley. Nucleosynthesis in Neutrino-driven Winds. I. The Physical Conditions. *ApJ*, 471:331–+, November 1996.

[23] C. Y. Cardall and G. M. Fuller. General Relativistic Effects in the Neutrino-driven Wind and r-Process Nucleosynthesis. *ApJ*, 486:L111+, September 1997.

[24] K. Otsuki, H. Tagoshi, T. Kajino, and S.-y. Wanajo. General Relativistic Effects on Neutrino-driven Winds from Young, Hot Neutron Stars and r-Process Nucleosynthesis. *ApJ*, 533:424–439, April 2000.

[25] K. Sumiyoshi, H. Suzuki, K. Otsuki, M. Terasawa, and S. Yamada. Hydrodynamical Study of Neutrino-Driven Wind as an r-Process Site. *PASJ*, 52:601–611, August 2000.

[26] S. Wanajo, T. Kajino, G. J. Mathews, and K. Otsuki. The r-Process in Neutrino-driven Winds from Nascent, "Compact" Neutron Stars of Core-Collapse Supernovae. *ApJ*, 554:578–586, June 2001.

[27] T. A. Thompson, A. Burrows, and B. S. Meyer. The Physics of Proto-Neutron Star Winds: Implications for r-Process Nucleosynthesis. *ApJ*, 562:887–908, December 2001.

[28] K. Sumiyoshi, M. Terasawa, G. J. Mathews, T. Kajino, S. Yamada, and H. Suzuki. r-Process in Prompt Supernova Explosions Revisited. *ApJ*, 562:880–886, December 2001.

[29] S. Wanajo, M. Tamamura, N. Itoh, K. Nomoto, Y. Ishimaru, T. C. Beers, and S. Nozawa. The r-Process in Supernova Explosions from the Collapse of O-Ne-Mg Cores. *ApJ*, 593:968–979, August 2003.

[30] R. Surman and G. C. McLaughlin. Neutrinos and Nucleosynthesis in Gamma-Ray Burst Accretion Disks. *ApJ*, 603:611–623, March 2004.

[31] Rebecca Surman, G. C. McLaughlin, and W. R. Hix. Nucleosynthesis in the outflow from gamma ray burst accretion disks. *Astrophys. J.*, 643:1057–1064, 2006.

[32] G. C. McLaughlin and R. Surman. Prospects for obtaining an r process from Gamma Ray Burst Disk Winds. *Nuclear Physics A*, 758:189–196, July 2005.

[33] C. Freiburghaus, S. Rosswog, and F.-K. Thielemann. R-Process in Neutron Star Mergers. *ApJ*, 525:L121–L124, November 1999.

[34] S. Goriely, P. Demetriou, H.-T. Janka, J. M. Pearson, and M. Samyn. The r-process nucleosynthesis: a continued challenge for nuclear physics and astrophysics. *Nuclear Physics A*, 758:587–594, July 2005.

[35] A. I. MacFadyen and S. E. Woosley. Collapsars: Gamma-Ray Bursts and Explosions in "Failed Supernovae". *ApJ*, 524:262–289, October 1999.

[36] J. Pruet, T. A. Thompson, and R. D. Hoffman. Nucleosynthesis in Outflows from the Inner Regions of Collapsars. *ApJ*, 606:1006–1018, May 2004.

[37] H. Ning, Y. Z. Qian, and B. S. Meyer. r-process nucleosynthesis in shocked surface layers of o- ne-mg cores. 2007.

[38] H. Th. Janka, B. Mueller, F. S. Kitaura, and R. Buras. Dynamics of shock propagation and nucleosynthesis conditions in o-ne-mg core supernovae. 2007.

[39] S. E. Woosley, A. Heger, and T. A. Weaver. The evolution and explosion of massive stars. *Reviews of Modern Physics*, 74:1015–1071, November 2002.

[40] H. A. Bethe. Supernova mechanisms. *Reviews of Modern Physics*, 62:801–866, 1990.

[41] R. Mayle, J. R. Wilson, and D. N. Schramm. Neutrinos from gravitational collapse. *ApJ*, 318:288–306, July 1987.

[42] Yong-Zhong Qian, George M. Fuller, Grant J. Mathews, Ron W. Mayle, James R. Wilson, and S. E. Woosley. Connection between flavor-mixing of cosmologically significant neutrinos and heavy element nucleosynthesis in supernovae. *Phys. Rev. Lett.*, 71(13):1965–1968, Sep 1993.

[43] G. C. McLaughlin, J. M. Fetter, A. B. Balantekin, and G. M. Fuller. Active-sterile neutrino transformation solution for r-process nucleosynthesis. *Phys. Rev. C*, 59:2873–2887, May 1999.

[44] W. R. Hix and F. K. Thielemann. Computational methods for nucleosynthesis and nuclear energy generation. *J. Comp. App. Math.*, 109:321–+, 1999.

[45] R. Surman and J. Engel. Changes in r-process abundances at late times. *Phys. Rev. C*, 64(3):035801–+, September 2001.

[46] T. Rauscher and F.-K. Thielemann. Astrophysical Reaction Rates From Statistical Model Calculations. *Atomic Data and Nuclear Data Tables*, 75:1–2, May 2000.

[47] William H. Press, Saul A. Teukolsky, William T. Vetterling, and Brian P. Flannery. *Numerical Recipes in FORTRAN: The Art of Scientific Computing*. Cambridge University Press, New York, NY, USA, 1992.

[48] P. Möller, J. R. Nix, and K.-L. Kratz. Nuclear Properties for Astrophysical and Radioactive-Ion Beam Applications. *Atomic Data and Nuclear Data Tables*, 66:131–+, 1997.

[49] P. Möller and J. Randrup. New developments in the calculation of β-strength functions. *Nuclear Physics A*, 514:1–48, July 1990.

[50] G. M. Fuller and B. S. Meyer. Neutrino Capture and Supernova Nucleosynthesis. *ApJ*, 453:792–+, November 1995.

[51] C. Sneden, A. McWilliam, G. W. Preston, J. J. Cowan, D. L. Burris, and B. J. Armosky. The Ultra–Metal-poor, Neutron-Capture–rich Giant Star CS 22892-052. *ApJ*, 467:819–+, August 1996.

[52] J. M. Pearson and S. Goriely. Nuclear mass formulas for astrophysics. *Nuclear Physics A*, 777:623–644, October 2006.

[53] Y.-Z. Qian, P. Vogel, and G. J. Wasserburg. Diverse Supernova Sources for the r-Process. *ApJ*, 494:285–+, February 1998.

[54] D. Argast, M. Samland, F.-K. Thielemann, and Y.-Z. Qian. Neutron star mergers versus core-collapse supernovae as dominant r-process sites in the early Galaxy. *A&A*, 416:997–1011, March 2004.

[55] J. J. Cowan, F.-K. Thielemann, and J. W. Truran. Nuclear chronometers from the r-process and the age of the galaxy. *ApJ*, 323:543–552, December 1987.

[56] I. V. Panov and F.-K. Thielemann. Fission and the r-Process: The Rates of Induced and Delayed Fission. *Astronomy Letters*, 29:510–521, August 2003.

[57] B. S. Meyer. Neutrino Reactions on 4He and the r-Process. *ApJ*, 449:L55+, August 1995.

[58] R. D. Hoffman, S. E. Woosley, and Y.-Z. Qian. Nucleosynthesis in Neutrino-driven Winds. II. Implications for Heavy Element Synthesis. *ApJ*, 482:951–+, June 1997.

[59] G. C. McLaughlin, G. M. Fuller, and J. R. Wilson. The Influence of Nuclear Composition on the Electron Fraction in the Post–Core Bounce Supernova Environment. *ApJ*, 472:440–+, December 1996.

[60] B. S. Meyer, G. C. McLaughlin, and G. M. Fuller. Neutrino capture and r-process nucleosynthesis. *Phys. Rev. C*, 58:3696–3710, December 1998.

[61] Bradley S. Meyer. *r*-process nucleosynthesis without excess neutrons. *Phys. Rev. Lett.*, 89(23):231101, Nov 2002.

[62] B. S. Meyer. Decompression of initially cold neutron star matter - A mechanism for the r-process? *ApJ*, 343:254–276, August 1989.

[63] S. Rosswog, M. Liebendörfer, F.-K. Thielemann, M. B. Davies, W. Benz, and T. Piran. Mass ejection in neutron star mergers. *A&A*, 341:499–526, January 1999.

[64] M. Apollonio and A. Baldini. Limits on neutrino oscillations from the CHOOZ experiment. *Physics Letters B*, 466:415–430, November 1999.

[65] B. Armbruster, I. M. Blair, B. A. Bodmann, N. E. Booth, G. Drexlin, J. A. Edgington, C. Eichner, K. Eitel, E. Finckh, H. Gemmeke, J. Hößl, T. Jannakos, P. Jünger, M. Kleifges, J. Kleinfeller, W. Kretschmer, R. Maschuw, C. Oehler, P. Plischke, J. Reichenbacher, C. Ruf, M. Steidl, J. Wolf, and B. Zeitnitz. Upper limits for neutrino oscillations from muon decay at rest. *Phys. Rev. D*, 65(11):112001, Jun 2002.

[66] C. Athanassopoulos, L. B. Auerbach, R. L. Burman, D. O. Caldwell, E. D. Church, I. Cohen, J. B. Donahue, A. Fazely, F. J. Federspiel, G. T. Garvey, R. M. Gunasingha, R. Imlay, K. Johnston, H. J. Kim, W. C. Louis, R. Majkic, K. McIlhany, G. B. Mills, R. A. Reeder, V. Sandberg, D. Smith, I. Stancu, W. Strossman, R. Tayloe, G. J. VanDalen, W. Vernon, and N. Wadia. Results on $\nu_\mu \rightarrow \nu_e$ neutrino oscillations from the lsnd experiment. *Phys. Rev. Lett.*, 81(9):1774–1777, Aug 1998.

[67] R. H. Cyburt, B. D. Fields, K. A. Olive, and E. Skillman. New BBN limits on physics beyond the standard model from ˆ4He. *Astroparticle Physics*, 23:313–323, April 2005.

[68] V. Barger, J. P. Kneller, P. Langacker, D. Marfatia, and G. Steigman. Hiding relativistic degrees of freedom in the early universe. *Physics Letters B*, 569:123–128, September 2003.

[69] V. Barger, J. P. Kneller, H.-S. Lee, D. Marfatia, and G. Steigman. Effective number of neutrinos and baryon asymmetry from BBN and WMAP. *Physics Letters B*, 566:8–18, July 2003.

[70] Kevork Abazajian, Nicole F. Bell, George M. Fuller, and Yvonne Y. Y. Wong. Cosmological lepton asymmetry, primordial nucleosynthesis and sterile neutrinos. *Physical Review D (Particles, Fields, Gravitation, and Cosmology)*, 72(6):063004, 2005.

[71] David O. Caldwell, George M. Fuller, and Yong-Zhong Qian. Sterile neutrinos and supernova nucleosynthesis. *Phys. Rev. D*, 61(12):123005, May 2000.

[72] H. Nunokawa, J. T. Peltoniemi, A. Rossi, and J. W. F. Valle. Supernova bounds on resonant active-sterile neutrino conversions. *Phys. Rev. D*, 56(3):1704–1713, Aug 1997.

[73] S. Eidelman, K.G. Hayes, K.A. Olive, M. Aguilar-Benitez, C. Amsler, D. Asner, K.S. Babu, R.M. Barnett, J. Beringer, P.R. Burchat, C.D. Carone, C. Caso, G. Conforto, O. Dahl, G. D'Ambrosio, M. Doser, J.L. Feng, T. Gherghetta, L. Gibbons, M. Goodman, C. Grab, D.E. Groom, A. Gurtu, K. Hagiwara, J.J. Hernández-Rey, K. Hikasa, K. Honscheid, H. Jawahery, C. Kolda, Kwon Y., M.L. Mangano, A.V. Manohar, J. March-Russell, A. Masoni, R. Miquel, K. Mönig, H. Murayama, K. Nakamura, S. Navas, L. Pape, C. Patrignani, A. Piepke, G. Raffelt, M. Roos, M. Tanabashi, J. Terning, N.A. Törnqvist, T.G. Trippe, P. Vogel, C.G. Wohl, R.L. Workman, W.-M. Yao, P.A. Zyla, B. Armstrong, P.S. Gee, G. Harper, K.S. Lugovsky, S.B. Lugovsky, V.S. Lugovsky, A. Rom, M. Artuso, E. Barberio, M. Battaglia, H. Bichsel, O. Biebel, P. Bloch, R.N. Cahn, D. Casper, A. Cattai, R.S. Chivukula, G. Cowan, T. Damour, K. Desler, M.A. Dobbs, M. Drees, A. Edwards, D.A. Edwards, V.D. Elvira, J. Erler, V.V. Ezhela, W. Fetscher, B.D. Fields, B. Foster, D. Froidevaux, M. Fukugita, T.K. Gaisser, L. Garren, H.-J. Gerber, G. Gerbier, F.J. Gilman, H.E. Haber, C. Hagmann, J. Hewett, I. Hinchliffe, C.J. Hogan, G. Höhler, P. Igo-Kemenes, J.D. Jackson, K.F. Johnson, D. Karlen, B. Kayser, D. Kirkby, S.R. Klein, K. Kleinknecht, I.G. Knowles, P. Kreitz, Yu.V. Kuyanov, O. Lahav, P. Langacker, A. Liddle, L. Littenberg, D.M. Manley, A.D. Martin, M. Narain, P. Nason, Y. Nir, J.A. Peacock, H.R. Quinn, S. Raby, B.N. Ratcliff, E.A.

Razuvaev, B. Renk, G. Rolandi, M.T. Ronan, L.J. Rosenberg, C.T. Sachrajda, Y. Sakai, A.I. Sanda, S. Sarkar, M. Schmitt, O. Schneider, D. Scott, W.G. Seligman, M.H. Shaevitz, T. Sjöstrand, G.F. Smoot, S. Spanier, H. Spieler, N.J.C. Spooner, M. Srednicki, A. Stahl, T. Stanev, M. Suzuki, N.P. Tkachenko, G.H. Trilling, G. Valencia, K. van Bibber, M.G. Vincter, D. Ward, B.R. Webber, M. Whalley, L. Wolfenstein, J. Womersley, C.L. Woody, O.V. Zenin, and R.-Y. Zhu. Review of Particle Physics. *Physics Letters B*, 592:1+, 2004.

[74] L. Wolfenstein. Neutrino oscillations in matter. *Phys. Rev. D*, 17(9):2369–2374, May 1978.

[75] J. Fetter, G. C. McLaughlin, A. B. Balantekin, and G. M. Fuller. Active-sterile neutrino conversion: consequences for the r-process and supernova neutrino detection. *Astroparticle Physics*, 18:433–448, February 2003.

[76] P. Möller, J. R. Nix, W. D. Myers, and W. J. Swiatecki. Nuclear Ground-State Masses and Deformations. *Atomic Data and Nuclear Data Tables*, 59:185–+, 1995.

[77] J. J. Cowan, B. Pfeiffer, K.-L. Kratz, F.-K. Thielemann, C. Sneden, S. Burles, D. Tytler, and T. C. Beers. R-Process Abundances and Chronometers in Metal-poor Stars. *ApJ*, 521:194–205, August 1999.

[78] T. Rauscher, J. H. Applegate, J. J. Cowan, F.-K. Thielemann, and M. Wiescher. Production of heavy elements in inhomogeneous cosmologies. *ApJ*, 429:499–530, July 1994.

[79] C. Sneden, J. J. Cowan, J. E. Lawler, I. I. Ivans, S. Burles, T. C. Beers, F. Primas, V. Hill, J. W. Truran, G. M. Fuller, B. Pfeiffer, and K.-L. Kratz. The Extremely Metal-poor, Neutron Capture-rich Star CS 22892-052: A Comprehensive Abundance Analysis. *ApJ*, 591:936–953, July 2003.

[80] B. S. Meyer and J. S. Brown. Survey of r-Process Models. *ApJS*, 112:199–+, September 1997.

[81] G. Audi, O. Bersillon, J. Blachot, and A. H. Wapstra. The Nubase evaluation of nuclear and decay properties. *Nuclear Physics A*, 729:3–128, December 2003.

[82] D. N. Spergel, R. Bean, O. Doré, M. R. Nolta, C. L. Bennett, J. Dunkley, G. Hinshaw, N. Jarosik, E. Komatsu, L. Page, H. V. Peiris, L. Verde, M. Halpern, R. S. Hill, A. Kogut, M. Limon, S. S. Meyer, N. Odegard, G. S. Tucker, J. L. Weiland, E. Wollack, and E. L. Wright. Three-Year Wilkinson Microwave Anisotropy Probe (WMAP) Observations: Implications for Cosmology. *ApJS*, 170:377–408, June 2007.

[83] L. M. Krauss and B. Chaboyer. New Globular Cluster Age Estimates and Constraints on the Cosmic Equation of State and The Matter Density of the Universe. *ArXiv Astrophysics e-prints*, November 2001.

[84] A. McWilliam, G. W. Preston, C. Sneden, and L. Searle. Spectroscopic Analysis of 33 of the Most Metal Poor Stars. II. *AJ*, 109:2757–+, June 1995.

[85] A. McWilliam. Barium Abundances in Extremely Metal-poor Stars. *AJ*, 115:1640–1647, April 1998.

[86] J. Westin, C. Sneden, B. Gustafsson, and J. J. Cowan. The r-Process-enriched Low-Metallicity Giant HD 115444. *ApJ*, 530:783–799, February 2000.

[87] R. Cayrel, V. Hill, T. C. Beers, B. Barbuy, M. Spite, F. Spite, B. Plez, J. Andersen, P. Bonifacio, P. François, P. Molaro, B. Nordström, and F. Primas. Measurement of stellar age from uranium decay. *Nature*, 409:691–692, February 2001.

[88] V. Hill, B. Plez, R. Cayrel, T. C. Beers, B. Nordström, J. Andersen, M. Spite, F. Spite, B. Barbuy, P. Bonifacio, E. Depagne, P. François, and F. Primas. First stars. I. The extreme r-element rich, iron-poor halo giant CS 31082-001. Implications for the r-process site(s) and radioactive cosmochronology. *A&A*, 387:560–579, May 2002.

[89] J. J. Cowan, C. Sneden, S. Burles, I. I. Ivans, T. C. Beers, J. W. Truran, J. E. Lawler, F. Primas, G. M. Fuller, B. Pfeiffer, and K.-L. Kratz. The Chemical Composition and Age of the Metal-poor Halo Star BD 3248. *ApJ*, 572:861–879, June 2002.

[90] S. Honda, W. Aoki, T. Kajino, H. Ando, T. C. Beers, H. Izumiura, K. Sadakane, and M. Takada-Hidai. Spectroscopic Studies of Extremely Metal-Poor Stars with the Subaru High Dispersion Spectrograph. II. The r-Process Elements, Including Thorium. *ApJ*, 607:474–498, May 2004.

[91] N. Christlieb, T. C. Beers, P. S. Barklem, M. Bessell, V. Hill, J. Holmberg, A. J. Korn, B. Marsteller, L. Mashonkina, Y.-Z. Qian, S. Rossi, G. J. Wasserburg, F.-J. Zickgraf, K.-L. Kratz, B. Nordström, B. Pfeiffer, J. Rhee, and S. G. Ryan. The Hamburg/ESO R-process Enhanced Star survey (HERES). I. Project description, and discovery of two stars with strong enhancements of neutron-capture elements. *A&A*, 428:1027–1037, December 2004.

[92] A. Frebel, N. Christlieb, J. E. Norris, C. Thom, T. C. Beers, and J. Rhee. Discovery of HE 1523-0901, a Strongly r-Process-enhanced Metal-poor Star with Detected Uranium. *ApJ*, 660:L117–L120, May 2007.

[93] F. Montes, T. C. Beers, J. Cowan, T. Elliot, K. Farouqi, R. Gallino, M. Heil, K.-L. Kratz, B. Pfeiffer, M. Pignatari, and H. Schatz. Nucleosynthesis in the Early Galaxy. *ApJ*, 671:1685–1695, December 2007.

[94] John J. Cowan, C. Sneden, J. E. Lawler, and E. A. Den Hartog. r-process enhanced halo stars. *PoS*, NIC-IX:014, 2006.

[95] M. Arnould, S. Goriely, and K. Takahashi. The r-process of stellar nucleosynthesis: Astrophysics and nuclear physics achievements and mysteries. *ArXiv e-prints*, 705, May 2007.

[96] Joshua Beun, G. C. McLaughlin, R. Surman, and W. R. Hix. Neutrinos, fisson cycling, and the r-process. *PoS*, NIC-IX:140, 2006.

[97] Gabriel Martinez-Pinedo et al. Nucleosynthesis in neutrino heated matter: The nu-p-process and the r-process. *PoS*, NIC-IX:064, 2006.

[98] F. K. Thielemann et al. Element synthesis in stars. *Prog. Part. Nucl. Phys.*, 46:5–22, 2001.

[99] S. Rosswog, E. Ramirez-Ruiz, and M. B. Davies. High-resolution calculations of merging neutron stars - III. Gamma-ray bursts. *MNRAS*, 345:1077–1090, November 2003.

[100] S. W. Bruenn. The prompt-shock supernova mechanism. I - The effect of the free-proton mass fraction and the neutrino transport algorithm. *ApJ*, 340:955–965, May 1989.

[101] S. W. Bruenn. The prompt-shock supernova mechanism. II - Supranuclear EOS behavior and the precollapse model. *ApJ*, 341:385–400, June 1989.

[102] A. Arcones, Hans-Thomas Janka, and L. Scheck. Nucleosynthesis-relevant conditions in neutrino-driven supernova outflows. i. spherically symmetric hydrodynamic simulations. 2006.

[103] S. Wanajo. Cold r-Process in Neutrino-Driven Winds. *ArXiv e-prints*, 706, June 2007.

[104] A. Burrows, L. Dessart, E. Livne, C. D. Ott, and J. Murphy. Simulations of Magnetically-Driven Supernova and Hypernova Explosions in the Context of Rapid Rotation. *ArXiv Astrophysics e-prints*, February 2007.

[105] B. D. Metzger, T. A. Thompson, and E. Quataert. Proto-Neutron Star Winds with Magnetic Fields and Rotation. *ApJ*, 659:561–579, April 2007.

[106] J. Beun, G. C. McLaughlin, R. Surman, and W. R. Hix. Fission cycling in supernova nucleosynthesis: Active-sterile neutrino oscillations. *Phys. Rev. D*, 73(9):093007–+, May 2006.

[107] I. V. Panov, E. Kolbe, B. Pfeiffer, T. Rauscher, K.-L. Kratz, and F.-K. Thielemann. Calculations of fission rates for r-process nucleosynthesis. *Nuclear Physics A*, 747:633–654, January 2005.

[108] R. C. Duncan, S. L. Shapiro, and I. Wasserman. Neutrino-driven winds from young, hot neutron stars. *ApJ*, 309:141–160, October 1986.

[109] C. L. Fryer, F. Herwig, A. Hungerford, and F. X. Timmes. Supernova Fallback: A Possible Site for the r-Process. *ApJ*, 646:L131–L134, August 2006.

[110] G. C. McLaughlin and G. M. Fuller. Neutrino Capture on Heavy Nuclei. *ApJ*, 455:202–+, December 1995.

[111] Rebecca Surman, Jonathan Engel, Jonathan R. Bennett, and Bradley S. Meyer. Source of the rare-earth element peak in r-process nucleosynthesis. *Phys. Rev. Lett.*, 79(10):1809–1812, Sep 1997.

[112] C. Freiburghaus, J.-F. Rembges, T. Rauscher, E. Kolbe, F.-K. Thielemann, K.-L. Kratz, B. Pfeiffer, and J. J. Cowan. The Astrophysical r-Process: A Comparison of Calculations following Adiabatic Expansion with Classical Calculations Based on Neutron Densities and Temperatures. *ApJ*, 516:381–398, May 1999.

[113] E. R. Hilf et al. *Suppl. to Proc. Int. Conf. NFFS-3*, 76-13:142, 1976.

[114] I. V. Panov and F.-K. Thielemann. Fission and the r-Process: Competition between Neutron-Induced and Beta-Delayed Fission. *Astronomy Letters*, 30:647–655, September 2004.

[115] E. Kolbe, K. Langanke, and G. M. Fuller. Neutrino-Induced Fission of Neutron-Rich Nuclei. *Physical Review Letters*, 92(11):111101–+, March 2004.

[116] M. Terasawa, K. Langanke, T. Kajino, G. J. Mathews, and E. Kolbe. Neutrino Effects before, during, and after the Freezeout of the r-Process. *ApJ*, 608:470–479, June 2004.

[117] A. Kelić, N. Zinner, E. Kolbe, K. Langanke, and K.-H. Schmidt. Cross sections and fragment distributions from neutrino-induced fission on r-process nuclei. *Physics Letters B*, 616:48–58, June 2005.

[118] J. M. Pearson, R. C. Nayak, and S. Goriely. Nuclear mass formula with Bogolyubov-enhanced shell-quenching: application to r-process. *Physics Letters B*, 387:455–459, February 1996.

[119] J. Duflo and A.P. Zuker. Microscopic mass formulas. *Phys. Rev. C*, 52(1):R23–R27, Jul 1995.

[120] Y.-Z. Qian. Neutrino-induced Fission and r-Process Nucleosynthesis. *ApJ*, 569:L103–L106, April 2002.

[121] S. Goriely and M. Arnould. Actinides: How well do we know their stellar production? *A&A*, 379:1113–1122, December 2001.

[122] K. Otsuki, G. J. Mathews, and T. Kajino. r-Process abundance universality and actinide cosmochronology. *New Astronomy*, 8:767–776, November 2003.

[123] Y. Aboussir, J. M. Pearson, A. K. Dutta, and F. Tondeur. Nuclear Mass Formula via an Approximation to the Hartree-Fock Method. *Atomic Data and Nuclear Data Tables*, 61:127–+, 1995.

[124] R. Surman and J. Engel. Changes in r-process abundances at late times. *Phys. Rev. C*, 64(3):035801, Aug 2001.

[125] R. L. Kozub, J. F. Shriner, Jr., A. Adekola, D. W. Bardayan, J. C. Blackmon, F. Liang, C. D. Nesaraja, D. Shapira, M. S. Smith, K. Y. Chae, K. L. Jones, Z. Ma, B. H. Moazen, K. Chipps, L. Erikson, J. A. Cizewski, R. Hatarik, S. D. Pain, C. Matei, W. Krolas, and T. P. Swan. Single particle states in ˆ131Sn and the r-process. *APS Meeting Abstracts*, pages H10+, October 2007.

[126] P. Möller, B. Pfeiffer, and K.-L. Kratz. New calculations of gross β-decay properties for astrophysical applications: Speeding-up the classical r process. *Phys. Rev. C*, 67(5):055802–+, May 2003.